UNIVERSITY OF CINCINNATI

Date: August 8, 2006

I, Amensisa Abdi,

hereby submit this work as part of the requirements for the degree of:

Doctor of Philosophy

in:

Physics

It is entitled:

Probing Electronic and Vibronic States in CdTe Self-Assembled Quantum Dots and CdS Nanowires using Room Temperature Resonant Raman Scattering

This work and its defense approved by:

Chair: Howard E Jackson

Leigh M Smith

Jan Yarrison-Rice

Michael Ma

Philip Argyres

Probing Electronic and Vibronic States in CdTe Self-Assembled Quantum Dots and CdS Nanowires using Room Temperature Resonant Raman Scattering

A dissertation submitted to the

Division of Research and Advanced Studies
of the University of Cincinnati

in partial fulfillment of the
requirements for the degree of

DOCTOR OF PHILOSOPHY (Ph.D.)

in the Department of Physics
of the College of Arts and Sciences

2006

by

Amensisa Abdi Berato

B.S., Asmara University, Asmara, Ethiopia, 1990
M.S., Addis Ababa University, Addis Ababa, Ethiopia, 1995
M.S., University of Cincinnati, 2002

Committee Chair: Professor Howard E. Jackson, Ph.D.

Abstract

Resonant Raman scattering (RRS) is a sensitive means to probe electronic and vibrational states in semiconductor nanostructures, even when such states are not accessible either through photoluminescence or transport techniques. In this thesis, resonant Raman scattering is used to probe the electronic and vibronic states of CdTe/ZnTe quantum dots and CdS nanowires at room temperature. In case of the CdTe/ZnTe quantum dots, the sensitivity of the ZnTe longitudinal optical phonon (LO) resonance is used to probe the excited state in the CdTe quantum dots. In addition, this technique is utilized to study the energy shifts due to post growth rapid thermal annealing. Due to annealing, both the ground and excited state energies of the quantum dots move to a higher value. This is consistent with the interdiffusion of Zn and Cd which makes the confining potential shallower and the average diameter of the quantum dots larger.

In the case of the CdS nanowires, the 1-LO and 2-LO resonance is readily observed above the broad photoluminescence (PL) background. The lineshape of the integrated intensity of the 1-LO and 2-LO resembles the PL spectrum suggesting that the RRS probes the electronic states in both the ensemble and in single nanowires. In addition, the energy separation between the peaks of the 1-LO and 2-LO resonance of the ensemble CdS nanowires was found to be 34 meV which is comparable to the 37 meV value measured in bulk samples.

We also show that spatially-resolved Raman scattering at resonance probes the

structural uniformity in a single CdS nanowire and is able to identify the layers of the CdTe/ZnTe quantum dots sample. We found RRS intensity of single CdS nanowire strongly depends on the morphology of the wire.

In conclusion, we have shown that RRS at room temperature is a sensitive and nondestructive tool to probe electronic and vibration sates as well as structural uniformity in semiconductor nanostructures.

Acknowledgments

First of all, I would like to express my deepest gratitude to my advisor, Prof. Howard Jackson, for his guidance, constant support, encouragement and patience throughout my graduate studies at the University of Cincinnati. I would not have been able to complete my PhD without his efforts and supports.

I would also like to extend my sincere gratitude to my co-advisers, Profs. Jan Yarsison-Rice and Leigh Smith, for giving me solid training on how to carry out scientific research, regular support, encouragement and keeping me on track whenever I ran into problems.

I am thankful to Profs. Michael Ma and Philip Argyres for agreeing to serve on my dissertation committee in short notice.

I am grateful to Dr. Lyubov Titova and Dr. Sebastian Mackowski. Dr. Lyuba's valuable discussions and help during writing papers and running experiments are unforgettable. Particularly, the speed at which she used to arrive in lab whenever I gave her a call was amazing. She is a very wonderful person both socially and professionally.

I would like to thank my lab colleagues Aditi Sharma, Tak Gurung, Kapila Hewaparakrama, and Thang Baong. I had valuable discussions and enjoyed working with them in lab.

I am indebted to John Markus for his help and advice during constructing lab equipment. I am also indebted to the machine shop staff, Bob Schrott, Mark Ankenbauer and Mark Satatelli for constructing my specialized equipment. I am also indebted to David Will and John Whitaker for their assistance with computer issues.

My appreciation goes to Melody Whitlock, Donna Deutenberg, and Elle Mengon for being so supportive throughout my graduate studies. I would also like to extend my appreciation to all the physics department staff for teaching me and helping me in numerous ways.

And last but not least, I would like to express my deepest appreciation to my wife and three boys for understanding me and being supportive during my entire graduate studies.

Table of Contents

List of Figures

Introduction

In recent years increasing interest has been focused on low dimensional semiconductor nanostructures, particularly quantum dots and nanowires, due to both their importance in fundamental physics and their potential for device applications. Quantum dots and nanowires provide strong confining potentials for both electrons and holes, and thus exhibit pronounced quantum effects for length scales smaller than the de-Broglie wavelength. The confinement of electrons and holes in these nanostructures modifies the electronic as well as the optical and vibrational properties of the material. To characterize and understand these nanostructures, we utilize room temperature resonant Raman scattering coupled with photoluminescence measurements. In this thesis, we have studied group II-IV semiconductor nanostructure samples, namely as-grown and annealed CdTe/ZnTe self-assembled quantum dots (SAQDs), and an ensemble as well as single CdS nanowires.

The CdTe/ZnTe SAQDs samples studied in this thesis were grown by molecular beam epitaxy (MBE). Using MBE, one can grow high-quality layers with good control of thickness and composition. The formation of SAQDs is a strain-driven process that occurs due to the lattice mismatch between CdTe and ZnTe semiconductor layers.[1] In the SAQDs, electrons and holes are strongly spatially confined and quantum effects become dominant. It was predicted in 1980s that SAQDs would exhibit a lower threshold current and higher light emission efficiency that are essential for the fabrication of better semiconductor lasers.[2,3] Ledentsov and colleagues demonstrated a quantum dots laser in 1994 for the first time.[4] Recently, in September 2004, the first

high-speed, 10Gbps, quantum dot laser that was stable over a temperature range of 20°C to 70°C was reported by Arakawa and Sakaki.[5] This breakthrough laser technology, based on the self-assembly growth of III-V quantum dots, operates at a wavelength of 1.3 μm, and is expected to advance low-cost and low power-consumption optical transmission systems. On the other hand, II-IV wide bandgap semiconductor quantum dots are suitable for the development of lasers in the visible light range. For instance, using CdS quantum dots, a group from Sandia National Laboratories reported the first white light-emitting device in 2003.[6] The characteristic discrete electronic states makes self-assembled QDs also attractive for spintronic and quantum computing applications since they exhibit extremely long phase and spin coherence times.[7,8,9,10,11]

The CdS nanowires investigated here were grown using another growth technique called chemical vapor deposition (CVD) and gold-catalyzed vapor-liquid-solid (VLS). In this process the gold catalyst determines the position and diameter of the nanowires. In recent years vapor-liquid-solid growth of nanowires has been developed in a number of semiconductor systems.[12,13,14] Indeed, several promising nanowire electronic devices have been demonstrated including electrical sensors[15], light emitting diodes[16], single photon emitters[17] and electrical injection lasers.[15,18]

Modeling and optimizing devices based on these semiconductor nanostructures depends critically on a detailed knowledge of the electronic states and their interactions in these quantum structures— knowledge which is presently limited. Simple photoluminescence experiments have been utilized to measure the ground states in these quantum wires (see, for instance, Ref. 13 and 19). Photoluminescence excitation

and photoconductivity measurements have been used extensively to probe the electronic structure of SAQDs, but these measurements also require coupling of confined energy states within the QD to a luminescent ground state or a delocalized continuum, respectively.[7,19,20,21] Standard optical absorption techniques are very challenging for such materials because of the small fractional coverage of the sample surface with quantum dots and nanowires, and have only been successfully applied for multilayers of dots, or waveguide geometries.[22] Hence, other tools which probe more complex electronic states are needed to more fully characterize these nanostructures.

Here resonant Raman scattering (RRS) is utilized to probe electronic states of the CdTe/ZnTe SAQDs and CdS nanowires. This technique has already been successfully used, for instance, to measure the diameter- and chirality-dependent electronic structure of single walled carbon nanotubes.[23]

This thesis is organized in the following way. In the next chapter, Chapter 2, a brief review of semiconductor nanostructures is provided. In particular, the effects of quantum confinement, the band structures of bulk CdTe and CdS, temperature dependence of the bandgap, and the energy distribution in quantum dots and nanowires are presented. In Chapter 3, Raman spectroscopy is considered in some detail. In this chapter, inelastic light scattering processes by phonons, Raman tensors and polarization selection a rules as well as resonant Raman scattering are discussed. The experimental methods employed, the major experimental components and the samples are described in Chapter 4. Chapter 5 and 6 are devoted to a presentation and discussion of the experimental results on the CdTe/ZnTe SAQDs and CdS nanowires, respectively. Finally, we conclude by presenting a summary of results in Chapter 7.

2 II-VI Semiconductor Nanostructures Overview

In this chapter we provide a brief overview of semiconductor nanostructures that will help us to understand the physical properties of CdTe/ZnTe QDs and CdS/Si QWRs that are the subject of this thesis. First we discuss the quantum confinement in low dimensional nanostructures in general. Subsequently we present the band structure and optical properties of both CdTe/ZnTe SAQDs and CdS nanowire samples.

2.1 Nanostructures

The phrase semiconductor nanostructures refers to condensed matter structures typically having dimensions less than Bohr radius of excitons or de-Broglie wavelength (usually less than 10 nm) and energy bandgaps ranging form 0 to 4 eV. In general, semiconductor nanostructures can be categorized into three groups based on their dimensionality. These are known as quantum wells (QWs), quantum wires (QWRs), and quantum dots (QDs) in decreasing order of their dimensionality. We have studied the electronic states and vibrational structures in two types of group II-IV semiconductor nanostructures namely CdTe/ZnTe QDs and CdS/Si QWR samples. The electronic and optical properties of these semiconductor nanostructures are significantly different from their bulk counterparts. The difference is mainly due to confinement effects that we now discuss in some detail.

2.2 Quantum Confinement

Fundamentally every solid consists of `10^{23} atoms/cubic centimeter. Solid materials can be mainly divided into groups of crystalline and amorphous structures according to the arrangement of their atoms or molecules. Atoms or molecules constituting crystalline structures are arranged in a periodic order whereas those forming amorphous solids have no long range order or periodicity. Both the CdTe/ZnTe QDs and CdS/Si QWRs samples we have studied are crystalline structures. Hence, in this thesis, semiconductor nanostructures or solids refer to crystalline semiconductor nanostructures or solids.

The idea and theory of using ultra-thin layers for the study of effects of size quantization was recognized in 1950s and early 1960s.[24] However, to demonstrate quantum size effect in ultra-thin layers, electrons have to be strongly confined in that region. If the interface is rough or if the interface has many defects, the chance of achieving size quantization would be minimal due to the collisional broadening of electron energy levels. High-quality interfaces are required to achieve a sufficiently long collision time needed for the energy spacing to be larger than the collisional broadening. The technology at that time was inadequate to observe size quantization effect experimentally in a rigorous way. Now it is possible to execute precise deposition of samples on a substrate monolayer by monolayer. This has enabled control of the size of layers at an atomic level, a size much less than the de-Broglie wavelength of the material.

It has been well-demonstrated experimentally that the size and shape of a semiconductor structure can affect its electronic and optical properties. [24,25] The effects of size quantization are more pronounced when the motion of carriers is restricted to a region comparable to their de-Broglie wavelength. That means carriers which are physically trapped in region on the order of a de-Broglie wavelength of the material will manifest quantum confinement. The de-Broglie wavelength λ depends on the effective mass m_{eff} of the carrier and temperature T as:

$$\lambda = \frac{h}{p} = \frac{h}{\sqrt{3\, m_{eff} kT}} \tag{2.1}$$

Where *h, p* and *k* are Planck constant, momentum and Boltzmann constant respectively. The effective mass m_{eff} of the carrier in the crystal is much smaller than the free electron mass.

A schematic of a 3D bulk material, a 2D quantum well, a 1D quantum wire and a quasi 0-D quantum dot are shown in of Fig. 2.1. Electrons in bulk structures, shown schematically in Fig. 2.1a, are free to move in all three dimensions. However, if a very thin layer on the order of the de-Broglie wavelength of the electrons in the material is sandwiched between other semiconductors of higher bandgap, as illustrated in Fig. 2.1b, the scenario is quite different. The higher bandgap semiconductors confine the motion of the electrons along one dimension. Since the dimension of the thin layer is very small, the electrons in this region behave like electrons in a potential well and thus the name quantum well. Electrons in a quantum well have discrete energy levels due to

the quantum mechanical confinement. In other words, the wave function of electrons confined to a very small spatial region is localized and leads to the formation of discrete energy states.

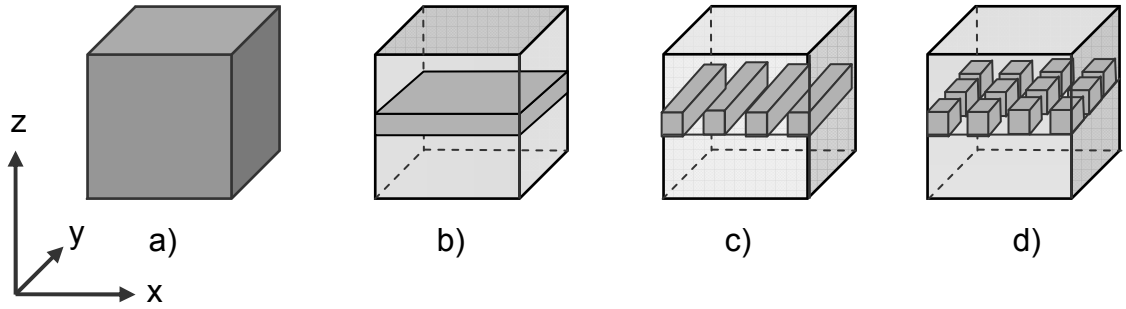

Figure 2.1: A schematic of a) bulk, b) quantum well, c) quantum wires, and d) quantum dots.[24,25]

In addition, confinement also affects the density of states significantly as shown in Fig. 2.2. The density of states is the number of allowed energy states per unit energy range. Bulk and quantum wells are the most widely used structures in today's semiconductor devices. We have to keep in mind that electrons in a quantum well are not confined in the other two dimensions and thus quantum well structures are also known as 2D nanostructures.

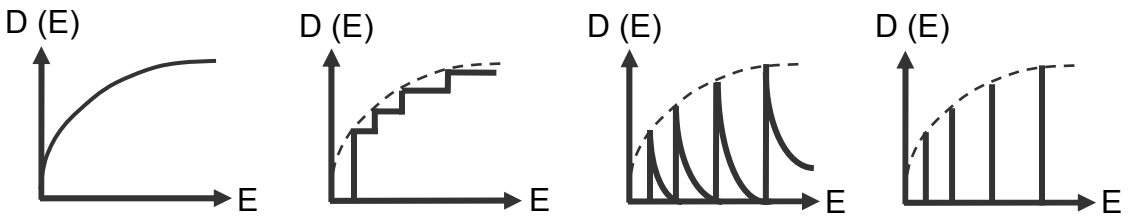

a) bulk b) quantum well c)quantum wire d) quantum dot

Figure 2.2: Density of electronic states corresponding to the schematics of Fig. 2.1 for a) bulk, b) quantum well, c) quantum wires, and d) quantum dots.[24,25] The horizontal axis is energy while the vertical is density of electronic states.

Even stronger confinement can be achieved by introducing two- and three-dimensional confinements of electrons as illustrated in Fig. 2.1c&d. In quantum wires, often called nanowires, illustrated in Fig. 2.1c, electrons are confined along two-dimensions but not localized along the third dimension and thus the name 1D nanostructures. The confinement effects are more pronounced in a quantum wire/1D nanostructure compared to quantum well/2D nanostructure. Carriers in quantum dots or 0D nanostructures, as shown in Fig. 2.1d, are completely localized in all three dimensions. This leads to discrete energy levels of carriers in 0D structures just like the electron in a hydrogen atom.

As has been said earlier, many physical properties of solids are attributed to the energy distribution of electrons in solids. Models like the free electron, Kroning-Penney and Tight-Binding models have been used to predict the band structure of solids. In

addition, powerful methods such as the effective mass and pseudopotential methods can be used to calculate band structures of materials.

Here we show an effective-mass method to calculate electronic energy states in quantum well. It will provide us with a picture of the semiconductors band structure which will be useful to have in mind. Let us first consider type I QW structure consisting of a thin layer **A** sandwiched between two barrier layers B (B/A/B). In type I QW structures the conduction band offset (ΔE_c) and the valence band offset (ΔE_v) have different signs as shown in Fig. 2.3. The electron wave function for a simple isotropic band is separable and can be written as[26]

$$\Psi(r) = \frac{1}{\sqrt{S}} e^{i k_{//} \bullet \rho} \varphi(z) \quad \cdots\cdots\cdots\cdots\cdots\cdots (2.2)$$

The Schrödinger equation in the well and the barrier layer, in the absence of the electron-hole coulomb interaction and without the spin-orbit interaction, can be written as

$$-\frac{\hbar}{2m_A} \frac{d^2 \varphi(z)}{dz^2} + \left[\frac{\hbar^2 \left(k_x^{\,2} + k_y^{\,2}\right) \varphi(z)}{2m_A} + V(z) \right] \varphi(z) = E \varphi(z), \quad |z| < L/2 \cdots (2.3)$$

$$-\frac{\hbar}{2m_B} \frac{d^2 \varphi(z)}{dz^2} + \left[\frac{\hbar^2 \left(k_x^{\,2} + k_y^{\,2}\right)}{2m_B} + V(z) \right] \varphi(z) = E \varphi(z), \quad |z| > L/2 \cdots (2.4)$$

where

$$V(z)=\begin{cases}0, & \text{for } |z|<L/2\\ V=\Delta E_c, & \text{for } |z|>L/2\end{cases} \quad \cdots\cdots\cdots\cdots\cdots (2.5)$$

m_A and m_B are carries effective mass in layers A and B respectively. The corresponding boundary conditions that relate the wave functions and their first derivative at the interface are given by:

$$\left.\begin{aligned}(\varphi(z))_A &= (\varphi(z))_B\\ \frac{1}{m_A}\left(\frac{d\varphi(z)}{dz}\right)_A &= \frac{1}{m_B}\left(\frac{d\varphi(z)}{dz}\right)_B\end{aligned}\right\} \quad \cdots\cdots\cdots\cdots (2.6)$$

Except for the fact that the masses m_A and m_B may be different, Eqs. 2.3 and 2.4 are identical to those in quantum-mechanics textbooks for a particle in a 1D finite square potential well. Eqs. 2.3 and 2.4 can have two types of solutions. In the case when $E - \frac{\hbar^2\left(k_x^{\,2}+k_y^{\,2}\right)}{2m_B} > \Delta E_c$, the electron energy spectrum contain continuous states. In the other case when $E - \frac{\hbar^2\left(k_x^{\,2}+k_y^{\,2}\right)}{2m_B} < \Delta E_c$, the electron energy spectrum has finite number of bound state. For the later case, the wavefunction $\varphi(z)$ can be written as

$$\varphi(z)=\begin{cases}Ae^{\alpha z}, & \text{for } z<-L/2\\ Be^{ikz}+Ce^{-ikz}, & \text{for } |z|<L/2\\ De^{-\alpha z}, & \text{for } z>L/2\end{cases} \quad \cdots\cdots\cdots\cdots\cdots (2.7)$$

where

$$\left.\begin{aligned} k &= \left[\frac{2m_A E}{\hbar^2} - \frac{\hbar^2\left(k_x^{\,2} + k_y^{\,2}\right)}{2m_B}\right]^{1/2} \\ \text{and } \alpha &= \left[\frac{2m_B(V-E)}{\hbar^2} + \frac{\hbar^2\left(k_x^{\,2} + k_y^{\,2}\right)}{2m_B}\right]^{1/2} \end{aligned}\right\} \quad \cdots\cdots\cdots\cdots\cdots\cdots (2.8)$$

Since the finite potential well is symmetric with respect to inversion of the z-axis, the parity of the wavefunction must be well defined. That means the wavefunction must be symmetric (even parity) or anti-symmetric (odd parity) under the inversion of the z-axis.

For the even solution, we can write the wave function as

$$\varphi(z) = \begin{cases} C\ \cos(kz), & \text{for } |z| \le L/2 \\ D\ e^{-\alpha(|z| - L/2)}, & \text{for } |z| \ge L/2 \end{cases} \quad \cdots\cdots\cdots\cdots\cdots\cdots (2.9)$$

Using Eq.(2.9), the boundary conditions Eq. (2.6) and Eqs. (2.3) & (2.4), we can obtain the transcendental equation for the energy of the even solutions:

$$\tan\left(k\frac{L}{2}\right) = \eta \equiv \frac{m_A\,\alpha}{m_B\,k} \quad \cdots\cdots\cdots\cdots\cdots\cdots (2.10)$$

For the odd parity solution, the wave function has the form

$$\varphi(z)=\begin{cases} C\ \sin(kz), & \text{for } |z| \le L/2 \\ D\sinh\{z\}\ e^{-\alpha(|z|\ -\ L/2)}, & \text{for } |z| \ge L/2 \end{cases} \quad \cdots\cdots\cdots\cdots\cdots\cdots (2.11)$$

and the corresponding energy is

$$\cot\left(k\frac{L}{2}\right) = -\eta \quad \cdots\cdots\cdots\cdots\cdots\cdots (2.12)$$

The graphical solutions of this an overly simplified particle in a box model is found in most quantum-mechanics textbooks. The number of bound state depends on ΔE_c. At least one bound state exists for arbitrary value of ΔE_c, in case of even parity. For odd bound state to exist ΔE_c must be greater than $\frac{\pi^2\hbar^2}{2m_A\ L_z^2}$. Schematics of the wavefunctions for the first three quantum confined states and energy distribution in QW are shown in Fig. 2.3.

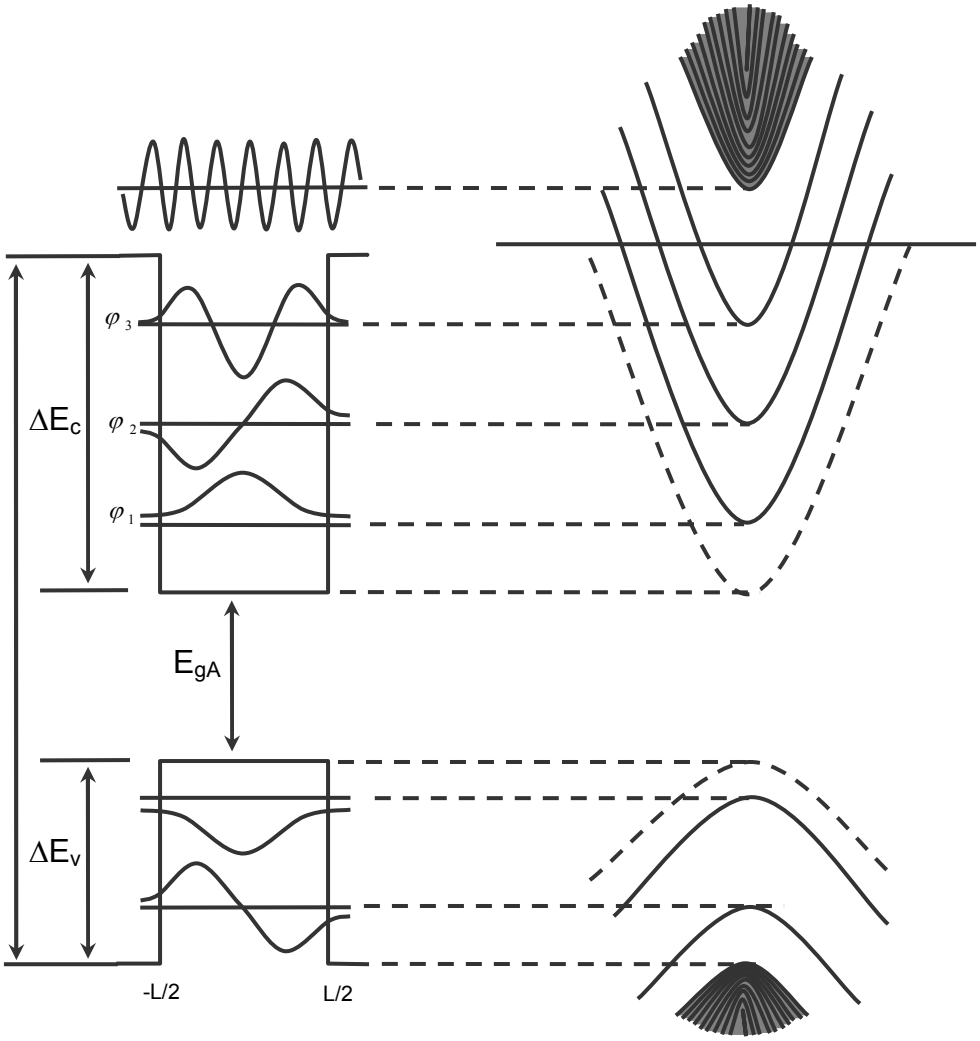

Figure 2.3: A schematic representation of electron and hole wave functions and energy dispersion for a quantum well. [26]

The average diameters of the CdTe quantum dots and CdS nanowires we have studied are 3 nm and ~10 nm respectively. [27,28] The calculated exciton Bohr radii of CdTe and CdS are 10 nm and 3 nm respectively.[27,29] This suggests that the electron and hole states in the CdTe SAQDs exhibit strong quantum confinement where as those in the CdS nanowire may exhibit only modest quantum confinement.

2.3 Physical Properties of Solids

The electronic and optical properties of most bulk semiconductors, where electrons can be treated as free particles, are extensively studied and well-known. Electrons in bulk solids are arranged in nearly continuous energy bands separated by a forbidden energy region called an energy gap or bandgap. The bandgap is the energy difference between the minimum point on conduction band and maximum point on valence band. The plot of electron energies versus wave vector k is known as the electronic band structure of the crystal. Semiconductors are also categorized into two main groups based on the relative position of the conduction band minimum and the valance band maximum in k space as shown in Fig. 2.4. When the conduction band minimum and the valance band maximum occur at the same point in k space, the semiconductor is called a direct-gap semiconductor. On the other hand, when the conduction band minimum and the valance band maximum occur at a different point in k space, the semiconductor is called indirect-gap semiconductor. GaAs and InSb are among commonly mentioned examples of direct-gap semiconductors while Si and Ge are two important examples of indirect-gap semiconductors. The CdTe/ZnTe SAQDs and CdS nanowire studied for this thesis are both direct-gap semiconductor nanostructures.[30]

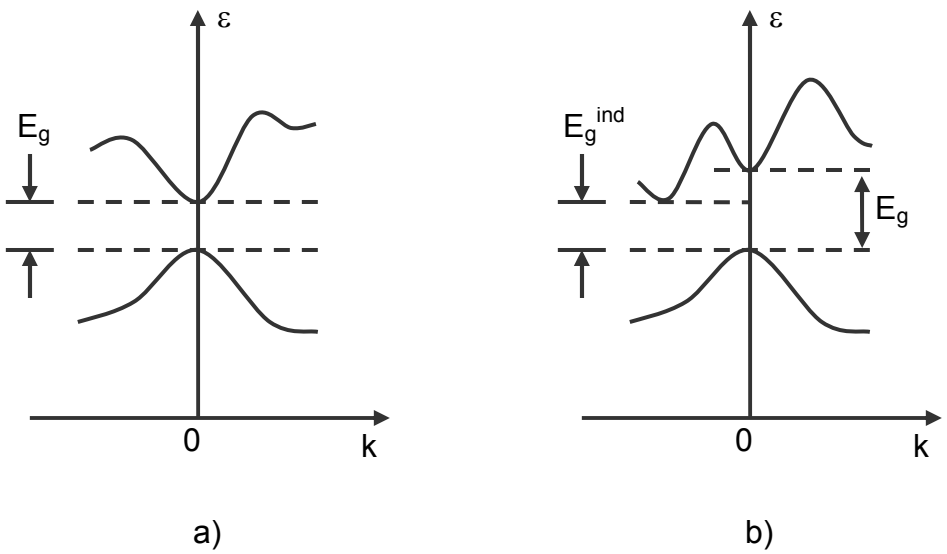

Figure 2.4: A schematic of a) direct- and b) indirect-gap semiconductors. The direct- and the indirect-gap energies are denoted by E_g and E_g^{ind} respectively.

2.4 Band Structures of CdTe & CdS and the effect of Temperature on the Bandgap

2.4.1 Band Structure of Bulk CdTe

The bulk CdTe energy band structure calculated near the fundamental bandgap is illustrated in Fig. 2.5. The electronic and optical properties of semiconductors are interrelated. Specifically, light absorption and emission are distinctively determined by the semiconductor band structure and in particular the bandgap. Thus, if one wants to understand the light emission process, it is essential to first understand the electronic

properties of the mobile carriers, i.e. the electrons in semiconductors. Using different techniques several groups have reported that the bandgap of bulk CdTe is 1.6 eV at low temperature.[30] For instance, a bandgap of 1.59 eV is obtained at 15 K using reflectivity measurements[31] and a bandgap of 1.6 eV is measured at 25 K using ellipsometry measurements.[32]

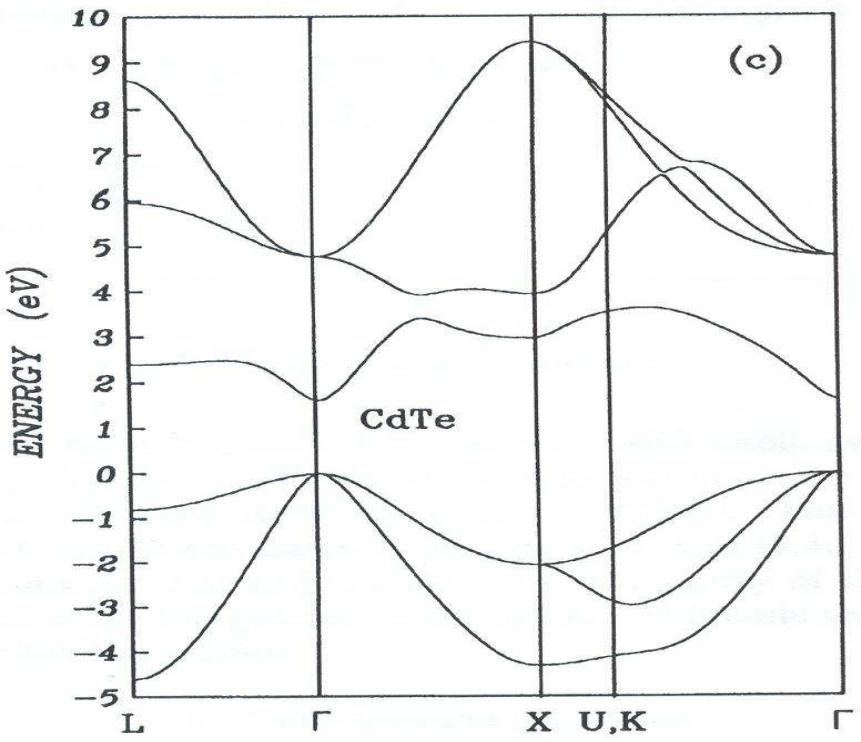

Figure 2.5: Band structure of bulk cubic CdTe along the principal symmetry direction of the fcc Brillouin zone.[33]

In order to conserve momentum, only phonon excitations with nearly zero momentum are involved in the Raman process. Hence, using resonant Raman scattering we are going to be looking near the zone center (Γ point) since the momentum is zero at this point.

2.4.2 Band structure of CdS

Figure 2.6 is the band structure of bulk CdS calculated in a sophisticated way by the use of self-interaction-corrected pseudopotentials in the local-density approximation. The calculated bandgap of CdS at room temperature is found to be 2.5 eV.[34] Ninomiya and Adachi have also measured the bandgap of bulk CdS to be 2.482 using ellipsometry techniques at room temperature.[35] Singh's group as reported a value of 2.37 eV using reflectance measurements.[34] Another group has reported 2.43 eV using photoluminescence measurements at 300 K.[36] We have measured a value of 2.45 eV for the CdS nanowires using photoluminescence measurements at room temperature.

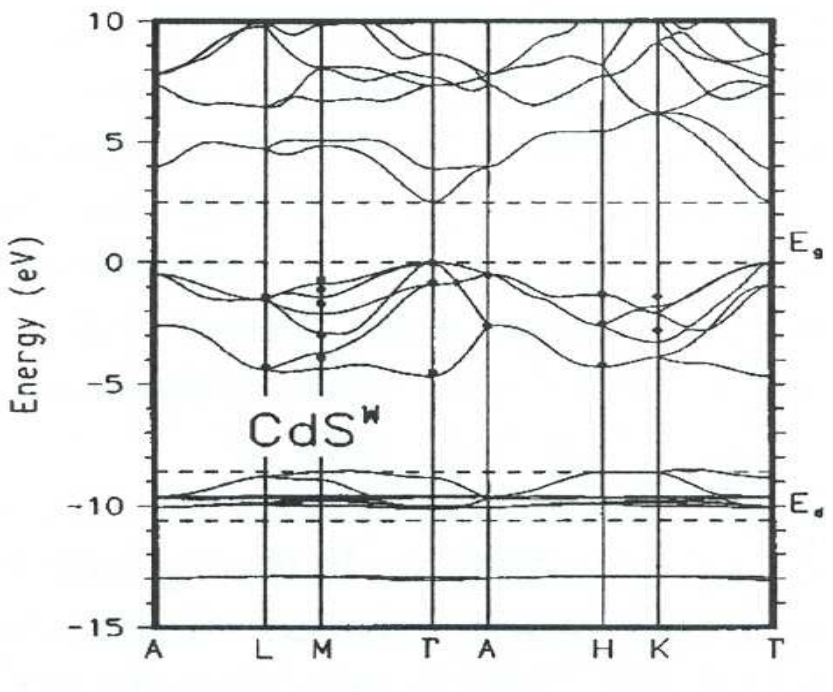

Figure 2.6: Band diagram for bulk wurtzite CdS in the principal symmetry direction calculated by the use of self-interaction-corrected pseudopotentials in local-density approximation.[37]

2.4.3 Photoluminescence

When a sample is excited by laser light that has photon energy higher than the bandgap of the sample, electrons will be excited from the valence band into the conduction band leaving a hole behind in the valence band. Photoluminescence (PL) from a direct bandgap semiconductor occurs when a free electron and hole relax to the bottom of the band, and consequently recombine and emit a photon. The energy of the emitted light, the PL, which involves the transition of free electrons from the minimum of the conduction band to the maximum of the valence band, is simply the bandgap energy. The PL process is illustrated schematically in Fig. 2.7. Electrons excited to virtual states higher than the minimum conduction band, as shown in Fig. 2.7, usually relax to the bottom of the conduction energy through the emission of phonons. This process is called momentum relaxation.

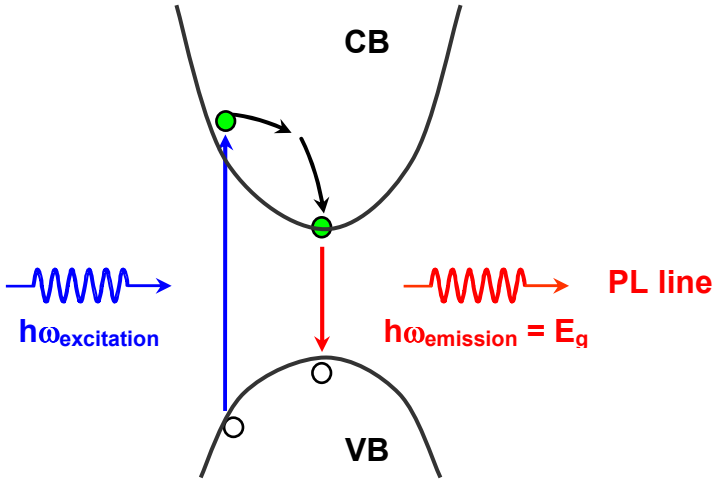

Figure 2.7: Schematic of photoluminescence process.

There is a strong possibility that the free electron-hole pair recombine before relaxing to the bottom of the band (k=0). In this case, the emission energy will be greater than the bandgap. On the other hand, the electrons and the holes may form bound states called excitons, a bound electron-hole pair. As a result, the emission energy can be less than the bandgap by excitons binding energy. The energy of the PL from CdS nanowire that is measured at room temperature reflects the ground state.

2.4.4 Temperature Dependence of Bandgap

The bandgap of semiconductors decreases with increasing temperature. This dependence of the energy bandgap of semiconductor on temprature results from thermal expansion and the electron-phonon interaction. We have carried out a temperature dependent PL measurement to determine the ground state of the CdTe quantum dots at room temperature. The temperature dependence of the bandgap of semiconductor is usually expressed by an empirical relation known as the Varshni equation:[38]

$$E_g(T) = E_g(T=0) - \frac{\alpha T^2}{\beta + T} \quad \cdots\cdots\cdots\cdots\cdots (2.13)$$

where α and β are the temperature coefficients and E_g (T), is the temperature dependent bandgap.

However, Eq. (2.13) leads to asymptotic behavior at low temperature that is not

observed. We should note that the equation fits at higher temperatures where the condition β/T << 1 holds.[39,40] In this case, Eq. 2.13 might be even approximated with a linear equation for T >> β (usually above 100 K as shown in Fig 2.8). In general β is proportional to the Debye temperature (Θ_D). Using a model β=0.375Θ_D after Manoogian and Woolley[40] and the Debye temperature (Θ_D)=158 K for CdTe[41], we obtain β=59K for CdTe. This suggests that Varshni empirical equation (Eq. 2.13) provides a reasonable fit for temperature dependent PL from CdTe SAQDs in the region of interest.

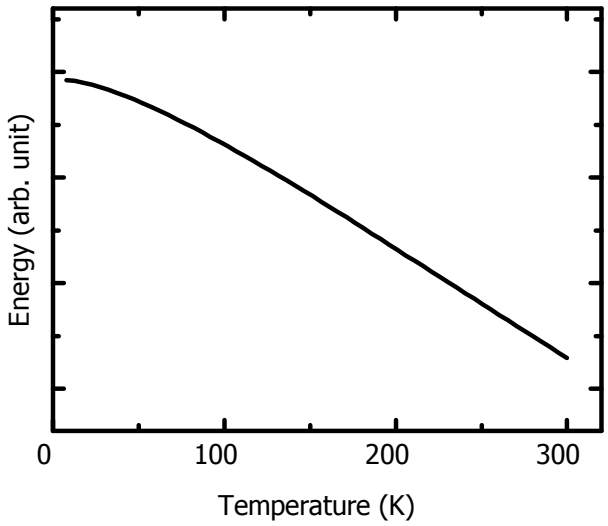

Figure 2.8: Schematic of photoluminescence process.

As said earlier, the bandgap shift with temperature arises due to thermal expansion of lattice with temperature and the direct renormalization of band energies due to electron-phonon interaction. The shift of bandgap due to thermal expansion are usually determined using hydrostatic pressure dependent bandgap experiments under

high presure. On the other hand, the effect of the electron-phonon interaction is calculated from perturbation theory by Cardona and others.[39,42] They have demonstrated that the dependence of the bandgap on temperature is ~T^4 and also argued based on the Debye's model that has an asymptotic behavior like T^4.

2.5 Energy Distribution in quantum dots and Nanowires

Carriers in quantum dots are confined in all directions within a spatial dimension comparable to the exciton Bohr radius. This confinement underlines that the effect of dimensionality and is manifested in the physical properties of quantum dots. Here, we would like to know how the electron states are distributed in a quantum dot structures. There are atomistic level theoretical calculations of the energy distribution in spherical quantum dots such as tight-binding [[43]] and the pseudopotential method.[[44]] In particular, the assignment of the electronic states based on the effective mass theory has provided a strong foundation for a description of the electronic structure in quantum dots.[45,46,47] Hence, we would like to present a calculation of electronic states in spherical quantum dots (QDs) and cylindrical quantum wires (QWRs) based on the effective mass theory. That will provide us with the knowledge of the distribution of electronic states in the CdTe QDs and the CdS nanowires which will be used in the analysis of our results later.

First, let us consider a spherical QD of material A surrounded by a substrate of different material B. The Hamiltonian and the potential energy of a carrier in a centrosymmetric finite potential are given by[24,26]

$$H\Psi(r)=\left\{\nabla\frac{\hbar^2}{2m_i}\nabla+V(r)\right\}\Psi(r) \text{ and } V(r)=\begin{cases}-V, & \text{for } r\le R\\ 0, & \text{for } r>R\end{cases} \quad \cdots\cdots\cdots\cdots\cdots\cdots (2.14)$$

where m_i stands for the effective masses of the carriers in the dot and the barrier layers, m_A and m_B respectively.

The wave function can be separated in radial and angular components $\Psi(r)=R_{nlm}(r)Y_{lm}(\vartheta,\phi)$, where Y_{lm} are the spherical harmonic functions. For the ground state (n=1) the angular momentum l is zero and the solution for the wavefunction is given by

$$R(r)=\begin{cases}\dfrac{\sin(kr)}{kr}, & \text{for } r\le R\\ \dfrac{\sin(kR)}{kR}\exp[-\kappa(r-R)], & \text{for } r>R\end{cases} \quad \cdots\cdots\cdots\cdots\cdots\cdots (2.15)$$

where

$$k^2=\frac{2m_A(V+E)}{\hbar^2} \qquad \text{and} \qquad \kappa^2=\frac{2m_B(-E)}{\hbar^2} \cdots\cdots\cdots\cdots\cdots\cdots (2.16)$$

Using the boundary conditions like Eq. 2.6 that require both R(r) and $(1/m_i)[\partial R(r)/\partial r]$ to be continuous across the interface at r=R, we can obtain the equation that should be satisfied by the energy states.

$$kR\cot(kR) = 1 - \frac{m_A}{m_B}(1 + \kappa R) \quad \cdots\cdots\cdots\cdots\cdots\cdots (2.17)$$

Using Eq. (2.17), one can determine the allowed ground state in a spherical quantum dot. The minimum potential V_{min} needed to confine at least one bound state can be written as

$$V_{min} < -\frac{\pi^2 \hbar^2}{8m^* R^2} \quad \cdots\cdots\cdots\cdots\cdots\cdots (2.18)$$

where $m_A = m^*$. Generally for all angular momentum, the wavefunctions are given by spherical Bessel functions j_l in the dot and spherical Hankel functions h_l in the barrier. Tran Thoai et. al.[48] (1990) gave the transcendental equation for the energy of the exited state level:

$$kR\cot(kR) = 1 - + \frac{k^2R^2}{\frac{m_A}{m_B}\frac{2 + 2\kappa R + \kappa^2 R^2}{1 + \kappa R} - 2} \quad \cdots\cdots\cdots\cdots\cdots\cdots (2.19)$$

Second, consider cylindrical QWR of material A surrounded by substrate of different material B. In the effective mass approximation, the 1D-electron wavefunction for cylindrical nanowire is written as[26]

$$\Psi(r) = \frac{1}{\sqrt{L}} e^{ik_z Z} \varphi(x, y) = \frac{1}{\sqrt{L}} e^{ik_z Z} \varphi(\rho, \phi) \cdots\cdots\cdots\cdots\cdots\cdots (2.20)$$

where z is the QWR principal axis and L is its length. Note that the cylindrical coordinates are related to rectangular coordinates by $\rho = \sqrt{x^2 + y^2}$ and ϕ (the azimuth angle) given by tan(y/x). The boundary conditions for the QWRs can be arranged as

$$\varphi_A = \varphi_B , \qquad \frac{1}{m_A} (\mathbf{N}.\nabla\varphi)_A = \frac{1}{m_B} (\mathbf{N}.\nabla\varphi)_B \quad \cdots\cdots\cdots\cdots\cdots\cdots (2.21)$$

where N is the normal to the dividing surface between materials A and B, and masses m_A and m_B are masses of carriers in materials A and B respectively.

The electron states in a cylindrical QWR are characterized by the z-component of the angular momentum (M). For the axially-symmetric state with M=0, the function $\varphi(x, y) \equiv \varphi(\rho)$ is expressed via the Bessel functions $J_0(x)$ and $K_0(x)$ as follows

$$\varphi(x, y) = \begin{cases} C J_0(\kappa\rho), & \text{if } \rho \le R \\ D K_0(\alpha\rho), & \text{if } \rho \ge R \end{cases} \quad \cdots\cdots\cdots\cdots\cdots\cdots (2.22)$$

where R is the wire radius, κ and α are related with the energy by the equations

$$\kappa = \left(\frac{2m_A E}{\hbar^2} - k_z^2 \right)^{1/2}, \; \alpha = \left(\frac{2m_B (V - E)}{\hbar^2} + k_z^2 \right)^{1/2} \quad \cdots\cdots\cdots\cdots\cdots\cdots (2.23)$$

Using the boundary condition of Eq. (2.21), we can show that

$D = C\,J_0(\kappa R) / K_0(\chi R)$ and obtain the following equation for the electron energy

$$\frac{J_1(\kappa R)K_0(\alpha R)}{J_0(\kappa R)K_1(\alpha R)} = \frac{\alpha\, m_A}{\kappa\, m_B} \quad \cdots\cdots\cdots\cdots\cdots\cdots (2.24)$$

In the QWR with an infinite confining potential, when the wave function at the boundary can be set to zero, this equations reduces to $J_0(\kappa R) = 0$. The fist three zeros of the function $J_0(x) = 0$ are 2.405, 5.520 and 8.654.

In general, according to a simple effective-mass approximation model, the bandgap increase of QDs and QWRs from the bulk value are

$$\Delta E_g = \frac{2\,\hbar^2\,\xi^2}{m^*\,D^2} \quad \cdots\cdots\cdots\cdots\cdots\cdots (2.25)$$

where

$$\frac{1}{m^*} = \frac{1}{m_e^*} + \frac{1}{m_h^*}$$

m_e^* and m_h^* are electron's and hole's effective masses, respectively, and D is the QDs and QWRs average diameter. For spherical QDs, $\xi = \pi$ is the zero point of the spherical Bessel function, while for cylindrical QWRs, ξ = 2.4048 is the zero point of the cylindrical Bessel function. Thus the ratio of bandgap increase between the QWRs and QDs with the same size D should be $\Delta E_g^{wire} / \Delta E_g^{dot}$ =0.586.[49]

Keeping in mind that all of the materials are the same except the size and distribution, we show schematically in Fig. 2.9 how the electronic states of materials changes due to confinement. In particular, we demonstrate that separation between energy states increases with confinement. The energy states in bulk materials are continuous whereas those in the quantum wells are discrete but with smaller separation as compared to those in quantum wires. The quantum dots with the strongest confinement have the largest energy separation.

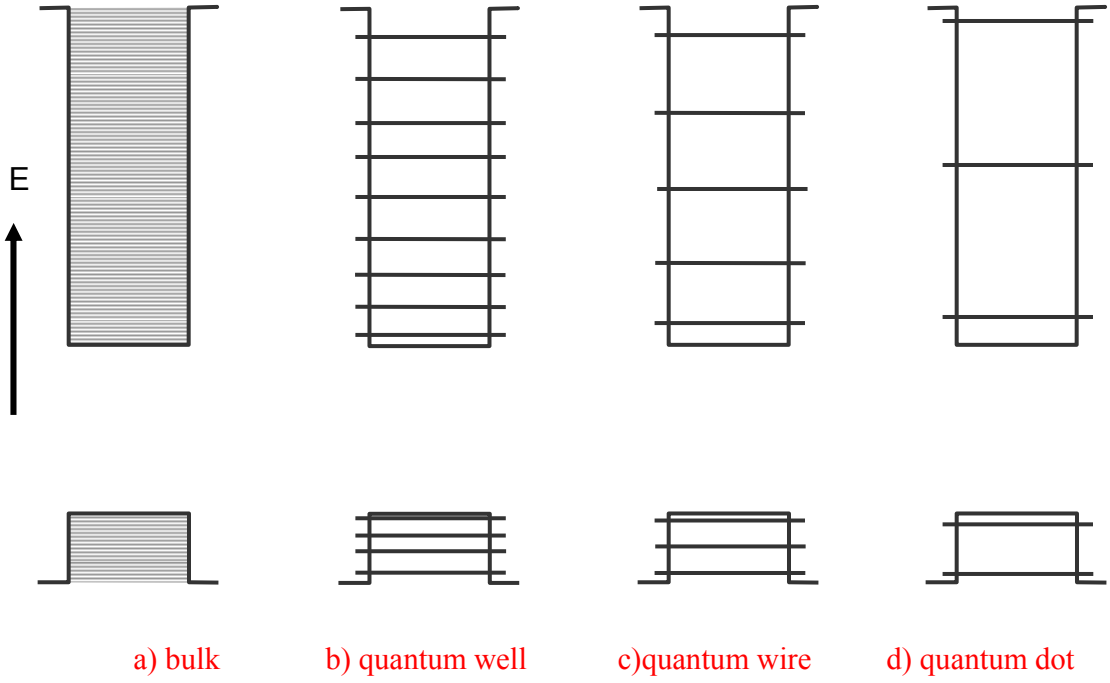

Figure 2.9: Schematic of energy diagram for a) bulk, b) quantum well, c) quantum wire and d) quantum dot. Due to strong confinement of carriers in quantum dots, the energy separation between states in this structure is the largest.

We have presented the effect of confinement on the distribution of electronic states that would be useful later. The band structure of bulk CdTe and CdS that has been discussed will be helpful to infer the physical properties of the CdTe quantum dots and CdS nanowires samples. The temperature dependence of the bandgap of semiconductors was briefly discussed. It will be used later to determine the energy band gap of CdTe SAQDs at room temperature using temperature dependent PL measurements.

3 Raman Spectroscopy: a brief overview

Here we present a brief overview of Raman scattering spectroscopy. First, we summarize some of the major applications of Raman spectroscopy. Subsequently, we discuss phonons in a diatomic lattice. Then, we present a concise discussion of the theory of inelastic light scattering by phonons from a macroscopic point of view. Next, we proceed to provide both Raman tensors and polarization selection rules. Finally, we present a short overview of resonant Raman scattering principles.

3.1 Applications of Raman Spectroscopy

Today, Raman spectroscopy is extensively used in a wide variety of scientific areas and has provided a wealth of information on material properties. In particular, Raman scattering and resonant Raman scattering have become standard spectroscopic tools for the study and characterization of semiconductors. Although a detailed discussion of all the applications of Raman scattering will not be provided here, we will mention a few of the significant applications to semiconductors. Raman spectroscopy provides us with a probe of crystalline structure, strain, interface disorder and the effects of alloying.[50] In addition, Raman scattering is frequently employed as a tool to investigate vibrational and electronic properties, as well as the electron-phonon coupling in semiconductors.[51] For instance, resonant Raman scattering (RRS) has been used to great effect in single walled carbon nanotubes to measure their electronic structure which is dependent on the tube diameter and chirality.[23] RRS provides insight into

electron-phonon interactions,[52,53] and has been a sensitive probe of strain in hetrostructures.[54] The ratio of Stokes to anti-Stokes intensity serves as a measure of temperature which makes Raman scattering useful as a contactless thermometer.[55,56] Raman scattering is also used to monitor deposition processes.[57,58] The power of RRS as a means to probe the vibrational and electronic states in CdTe quantum dots and CdS nanowires is demonstrated in this thesis. Raman scattering is an inelastic light scattering process in which energy is transferred between the incident light and elementary excitations in the sample. The transferred energy matches the energy of an elementary excitation in the sample such as a phonon, a polariton, a plasmon, a coupled plasmon phonon mode or a single electron or hole excitation.[59] In our case the energy is transferred between the incident light and a phonon in the sample. In the next section we will present a simplified way of understanding phonons in crystals.

3.2 Crystal Vibration for a Diatomic Basis

The interaction of atoms in real solids is a complicated subject that both experimentalists and theoreticians study. In general, systematic approximations and assumptions are involved in the efforts to understand these interactions. Here we consider a simplified first order harmonic approximation of the interaction between atoms since their displacement from equilibrium is very small. When the displacements of atoms from equilibrium positions are very small, the higher order terms in the expansion of of the interaction with displacement can be excluded. Let us consider a crystal composed of a two atom basis. We may think of the case where atoms, M_1 and

M_2, lie on alternating planes as shown in Fig. 3.1 undergoing a longitudinal vibration. We assume that each plane of atoms vibrates in phase along the direction of ***k***. That is, we assume all atoms of mass M_1 lying on a plane oscillate together, while all atoms of mass M_2 lying on a plane also oscillate in phase.[60]

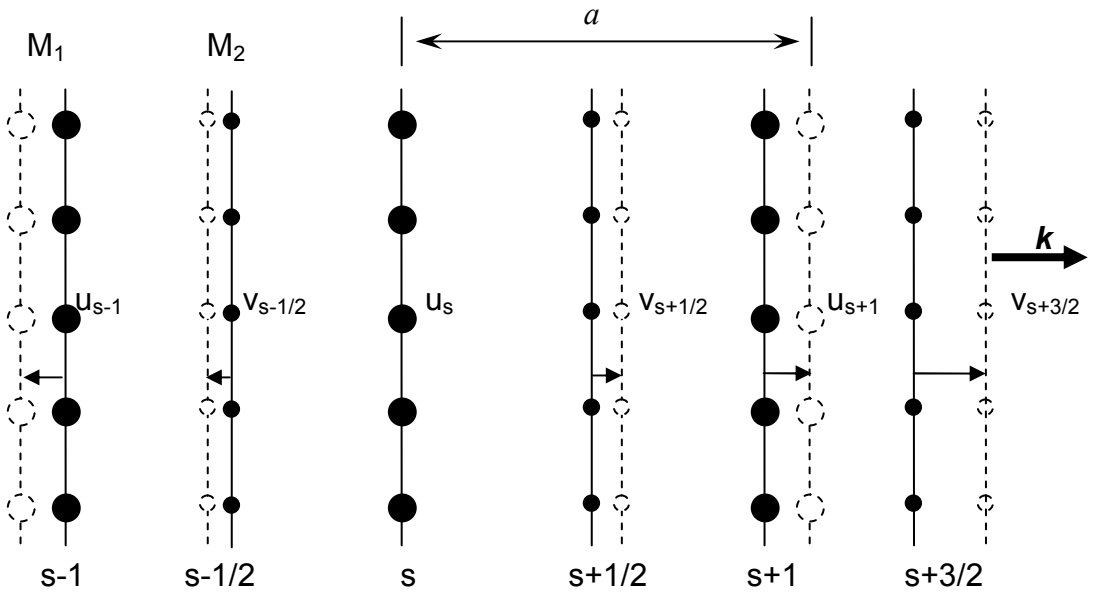

Figure 3.1: Longitudinal vibration of a diatomic crystal. The dashed lines stand for the planes of atoms displaced from equilibrium, while the solid lines represent the planes of atoms in equilibrium. The variables u_s and $v_{s+1/2}$ represent the displacements of the planes of atoms M_1 and M_2 from equilibrium positions respectively.[60]

We further assume that the force constants are nonzero only for nearest-neighbor interactions and also that the force constants are identical between all pairs of nearest-neighbors. Implementing the above assumptions, we get the following equation

of motion for the atomic planes of atoms M_1 and M_2.

$$\left.\begin{aligned} M_1 \frac{d^2 u_s}{dt^2} &= C\left(v_{s+1/2} + v_{s-1/2} - 2u_s\right) \\ M_2 \frac{d^2 v_{s+1/2}}{dt^2} &= C\left(u_{s+1} + u_s - 2v_{s+1/2}\right) \end{aligned}\right\} \qquad (3.1)$$

Again, u_s and $v_{s+1/2}$ represent the displacements of the planes of atoms M_1 and M_2 from equilibrium positions respectively. Let us consider traveling wave solutions of the form

$$\left.\begin{aligned} u_s &= U\exp\left[i(ska - \omega t)\right] \\ v_{s+1/2} &= V\exp\left[i(k\{s+1/2\}a - \omega t)\right] \end{aligned}\right\} \qquad (3.2)$$

with U and V are amplitude of oscillation of the planes of atoms M_1 and M_2 respectively, and a is the repeat distance between identical atomic planes. Substituting Eq. (3.2) into (3.1) and solving the resulting equations simultaneously, we obtain the dispersion relation for the nearest-neighbor interaction to be

$$\omega^2 = \frac{\mathbf{C}\left(\mathbf{M_1} + \mathbf{M_2}\right) \pm \left[\mathbf{C^2}\left(\mathbf{M_1} + \mathbf{M_2}\right)^2 - 4\mathbf{C^2}\left(\mathbf{M_1}\,\mathbf{M_2}\right)\,\mathbf{sin}^2\left(\frac{1}{2}\mathrm{ka}\right)\right]^{1/2}}{\mathbf{M_1}\,\mathbf{M_2}} \qquad (\mathbf{3.3})$$

The solutions to Eq. (3.3) are two modes of vibrations designated as ω_-^2 and ω_+^2. The first group of vibrations with frequency ω_-^2 is known as acoustic modes. In the case

of acoustic modes, different atomic planes, M_1 and M_2, move in same direction. The second sets of vibrations with ω_+^2 are called optical modes where the different atoms move in opposite directions. The quanta of these vibrational modes in a crystal are called phonons. The phonon dispersion, a plot of frequency of vibration versus wavenumber, is illustrated in Fig. 3.2 for longitudinal vibrations. The longitudinal optical (LO) phonon mode and the longitudinal acoustic (LA) phonon mode are separated by a forbidden frequency region at the zone boundary. The optical phonon branch appears at higher frequency and is less dispersive than the acoustic mode. Photons may be scattered inelastically by both optical and acoustic phonons. The scattering of photons from the acoustic phonon is called Brillouin scattering, whereas the scattering of photons from optical phonons is called Raman scattering.

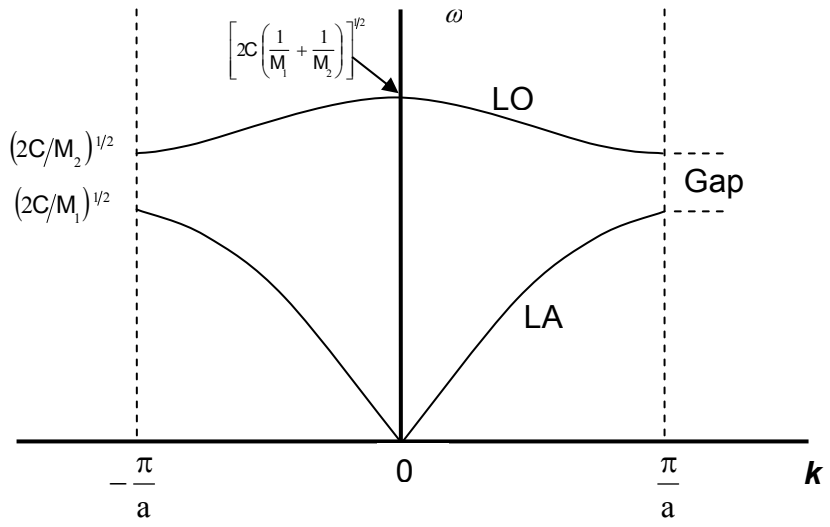

Figure 3.2: Dispersion curves for longitudinal optical (LO) and longitudinal acoustic (LA) modes.

Obviously atoms in crystals are not restricted to move only along the direction of ***k***. If the atoms in crystals oscillate perpendicular to ***k***, we obtain transverse optical (TO) and transverse acoustic (TA) modes. Generally in a substance characterized by P atoms, there exists a group of acoustic (one LA and two TA) modes together with P-1 groups of optical (one LO and two TO) modes as shown in Fig. 3.3.

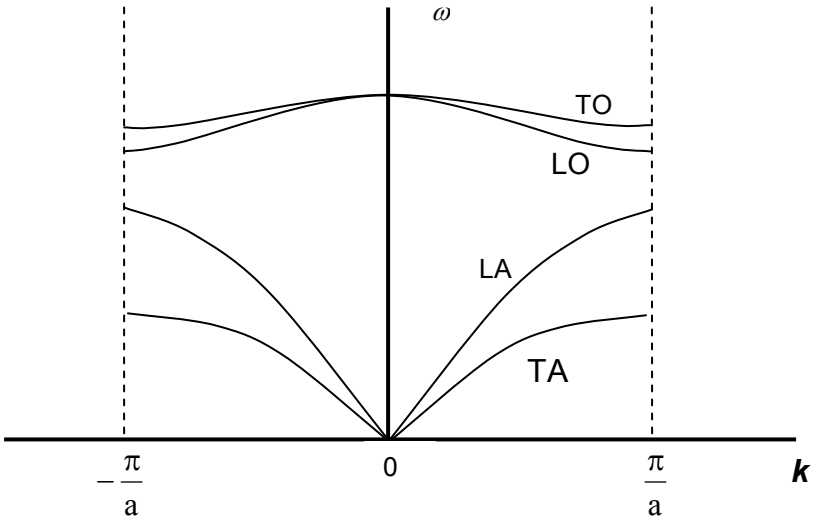

Figure 3.3: Dispersion curves for longitudinal and transverse optical and acoustic modes.

In ZnTe, the TO and LO phonon Raman frequencies are approximately 165 and 202 cm^{-1} respectively at the zone center.[61] The CdS LO phonons associated with a backscattering geometry are reported to be 305 cm^{-1}.[62]

3.3 Inelastic Light Scattering Process by Phonons

When light is shined on a material, most photons are elastically scattered. This elastic scattering process, in which the scattered photons have the same energy as the incident photons, is known as Rayleigh scattering. On the other hand, a very small fraction of photons (approximately 1 in 10^7 photons) are inelastically scattered. The inelastic scattering process that involves scattering of photons at energies (frequencies) other than the incident photon is called Raman scattering, after the Indian physicist C. V. Raman who discovered the effect in 1928.[63,64] A schematic of an energy level diagram for the Raman scattering process is presented in Fig. 3.4. Raman scattering is an inelastic scattering of a photon in which an optical phonon is either created or annihilated. This means that in this process, after interacting with the material, the scattered photon appears with an energy different from the incident photon. The energy difference between the incident and Raman scattered photons is equal to the energy of the scattering crystal lattice vibration or phonon. In Stokes Raman scattering, the energy of the scattered photon is less than that of the incident photon, i.e., scattered photon has longer wavelength than that of the incident photon. However, there is a possibility that a phonon is annihilated and transfers its energy to the scattered photon. In such a case, scattered photon appears with higher energy (shorter wavelength) than the incident photon, and the effect is known as anti-Stokes Raman scattering.

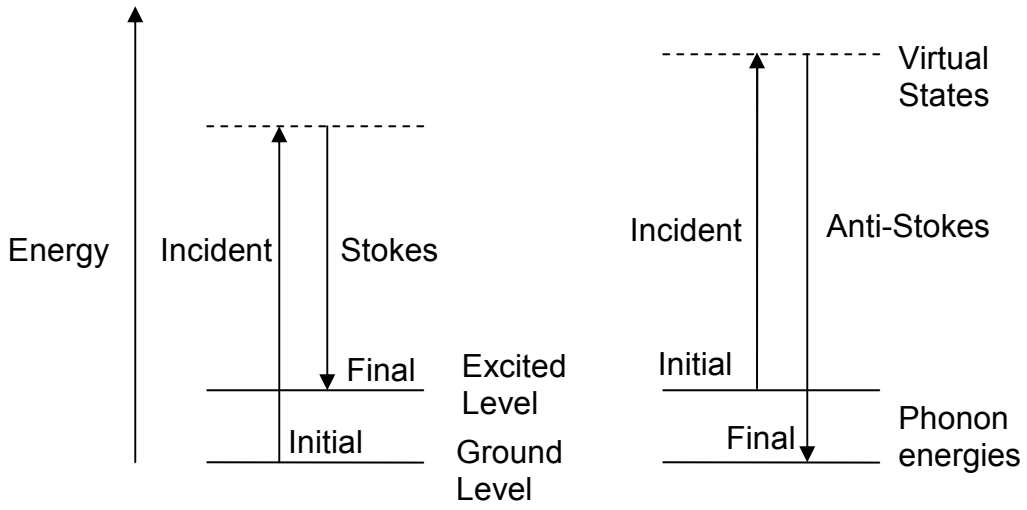

Figure 3.4: An energy level diagram for Stokes and Anti-Stokes Raman scattering.[65]

A schematic representation of the Raman process is illustrated in Fig. 3.5. In the backscattering geometry, the incident and the scattered light are along the same line. This implies that the phonon excitation should also lie along the backscattering direction to conserve momentum.

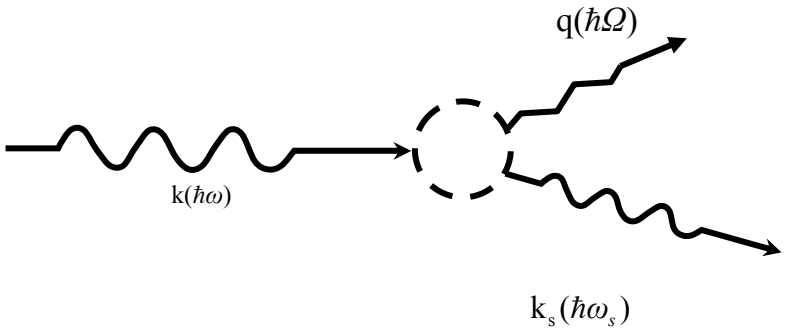

Figure 3.5: A diagrammatic representation of the Raman process. The broken circle represents the virtual electronic state, the wave and zigzag lines represent the photons and phonons respectively.

The Raman shift as a result of the scattering is often reported in wavenumber (cm^{-1}) which can be calculated using the equation

$$\text{Raman Shift}\left(cm^{-1}\right) = \left(\frac{1}{\lambda_{incident}} - \frac{1}{\lambda_{scattered}}\right) \times 10^{7} \qquad (3.4)$$

where the incident and Raman scattered photon wavelength ($\lambda_{incident}$ and $\lambda_{scattered}$ respectively) are in nanometers. In Raman spectroscopy, the intensity of the Raman scattered photons is also usually plotted as a function of wavenumber. A Raman spectrum is a plot of the intensity of Raman scattered photons versus the Raman shift (energy). We should note at this point that for Raman scattering from phonons to be allowed, both polarizability and symmetry of a material must be considered. In the following sections, we will discuss this in more detail.

3.4 Macroscopic Theory of the Raman Scattering Process

Many of the important features of Raman scattering can be explained using a simple classical interaction model of an incident electromagnetic wave with an induced electric dipole moment. In a simplified heuristic manner, we will provide a discussion of the interaction of electric field of the light with the sample. After discussing induced polarization, we will provide the calculated intensity of the scattered light that depends on polarization selection rules and symmetry of samples, and write it in tensor form.

The electric field of the incident radiation induces an electric dipole moment in a

material. The induced electric dipole moment, **P**, is directly proportional to the electric field as[51,66]

$$\mathbf{P} = \tilde{\chi}\,\mathbf{E} \tag{3.5}$$

The proportionality constant $\tilde{\chi}$ is the polarizability tensor of the medium or dielectric susceptibility tensor. Suppose the incident plane electromagnetic radiation in the medium is given by

$$\mathbf{E}(\boldsymbol{r},\mathrm{t}) = \mathbf{E}(\boldsymbol{k},\omega)\,\boldsymbol{cos}(\boldsymbol{k}\cdot\boldsymbol{r}-\omega\mathrm{t}) \tag{3.6}$$

where $\boldsymbol{k}$ and ω in this expression are wavevector and frequency of the incident radiation, then the induced polarization having the same frequency and wavevector as the incident photon can be described by

$$\mathbf{P}(\mathbf{r},\mathrm{t}) = \mathbf{P}(\boldsymbol{k},\omega)\cos(\boldsymbol{k}\cdot\boldsymbol{r}-\omega\mathrm{t}) \tag{3.7}$$

The polarizability is a measure of how the medium responds to an electric field and acquires an induced electric dipole moment. This means that the polarizability also depends on wavevector and frequency of the radiation. Consequently, the amplitude of the polarization is given by

$$\mathbf{P}(\boldsymbol{k},\boldsymbol{\omega}) = \tilde{\chi}(\boldsymbol{k},\omega)\,\mathbf{E}(\boldsymbol{k},\omega) \tag{3.8}$$

When the medium is at a finite temperature, there are thermally excited atomic vibrations or phonons. The atomic displacements **Q** can be written

$$\mathbf{Q}(\mathbf{r},\mathrm{t}) = \mathbf{Q}(\boldsymbol{q},\Omega)\, cos(\boldsymbol{q}\cdot\boldsymbol{r}-\Omega\mathrm{t}) \tag{3.9}$$

where $\boldsymbol{q}$ and Ω are wavevector and frequency of phonons. These atomic vibrations affect the polarizability of the medium. Hence, $\tilde{\chi}$ is expressed as a function of *Q*. It is possible to expand $\tilde{\chi}$ as a Taylor series in *Q* since the amplitude of vibration at room temperature is small:

$$\tilde{\chi}(\boldsymbol{k},\omega,\mathbf{Q}) = \tilde{\chi}_0(\boldsymbol{k},\omega) + \left(\frac{\partial\tilde{\chi}}{\partial\mathbf{Q}}\right)_0 \mathbf{Q}(\boldsymbol{r},\mathrm{t}) \tag{3.10}$$

The first term on the right hand side of Eq. (3.10) denotes the electric susceptibility of the medium with no fluctuations. The second term in Eq. (3.10) represents an oscillation of susceptibility induced by the lattice wave *Q*(***r***,t). Substituting Eqs. (3.6), (3.8)-(3.10) into Eq. (3.7), we can express the polarization of the medium in the presence of atomic vibration as

$$\begin{aligned}\mathbf{P}(\boldsymbol{r},\mathrm{t},\mathbf{Q}) &= \mathbf{P}_0(\boldsymbol{r},\mathrm{t}) + \mathbf{P}_{\mathrm{ind}}(\boldsymbol{r},\mathrm{t},\mathbf{Q}) \\ &= \tilde{\chi}_0(\boldsymbol{k},\omega)\mathbf{E}(\boldsymbol{k},\omega)\cos(\boldsymbol{k}\cdot\boldsymbol{r}-\omega\mathrm{t}) \\ &\quad + \left(\frac{\partial\tilde{\chi}}{\partial\mathbf{Q}}\right)_0 \mathbf{Q}(\boldsymbol{q},\Omega)\cos(\boldsymbol{q}\cdot\boldsymbol{r}-\Omega\mathrm{t})\times\mathbf{E}(\boldsymbol{k},\omega)\cos(\boldsymbol{k}\cdot\boldsymbol{r}-\omega\mathrm{t})\end{aligned} \tag{3.11}$$

The first term on the right hand side of Eq. (3.11) is an expression for polarization

vibrating in phase with the incident radiation. The second term is the induced polarization that can be rewritten as

$$\mathbf{P}_{\text{ind}}(\boldsymbol{r},\mathrm{t},\mathbf{Q}) = \frac{1}{2}\left(\frac{\partial\tilde{\chi}}{\partial\mathbf{Q}}\right)_0 \mathbf{Q}(\boldsymbol{q},\Omega)\mathbf{E}(\boldsymbol{k},\omega) \times\{\cos[(\boldsymbol{k}+\boldsymbol{q})\cdot\boldsymbol{r}-(\omega+\Omega)\mathrm{t}] + \cos[(\boldsymbol{k}-\boldsymbol{q})\cdot\boldsymbol{r}-(\omega-\Omega)\mathrm{t}]\} \qquad (3.12)$$

This shows that the induced polarization consists of a Stokes shifted wave with wavevector $\boldsymbol{k}_s = \boldsymbol{k} - \boldsymbol{q}$ and frequency $\omega_s = \omega - \Omega$ and an anti-Stokes shifted wave with wavevector $\boldsymbol{k}_s = \boldsymbol{k} + \boldsymbol{q}$ and frequency $\omega_s = \omega + \Omega$. These relations for Stokes and anti-Stokes shifted waves show that energy and momentum are conserved in the process. The conservation of energy and momentum can more concisely be written as

$$\left.\begin{aligned}\hbar\omega &= \hbar\omega_s \pm \hbar\Omega \\ \mathrm{k} &= \mathrm{k}_s \pm \mathrm{q}\end{aligned}\right\} \qquad (3.13)$$

where ω_s and k_s represent frequency and momentum of the scattered light respectively. Note that since the momenta of the incident and scattered photons are very small compared to the reciprocal lattice vectors, only excitations with $\boldsymbol{q} \approx 0$ take part in the Raman process. That means the momenta of incident and scattered light ($1/\lambda$ ~ on the order of 10^6 cm^{-1}) is much less than that of phonon ($1/a$ ~ on the order of 10^9 cm^{-1} where a is the lattice constant). Hence only excitations near the zone center, $\boldsymbol{q} \approx 0$, are involved in Raman scattering.

Furthermore, the energy scattered by the induced vibrating electric dipole moment per unit time per unit solid angle can be written as

$$\frac{d W_s}{d\Omega} = \frac{\omega^4}{(4\pi)^2 \varepsilon_o c^3} \left| \boldsymbol{e}_s \cdot \mathbf{p}_{ind} \right|^2 \qquad (3.14)$$

where $d\Omega$ the element of solid angle, ε_o is permittivity of the material, c is the speed of light in the material and $\boldsymbol{e}_s$ is the unit vector in the direction of the polarization of the scattered light. Equation (3.14) shows that the differential cross section of the induced polarization depends on the polarization of scattered and incident light. In other words, the intensity of scattered light depends explicitly on the polarization of the scattered and the incident light. In the next section, we will discuss Raman tensors and the polarization selection rules upon which the intensity of scattered light depends.

3.5 Raman tensors and polarization selection rules

From the previous section, we can infer that the symmetry properties of the second-order susceptibility tensor and the spatial symmetry of the medium involved help determine the scattering cross section for the Raman processes. The Raman tensors and the polarization of incident photons set the selection rules for determining the symmetries of the Raman active phonons.

The intensity of scattered light can be defined as the time-averaged power of the

scattered light. For our purpose of understanding Raman selection rules, one can determine the intensity of Raman scattered light ($\mathbf{I_s}$) by the induced polarization discussed in the previous section. Using Eqs. (3.12) and (3.14), we obtain:

$$\mathbf{I_s} \propto \left| \boldsymbol{e}_i \cdot \Re \cdot \boldsymbol{e}_s \right|^2 \qquad (3.15)$$

where $\Re = \left(\frac{\partial \tilde{\chi}}{\partial Q} \right)_0 \hat{Q}(\Omega)$ and $\hat{Q}(\Omega)$ is a unit vector in the direction of induced electric dipole moment, $\boldsymbol{e}_i$, is along the directions of polarization of the incident light. The Raman tensor, $\Re$, is a second-rank tensor like the polarizability tensor which contains the polarizability as a function of symmetry.

Equation (3.15) demonstrates that the intensity of Raman scattering light is dependent on the directions of polarizations of both the incident ($\boldsymbol{e}_i$) and scattered ($\boldsymbol{e}_s$) light, as well as the Raman tensor ($\Re$).

3.5.1 Raman Tensors for Zinc-blend-type Structures

CdTe has a zinc-blende-type structure. The zone-center optical phonon of cubic zinc-blende structures has a space-group symmetry Γ_4 that is a triply degenerate representation with components along **x**, **y** and **z**. These three components can be considered as the projections of the relative displacement of atoms in the unit cell along the crystallographic axes. Thus the third-rank tensor $\left(\frac{\partial \tilde{\chi}}{\partial Q} \right)$ that depends on phonon

displacement has only one linearly independent nonzero component. The corresponding Raman tensors for optical phonons polarized along the **x**, **y** and **z** directions, which are dependent on the phonon displacement, are given as 3 x 3 matrices:[51]

$$\Re(\mathbf{x}) = \begin{pmatrix} 0 & 0 & 0 \\ 0 & 0 & d \\ 0 & d & 0 \end{pmatrix}$$
$$\Re(\mathbf{y}) = \begin{pmatrix} 0 & 0 & d \\ 0 & 0 & 0 \\ d & 0 & 0 \end{pmatrix} \qquad (3.16)$$
$$\Re(\mathbf{z}) = \begin{pmatrix} 0 & d & 0 \\ d & 0 & 0 \\ 0 & 0 & 0 \end{pmatrix}$$

The Raman polarizability d is directly proportional to the amplitude probability corresponding to scattering of photons with the emission of an optical phonon. The intensity of Raman scattered light is proportional to the square of *d* as can be seen in Eq. 3.15. Equation 3.16 suggests that the nonzero components of the Raman tensor $\Re(\mathbf{x})$ of an optical phonon polarized along **x** direction are $\Re_{yz}(\mathbf{x})$ and $\Re_{zy}(\mathbf{x})$. Similar arguments hold true for the remaining two Raman tensors for an optical phonon polarization along **y** and **z** directions. We can now see that the Raman selection rules depend on the geometry of the sample. The selection rule can be more concisely written in the Porto notation as $\mathbf{k}_i(\mathbf{e}_i, \mathbf{e}_s)\mathbf{k}_s$. Here $\mathbf{k}_i$ and $\mathbf{k}_s$ represent the direction of the incident and scattered light respectively. And $\mathbf{e}_i$ and $\mathbf{e}_s$ specify the direction of polarization of the incident and scattered light, respectively. For the backscattering

geometry (our case), $\mathbf{k}_i$ and $\mathbf{k}_s$ point in opposite directions. The direction of wavevector ***q*** of the phonons must be along $\mathbf{k}_i$ or $\mathbf{k}_s$ so that momentum is conserved. Let **x**, ***y*** and **z** be along the directions [100], [010] and [001] and **y**' and **z**' along [011] and $[0\,\bar{1}\,1]$ directions, respectively.

Consider light incident on a sample in the growth direction along [100]. For backscattering, ***q*** must be along $[\bar{1}\,00]$ and thus its Raman tensor is given by $\Re(\mathbf{x})$ of Eq. (3.16). Thus for LO phonon polarized along *x* in the backscattering geometry, there are four possible configurations for linearly polarized light that are nonzero implying that the corresponding backscattered Raman intensities are nonzero.

$$\mathbf{x}(\mathbf{y},\mathbf{z})\overline{\mathbf{x}} = \mathbf{y}\cdot\Re(\mathbf{x})\cdot\mathbf{z} = \begin{bmatrix}0 & 1 & 0\end{bmatrix}\begin{pmatrix}0 & 0 & 0\\ 0 & 0 & \mathsf{d}\\ 0 & \mathsf{d} & 0\end{pmatrix}\begin{pmatrix}0\\ 0\\ 1\end{pmatrix} = \mathsf{d}$$

$$\mathbf{x}(\mathbf{z},\mathbf{y})\overline{\mathbf{x}} = \mathbf{z}\cdot\Re(\mathbf{x})\cdot\mathbf{y} = \begin{bmatrix}0 & 0 & 1\end{bmatrix}\begin{pmatrix}0 & 0 & 0\\ 0 & 0 & \mathsf{d}\\ 0 & \mathsf{d} & 0\end{pmatrix}\begin{pmatrix}0\\ 1\\ 0\end{pmatrix} = \mathsf{d}$$

$$\mathbf{x}(\mathbf{y}',\mathbf{y}')\overline{\mathbf{x}} = \mathbf{y}'\cdot\Re(\mathbf{x})\cdot\mathbf{y}' = \begin{bmatrix}0 & 1 & 1\end{bmatrix}\begin{pmatrix}0 & 0 & 0\\ 0 & 0 & \mathsf{d}\\ 0 & \mathsf{d} & 0\end{pmatrix}\begin{pmatrix}0\\ 1\\ 1\end{pmatrix} = 2\mathsf{d} \qquad (3.17)$$

$$\mathbf{x}(\mathbf{z}',\mathbf{z}')\overline{\mathbf{x}} = \mathbf{z}'\cdot\Re(\mathbf{x})\cdot\mathbf{z}' = \begin{bmatrix}0 & -1 & 1\end{bmatrix}\begin{pmatrix}0 & 0 & 0\\ 0 & 0 & \mathsf{d}\\ 0 & \mathsf{d} & 0\end{pmatrix}\begin{pmatrix}0\\ -1\\ 1\end{pmatrix} = -2\mathsf{d}$$

On the other hand, the back-scattering associated with $\mathbf{x}(\mathbf{y},\mathbf{y})\overline{\mathbf{x}}$, $\mathbf{x}(\mathbf{z},\mathbf{z})\overline{\mathbf{x}}$, $\mathbf{x}(\mathbf{y}',\mathbf{y}')\overline{\mathbf{x}}$ and $\mathbf{x}(\mathbf{z}',\mathbf{z}')\overline{\mathbf{x}}$ are zero.

$$\mathbf{x}(\mathbf{y},\mathbf{y})\bar{\mathbf{x}} = \mathbf{y}\cdot\Re(\mathbf{x})\cdot\mathbf{y} = \begin{bmatrix}0 & 1 & 0\end{bmatrix}\begin{pmatrix}0 & 0 & 0\\ 0 & 0 & \mathsf{d}\\ 0 & \mathsf{d} & 0\end{pmatrix}\begin{pmatrix}0\\ 1\\ 0\end{pmatrix} = \mathbf{0}$$

$$\mathbf{x}(\mathbf{z},\mathbf{z})\bar{\mathbf{x}} = \mathbf{z}\cdot\Re(\mathbf{x})\cdot\mathbf{z} = \begin{bmatrix}0 & 0 & 1\end{bmatrix}\begin{pmatrix}0 & 0 & 0\\ 0 & 0 & \mathsf{d}\\ 0 & \mathsf{d} & 0\end{pmatrix}\begin{pmatrix}0\\ 0\\ 1\end{pmatrix} = \mathbf{0}$$

$$\mathbf{x}(\mathbf{y}',\mathbf{z}')\bar{\mathbf{x}} = \mathbf{y}'\cdot\Re(\mathbf{x})\cdot\mathbf{z}' = \begin{bmatrix}0 & 1 & 1\end{bmatrix}\begin{pmatrix}0 & 0 & 0\\ 0 & 0 & \mathsf{d}\\ 0 & \mathsf{d} & 0\end{pmatrix}\begin{pmatrix}0\\ -1\\ 1\end{pmatrix} = \mathbf{0} \qquad (3.18)$$

$$\mathbf{x}(\mathbf{z}',\mathbf{y}')\bar{\mathbf{x}} = \mathbf{z}'\cdot\Re(\mathbf{x})\cdot\mathbf{y}' = \begin{bmatrix}0 & -1 & 1\end{bmatrix}\begin{pmatrix}0 & 0 & 0\\ 0 & 0 & \mathsf{d}\\ 0 & \mathsf{d} & 0\end{pmatrix}\begin{pmatrix}0\\ 1\\ 1\end{pmatrix} = 0$$

The LO mode is forbidden in these geometries and thus the corresponding Raman intensity is zero.

In addition, we can show that the Raman scattering from the TO phonon is not allowed in backscattering geometry from a (100) sample surface. The polarization of TO of the light incident along the **x** direction must be along **y**, or **z** or a linear combination of **y** and **z**. But the Raman tensor of optical phonon polarized along the **y** and **Z** has a projection along **x**. This means that the polarization of the incident and scattered light must have a projection along the backscattering direction. Hence, Raman scattering by the TO phonon is not allowed in backscattering geometry from the (100) surface of CdTe.

3.5.2 Raman Tensors for Wurtzite Structures

The CdS nanowire samples we have investigated have the hexagonal wurtzite structure. The wurtzite structure belongs to the space-group C_{6v}^4 and group theory predicts that the zone-center optical modes are A_1, $2B_1$, E_1 and $2E_2$.[50,67] In the A_1 branch, the Raman active phonon is polarized along the z-direction. The E_1 branch is also Raman active in which the phonon is polarized in the xy plane. The Raman tensors of the wurtzite structures are as follows:

$$\begin{pmatrix} a & 0 & 0 \\ 0 & a & 0 \\ 0 & 0 & a \end{pmatrix} \quad A_1(\mathbf{z}) \text{ mode}$$

$$\begin{pmatrix} 0 & 0 & c \\ 0 & 0 & 0 \\ c & 0 & 0 \end{pmatrix} \quad E_1(\mathbf{x}) \text{ mode} \qquad (3.19)$$

$$\begin{pmatrix} 0 & 0 & 0 \\ 0 & 0 & c \\ 0 & c & 0 \end{pmatrix} \quad E_1(\mathbf{y}) \text{ mode}$$

$$\begin{pmatrix} f & 0 & 0 \\ 0 & -f & 0 \\ 0 & 0 & 0 \end{pmatrix} \quad \begin{pmatrix} 0 & -f & 0 \\ -f & 0 & 0 \\ 0 & 0 & 0 \end{pmatrix} \quad E_2 \text{ mode}$$

Let **x**, ***y*** and **z** be along the directions [100], [010] and [001] respectively. Suppose light propagating in the y-direction is incident on the sample in the back-scattering geometry, then the LO must be polarized along the y-direction to satisfy the conservation of momentum. Similarly, if a light propagating in the x-direction is incident on the sample in back-scattering geometry, then the LO must be polarized along the x-

direction. In our case, we have arranged the wire in such a way that the polarization of the incident laser is along the wire (z-axis). The LO phonon polarized along the z-direction has A_1 symmetry; thus the associated allowed back-scattering geometries are $\mathbf{z}(\mathbf{y},\mathbf{y})\bar{\mathbf{z}}$ and $\mathbf{z}(\mathbf{x},\mathbf{x})\bar{\mathbf{z}}$.

$$\mathbf{z}(\mathbf{y},\mathbf{y})\bar{\mathbf{z}} = \mathbf{y}\cdot A_1(\mathbf{z})\cdot\mathbf{y} = \begin{bmatrix}0 & 1 & 0\end{bmatrix}\begin{pmatrix}a & 0 & 0\\ 0 & a & 0\\ 0 & 0 & a\end{pmatrix}\begin{pmatrix}0\\1\\0\end{pmatrix} = a$$

$$\mathbf{z}(\mathbf{x},\mathbf{x})\bar{\mathbf{z}} = \mathbf{x}\cdot A_1(\mathbf{z})\cdot\mathbf{x} = \begin{bmatrix}1 & 0 & 0\end{bmatrix}\begin{pmatrix}a & 0 & 0\\ 0 & a & 0\\ 0 & 0 & a\end{pmatrix}\begin{pmatrix}1\\0\\0\end{pmatrix} = a \qquad (3.20)$$

According to Eqs. (3.15) and (3.20), the intensity of the Raman scattering will be proportional to the square of the Raman polarizability, a.

3.6 Resonant Raman Scattering

The intensity of Raman scattered light also depends on several factors such as the excitation power density, the polarization direction and the excitation wavelength (energy) of the incident light. When the energy of either the *incident* or the *scattered* photon matches the energy of an electronic state of the material, the Raman scattering cross-section (and therefore the intensity of Raman signal) is significantly enhanced. Intensity enhancements on the order of 10^2-10^4 can be achieved.[65] This resonance enhancement (resonant Raman scattering, RRS) is a powerful tool for studying the

electronic band structure, in addition to studying the vibrational modes of a material. It has been successfully used to study electronic states in semiconductors, superconductors, amorphous materials, as well as in various nanostructures.[23,68]

The application of RRS to the study of nanoscale materials is of particular importance, since the significant enhancement of the intensity of scattered light permits studying *individual* nanostructures (such as carbon nanotubes[69] and nanowires[70]), whereas conventional Raman scattering is usually limited to the ensemble measurements.

In a microscopic quantum mechanical picture, one-phonon Raman scattering can be described within the framework of the time-dependent perturbation theory. The scattering efficiency is calculated by third-order perturbation theory in which the Raman scattering is represented by a three-step process.[71,72] In the first step, the incident laser photon is absorbed and excites the crystal from the ground to the excited state by creating an electron-hole pair. Then the electron-hole pair is scattered with the creation or annihilation of a phonon. Finally, the electron-hole pair recombines by emitting a photon. The dominant contribution to the scattering efficiency near resonant conditions is given by[69,73,74]

$$\left(\frac{2\pi}{\hbar}\right)\sum_{n,n'}\left|\frac{\langle 0|H_{eR}(\omega_i)|a\rangle\langle a|H_{e\text{-}ion}|a\rangle\langle a|H_{eR}(\omega_i)|0\rangle}{[E_a-\hbar\omega_i-i\Gamma_a][E_a-\hbar\omega_s-i\Gamma_a]}\right|^2 \qquad (3.21)$$

where $H_{eR}(\omega_i)$ and $H_{e\text{-}ion}(\omega_i)$ is Hamiltonian of the exciton-radiation and exciton-phonon interaction, respectively. A ground state $|0\rangle$ and the excited state $|a\rangle$ with energy E_a are taken as the initial and intermediate states, and $\hbar\omega_i$ and $\hbar\omega_s$ are the energies of the incident and Raman scattered photons, respectively. Γ_a is the damping constant (lifetime broadening) that depends on the finite lifetime of the states τ_a as $\Gamma_a = \hbar/\tau_a$. We should point out that while the Raman scattering of photons is mediated by the electronic interactions, the electronic system returns to the initial state.

As can be seen from Eq. 3.21, the Raman scattering can be greatly enhanced when either the energy of the incident or the scattered photon matches the energy of the particular electron-hole pair (excitonic) state. The first condition, $E_a = \hbar\omega_i$, is known as an incoming resonance, whereas the second case $E_a = \hbar\omega_s$ is called an outgoing resonance. We can achieve resonant Raman scattering conditions by tuning the laser energy to game the energy of the electronic states in the material. Moreover, the resonances with the states that are not optically active may be observed since the RRS scattering can be with virtual states. Hence, measuring Raman scattering intensity as a function of the excitation energy provides detailed information about the electronic band structure of the material.

In summary, we have presented a theory of crystal vibrations in a diatomic basis in the first order harmonic approximation of the interaction between atoms. Based on this, we have obtained the phonon dispersion curves and discussed the optical and

acoustic phonons that will be useful to have in mind. We have also presented the theory of inelastic light scattering by phonons (Raman scattering), discussed Raman selection rules, and finally we have discussed the theory of resonant Raman scattering. These comments will help us in discussing our results and analysis later in this thesis.

4 Samples and Experimental Techniques

In this chapter, a description of the samples studied for this dissertation, as well as the discussion of the experimental techniques employed will be presented. The first section contains a discussion of CdTe SAQDs, including fabrication methods and sample descriptions. In the second section, the CdS nanowires sample's synthesis method and sample descriptions are given. The third section details the experimental setup and includes a discussion of the main experimental instruments.

4.1 CdTe SAQD Samples

The CdTe self-assembled quantum dot samples investigated in this thesis were provided by J. Kossut's and G. Karczewski's group at the Institute of Physics, Polish Academy of Sciences, Warsaw, Poland. The samples were fabricated by molecular beam epitaxy (MBE) that has been successfully demonstrated to make well-controlled size and spatial distribution of SAQDs on a large area of substrate.[75,76,77] In the MBE technique, a molecular beam of each constituent element is created in separate ovens in an ultra-high vacuum chamber. The beams are then guided to strike a substrate which was maintained at temperature of 320 °C. The system is equipped with a shutter in front of each source to regulate the flow of the beams. The opening and closing intervals of the shutters can be controlled on the timescale of monolayer growth. This provides a precise method of controlling the growth of materials onto a substrate so they form a single crystal. The growth process was monitored by reflection high energy

electron diffraction (RHEED). A schematic of the sample is shown in Fig. 4.1. The growth direction is indicated by the arrow pointing to Z.

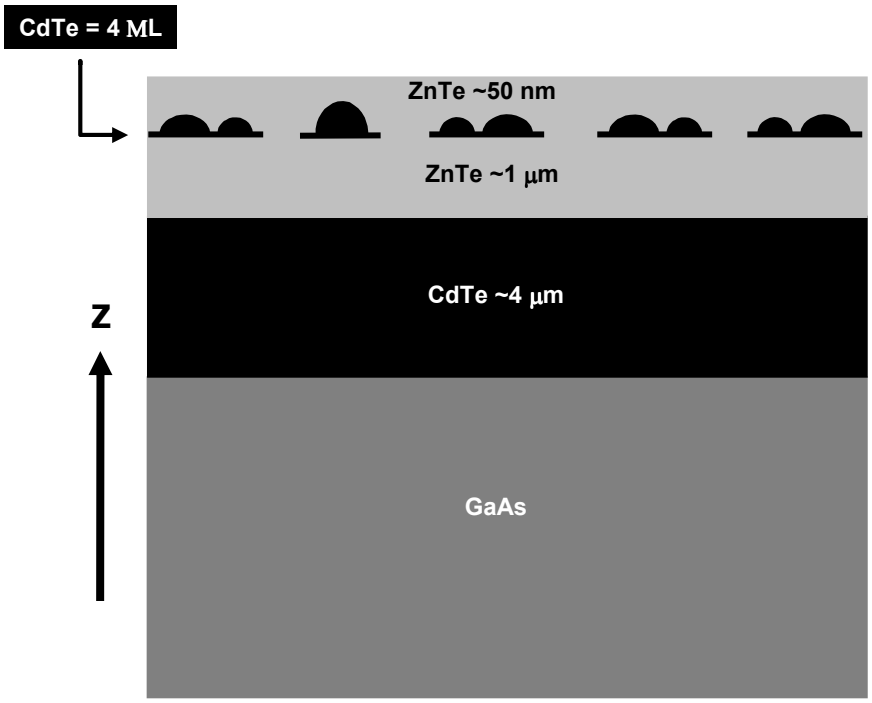

Figure 4.1: Schematic of the CdTe quantum dot sample growth.

The growth process and the QD formation mechanism are as follows. Initially, 4 μm thick CdTe layers are grown on a (100)-oriented 1mm thick GaAs substrate. After that, a 1 μm thick ZnTe buffer layer is grown on top of the CdTe. The purpose of the 4 μm thick layer of CdTe sandwiched between GaAs and ZnTe is to relax the strain due to lattice mismatch between GaAs and ZnTe which is 7.4%. The lattice mismatch between CdTe and ZnTe is somewhat less, at 5.9%. Subsequently, the SAQDs are fabricated by depositing a thin CdTe quantum dot layer (4 monolayer (ML)) on the ZnTe layer. A slow growth rate of 0.025 monolayer/second is preferred to achieve equilibrium

conditions and to easily monitor the process with the RHEED.[75] After depositing the QDs layer, the Cd flux was interrupted for 20 seconds to facilitate a uniform deposition of quantum dots. An atomic force microscope (AFM) image of the surface of the QDs sample after the deposition of 3.5-ML-thick CdTe is shown in Fig. 4.2. Finally, the process is completed by capping the dots with a 50 nm thick ZnTe layer. The capping layer protects the QDs from the atmosphere and prevents oxidation.[78]

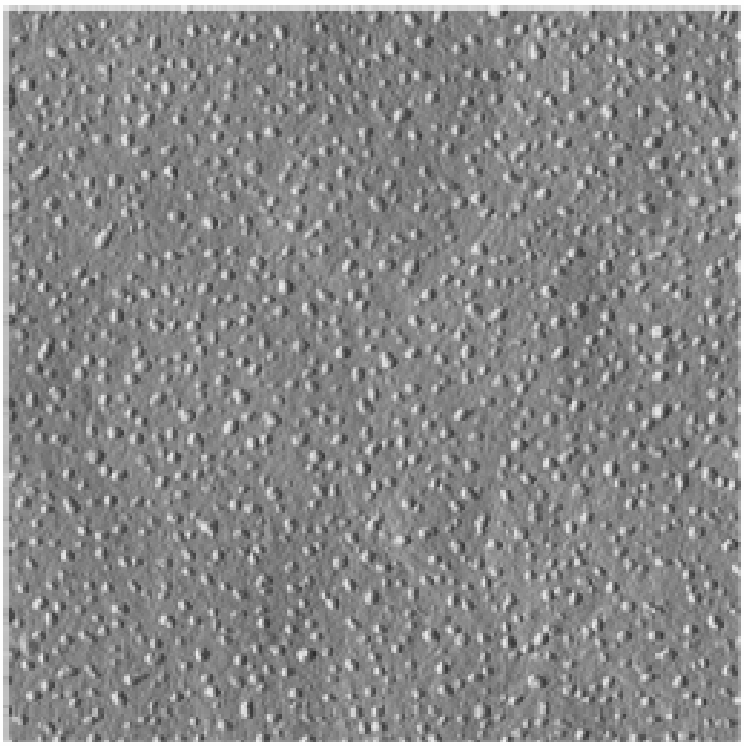

Figure 4.2: AFM top view of the surface on which 3.5-ML-thick CdTe was deposited. The scanned size is 1X1 μm. The typical size of the small islands was ~20 nm in diameter and ~2.7 nm in height.[79]

The lattice constants of GaAs, ZnTe and CdTe are 5.65, 6.10 and 6.48 Å respectively. A strain due to the lattice mismatch between ZnTe buffer layer and CdTe quantum dots layer develops as the quantum dot layer is deposited. The quantum dot layer forms small islands at a thickness of 4 ML of CdTe. A cross-section transmission electron microscope image taken by G. Karczewski's group, not shown here, confirmed the formation of thin islands of CdTe layer covered by quantum dots.[1,79] These quantum dots on top of tiny islands, formed as a result of strain due to lattice mismatch, are called self-assembled quantum dots (SAQDs). The QDs' average diameter and surface density are approximately 3 nm and 10^{12} cm^{-2}, respectively. Part of the as-grown sample was annealed in an inert Ar atmosphere at 420 °C for 15 seconds. We investigated how annealing affects the characteristics of the CdTe SAQDs.

4.2 CdS nanowires

The CdS nanowires (NW) used for this study were supplied by Professor L. J. Lauhon's group (Department of Materials Science and Engineering, Northwestern University, IL). The CdS nanowires are grown on a Si(100) substrate using a chemical vapor deposition and gold-catalyzed vapor-liquid-solid (VLS) growth. For the VLS growth, it is important that the catalyst metal forms a liquid alloy with the nanowire material and also that this liquid alloy concurrently exist with the solid nanowire material. An equilibrium phase diagram can be used to select the right catalyst metal, to determine a composition of the catalyst and nanowire material, and to find out the synthesis temperature to achieve the above conditions.[80]

A schematic of the VLS growth is presented in Fig. 4.3. The catalyst is used to govern the growth direction in 1D. In addition, the size of the gold catalyst particles determines the diameter of the nanowires. [80,81] The VLS process starts with the formation of a nanosized liquid droplet of a gold catalyst. Then it follows with the dissolution of gaseous CdS reactants into the nanosized gold catalyst liquid droplets to form Au-CdS liquid alloys as the temperature is increased above the eutectic point. The eutectic point is the point in binary phase diagram at which all three phases (i.e., vapor, liquid and solid) exist simultaneously. The nanowires start to grow at the liquid-solid interface when the liquid alloys get saturated in the presence of CdS reactant as long as the gold catalyst remains liquid.[82]

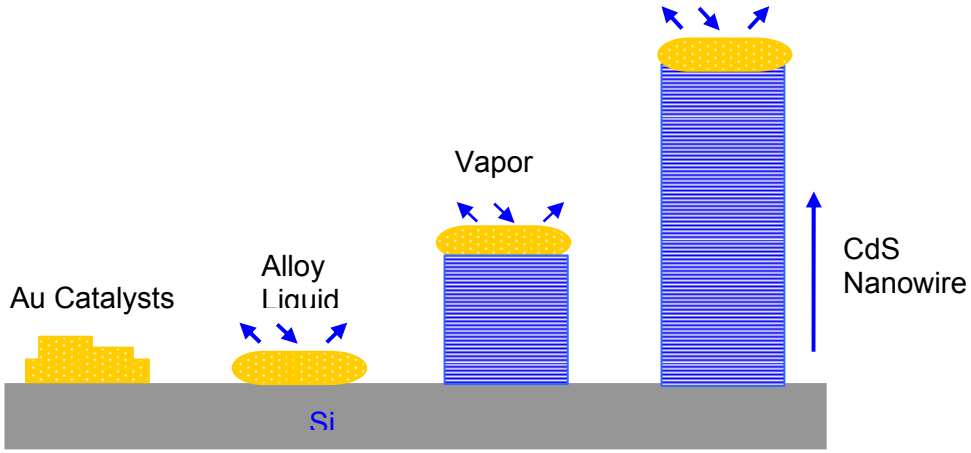

Figure 4.3: Schematic representation of the VLS growth.[83]

We have studied both single wire samples and a sample containing an ensemble of nanowires. The average diameter and length of the single CdS nanowires is 50 nm and 10 μm, respectively. The average diameter and length of the ensemble of NWs is 10 nm and 10 μm, respectively. Fig. 4.4 displays a scanning electron microscope

(SEM) image of the ensemble CdS nanowires (NWs) sample. The SEM image indicates that the density, the length and the shapes of the NWs are not uniform. Some bends, kinks, branches and bulges are observed on the image. However, some long (~10 μm) relatively straight strands can be seen on the other SEM image. The SEM also displays the nonuniformity of the distribution of the nanowire samples on the substrate surface.

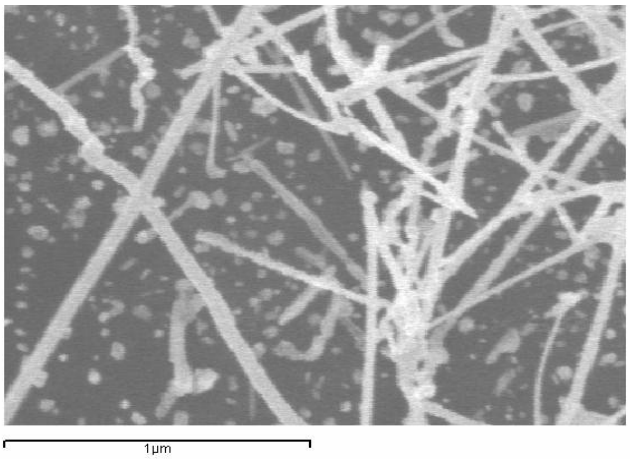

Figure 4.4: SEM image of bulk CdS nanowire sample grown on Si(100). The image scale is 1 μm.[81]

4.3 Experimental setup for Resonant Raman Scattering

In this section, the experimental setup used for resonant Raman scattering (RRS) measurement and the major experimental apparatus involved will be described. The RRS spectra from the QDs and nanowires are recorded in two different experimental configurations. In both cases, Raman spectra were obtained in the back-

scattering geometry. A 50X/0.5NA objective was used to achieve a ~1.5 μm exciting laser spot size and to collect the back-scattered resonant Raman signal. Resonant Raman spectra were collected using a DILOR triple spectrometer running in subtractive mode with a liquid nitrogen cooled charge-coupled device camera. The resonant Raman intensities, from which backgrounds are subtracted, were normalized to the laser power and the acquisition time.

4.3.1 Experimental Configuration for CdTe SAQD experiments

Figure 4.5 displays the typical experimental setup used in our lab. Only the major components of the system are included here. As described later in this section, the direction of polarization of incident and back-scattered light is controlled with a combination of Glan-Thompson polarizer and a Babinet-Soleil compensator. The directions of the incident and back-scattered laser light are indicated by arrows.

All the CdTe SAQD data were taken using this arrangement with an external microscope objective. The temperature dependent PL was measured with the sample in a cryostat that was cooled by liquid He. The RRS measurements were done at room temperature by mounting the CdTe quantum dot sample on the outside of the cryostat. The 514.5 nm line from an Argon ion laser is used to excite the sample for the temperature dependent PL measurements. The excitation sources for the resonant Raman measurements were Rhodamine-6G and DCM tunable dye lasers pumped by a multi-line cw Ar^+ laser. The Rhodamine-6G dye laser was tuned from 575 nm to 605 nm. The DCM dye laser was tuned from 610 nm to 710 nm.

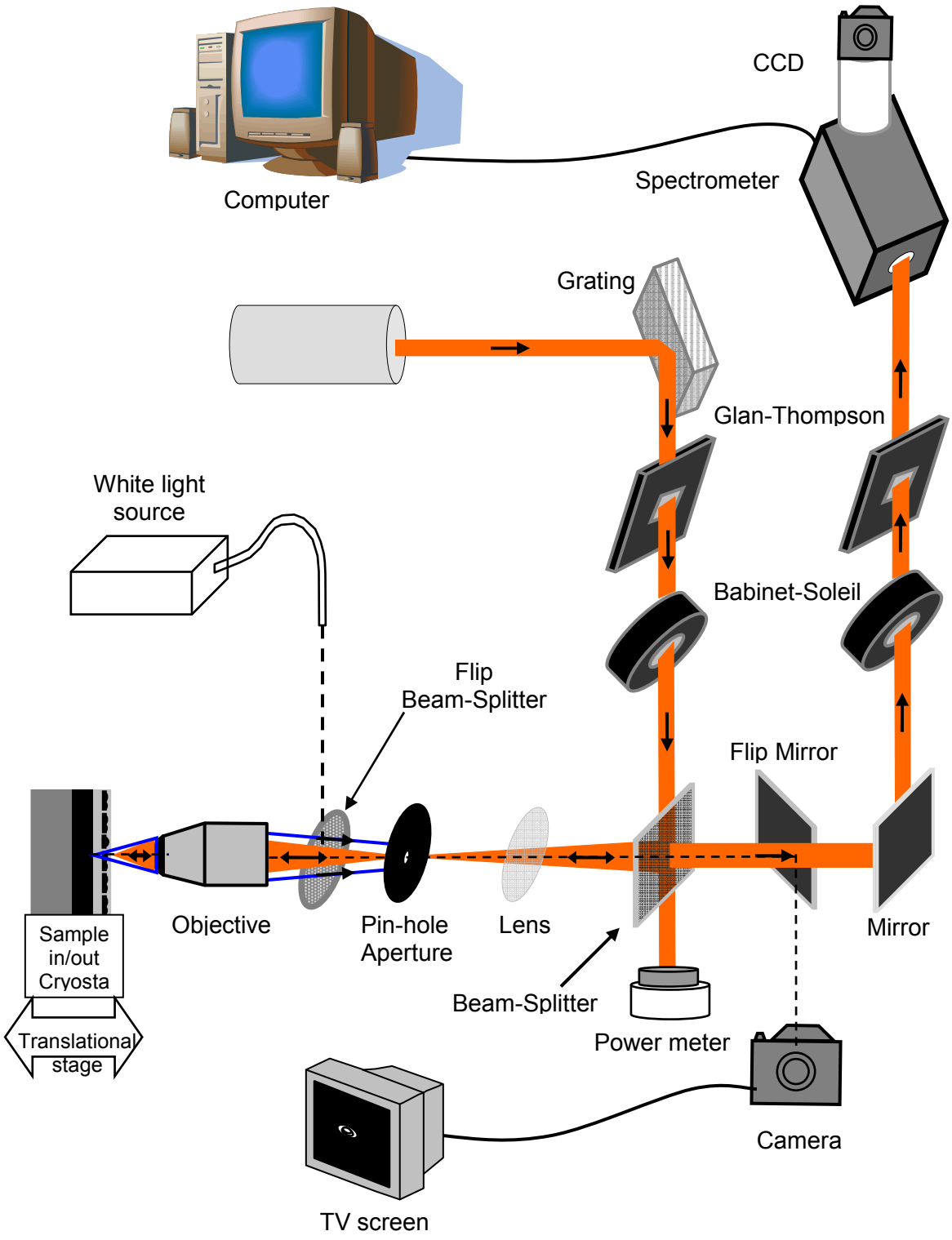

Figure 4.5: Experimental setups for taking PL and RRS from CdTe SAQDs

A grating coupled with a galvanometer made it possible to disperse the dye laser to get approximately a single wavelength. The Glan-Thompson polarizer located after the dye laser is arranged in such a way only vertically polarized light is allowed to pass. The Babinet-Soleil next to the Glan-Thompson is used to rotate the polarization direction of the incident laser. The beam-splitter is positioned at approximately 45 ^{o} angle with respect to the laser beam so that half of the beam reflects toward the sample. The remaining half of the beam, which passes through the beam-splitter, is measured by a power meter to monitor the power of the laser exciting the sample. Then the 8 mm convex lens focuses the laser at the center of the pin-hole. The pin-hole aperture in this confocal arrangement is essential for eliminating stray back-scattered light from the out-of-focus region of the sample. Finally, the laser beam is focused on the sample with a 50X microscope objective. The objective collects the back-scattered light and focuses it on the pin-hole. The translational stage positions the sample approximately in the focus of the laser which is determined by monitoring with a camera. The camera also helps to check the alignment of the system. A white light source is used for monitoring and the alignment check (dashed line in Fig. 4.5). During signal collection, the efficiency of the spectrometer depends on the direction of polarization of the light.[84] The maximum efficiency is achieved when the light is vertically polarized with respect to the optical table, and therefore polarized parallel with respect to the spectrometer grating. Thus, the Babinet-Soleil in the path of the scattered light is used to rotate the polarization of the scattered light vertically. The Glan-Thompson polarizer in path of the backscattered light is arranged such that vertically polarized light passes through to the spectrometer entrance slit. The emission

from the sample ranging from 575 nm to 710 nm was spectrally filtered to remove spontaneous fluorescence using a servo-controlled spectrograph. [84]

4.3.2 Experimental Configuration for CdS nanowire experiments

The second experiment makes use of an in-line microscope configuration and is shown by schematic of Fig. 4.6. This configuration is used for measurements of room temperature PL and RRS intensities from the CdS nanowire samples. The RRS and the non-resonant PL spectra from the CdS nanowire were excited using individual lines from a cw Ar^+ laser (458 nm, 476 nm, 488 nm, 496 nm, 502 nm and 514 nm). To protect the sample from laser induced oxidation that might irreversibly damage the wire, when the sample was exposed to air, dry nitrogen gas was continuously blown across the surface of the sample during the entire experiment. The power of the laser through the 50X objective is also kept less than 1 mW to eliminate any possible heating effects in the nanowires. The power density of the tightly focused laser (diameter of about 1.7 μm) of ~1 mW power is very small (about 2 μWatt/cm^2). Even though reducing the optical power of the excitation source reduces the overall strength of a signal, the RRS spectra excited using about 1 mW laser power was strong enough to study electronic and vibronic states in the nanowires.

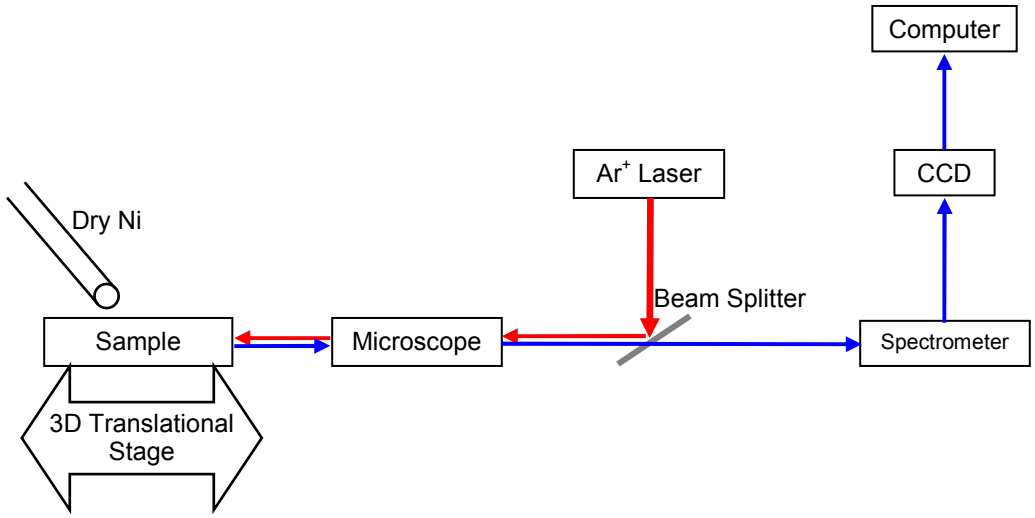

Figure 4.6: Schematic of an in-line Microscope setup.

With this arrangement, it is possible to study a sample as small as 2 μm. We were able to acquire RRS along the 10 μm long CdS nanowire by scanning the sample under the microscope objective with the translational stage. Even with the low excitation power, this experimental arrangement enabled us to collect considerably more signal compared to the lower signal obtained using the experimental arrangement presented in the previous section. This is due to the difference in the alignment, particularly the total number of optical components involved. The smaller number of optical components involved reduces the signal loss due to reflection and scattering.

4.3.3 Spectrometer Calibration and Background Correction

We calibrated the spectrometer regularly by measuring the 514.5 nm line of an Argon laser and placing it at the center of a 20 nm detection range. When the 514.5 nm line was measured at a different position from the center of the detection range, the

measured value slightly deviated from the 514.5 nm. This deviation was observed to increase with increasing distance from the center of the detection range. The inaccuracy in the wavelength measurement is a direct consequence of the calibration accuracy of the spectrometer which depends on factors such as mechanical effect, reading of the spectrograph absolute wave number, resetting of relative frequencies counter, and entrance of an accurate exciting line. Therefore, both the laser and detection wavelength ranges were carefully calibrated using multiple gas lines that were taken under the same conditions as the RRS of the CdTe SAQDs. A reference calibration was also provided by the Raman scattering from the underlying line from Si substrate that was present in all the RRS spectra of the CdS nanowires.

The RRS spectra from the CdTe SAQDs and CdS nanowires that were excited using 587 nm and 487 nm respectively are shown in Fig. 4.7 a & b. To calculate the integrated RRS intensity more accurately, we have subtracted the underlining PL and dark signals from both the CdTe SAQDs and CdS nanowire spectra. The 1LO integrated intensity from CdTe SAQDs was obtained after subtracting the background which was approximated by an inclined straight line as shown in Fig. 4.7a. The RRS signal from CdS nanowire (top spectrum in Fig. 6b) is shifted upward for clarity. The PL background of the RRS of CdS nanowire was estimated by deleting the LO signals and then fitting the resulting lineshape (the middle lines in Fig. 4.7b). After subtracting the PL background the spectrum shown by the bottom line in Fig. 6b is obtained and then the 1LO and 2LO integrated intensities from CdS nanowire samples were calculated. Finally, for both CdTe SAQDs and CdS nanowires, the Raman intensity was normalized to the laser power and accumulation time.

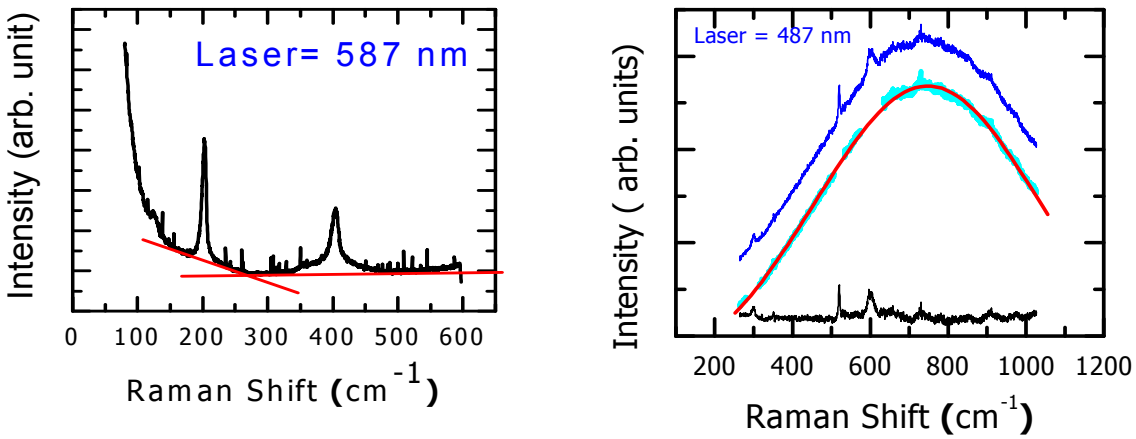

a) b)

Figure 4.7: Typical RRS spectrum from a) CdTe SAQDs b) CdS nanowires. The curves used for the back-ground subtraction is shown in both cases.

4.3.4 The Argon-ion Laser

A Model # 2030, Spectra-Physics Argon Ion Laser was used as a source of excitation for CdTe QDs and CdS nanowire PL, and CdS nanowire RRS measurements. In addition, it served as an optical pump for a dye laser used as a source of excitation for CdTe QDs RRS measurements.

The argon ion laser can potentially lase at 9 different wavelengths. A single line can be preferentially tuned using a prism in front of end mirror. The primary lines are 488 and 514.5 nm. We could also tune to 457.9, 476.5, 496 and 502 nm lines. At each wavelength, the vertical and horizontal fine adjustments of the rear reflector are optimized for maximum output power as indicated on the power meter. The argon was set to lase with all lines for pumping the dye laser.

4.3.5 Dye Laser

In order to perform RRS measurement, one has to be able to continuously vary the excitation wavelength close to the bandgap of the material. In particular, dye lasers are suitable for this purpose as they can be continuously tuned through a wide range of wavelengths. The gain medium in a dye laser is an organic dye molecule that is dissolved in a solvent and circulated through a jet. The organic dye molecules have broad fluorescence bands when excited. To excite the RRS from CdTe quantum dots, we have used Model 599 Standing Wave Dye Laser by Coherent, Inc. Fig. 4.8 below is the schematic of the optics of the Coherent model 599 standing wave dye laser.

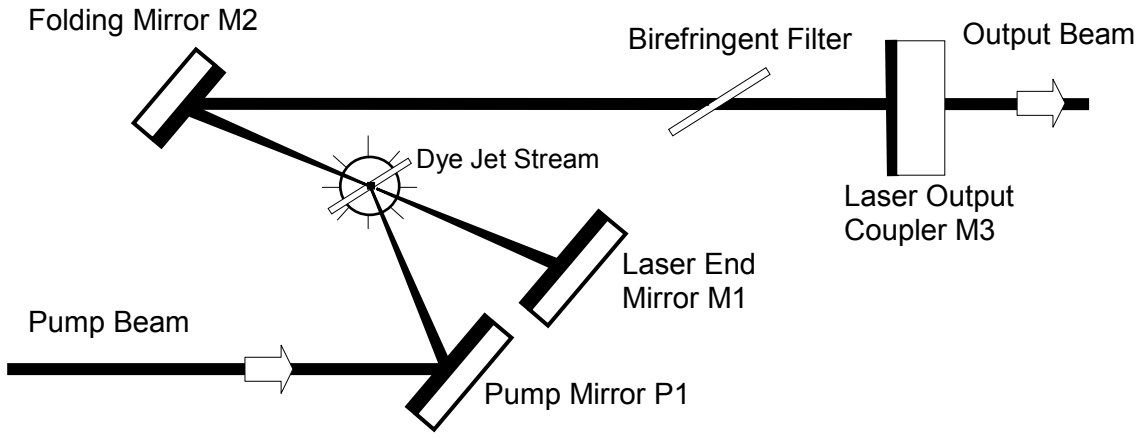

Figure 4.8: Optical schematic of the coherent Model 599 standing wave dye laser.

In all experiments, the pump laser was the argon ion laser running multi-line. The active gain mediums were either Rhodamine 6G or DCM dyes dissolved in ethylene glycol. These dyes can potentially lase from 570 to 640 nm and from 610 to

710 nm respectively. The dyes are prepared according to the dye recipes in the manual, so that the absorption is between 80 and 85%. This is important for long dye lifetime and optimum performance. A birefringent filter that consists of 3-crystalline-quartz plates is used to select a particular laser line. The birefringent filter plate is a linear retarder that produces a relative delay between ordinary and extraordinary rays aligned long the fast and slow axes of the crystal. This allows light a source of a single polarization state to interfere with itself. This makes a birefringent filter plate useful for line-narrowing by selectively tuning a desired wavelength and creating reflection losses at other wavelengths. Basically, the birefringent filter is oriented at Brewster's angle in the laser cavity with the optical axis in the plane of the face so that one can tune a linearly polarized single wavelength light by rotating it.

Sensitive alignment of optical components is required to have the dye laser lase and to achieve stable power. The process of switching a dye involves replacing some optical components with the appropriate ones. That means sensitive optical component alignment is also required every time the dye is switched. A complete description of the alignment procedure is found in Appendix A.

4.3.6 Spectrometer

A spectrometer is an instrument that is designed to collect, spectrally disperse and re-image an optical signal in a particular wavelength range. We have used a DILOR triple Raman Spectrometer manufactured by Jobin Yvon, Inc to collect the spectra scattered from CdTe SAQDs and CdS nanowires samples. A schematic of the normal configuration of a DILOR spectrometer is shown in Fig. 4.9. Both the fore-

monochromator and spectrograph in the system are constructed based on the Czerny-Turner arrangements. The fore-monochromator consists of four spherical mirrors of 800 mm focal length and two plane holographic gratings of 1800 grooves/mm with a maximum efficiency at 500 nm and useful dispersion range from 350 to 850 nm in λ. The two plane holographic gratings are used as a pre-filter for the spectrograph. The spectrograph is composed of two spherical mirrors of focal length 600 mm and the same plane holographic grating just described. The DILOR triple Raman Spectrometer can be configured to be used in a single channel or multichannel (additive and subtractive fore-monochromator, and spectrograph) mode. In all experiments we have conducted, the subtractive fore-monochromator mode is used. In this mode, a double subtractive monochromator is used to select a spectral range while a spectrograph is used to disperse the spectrum.

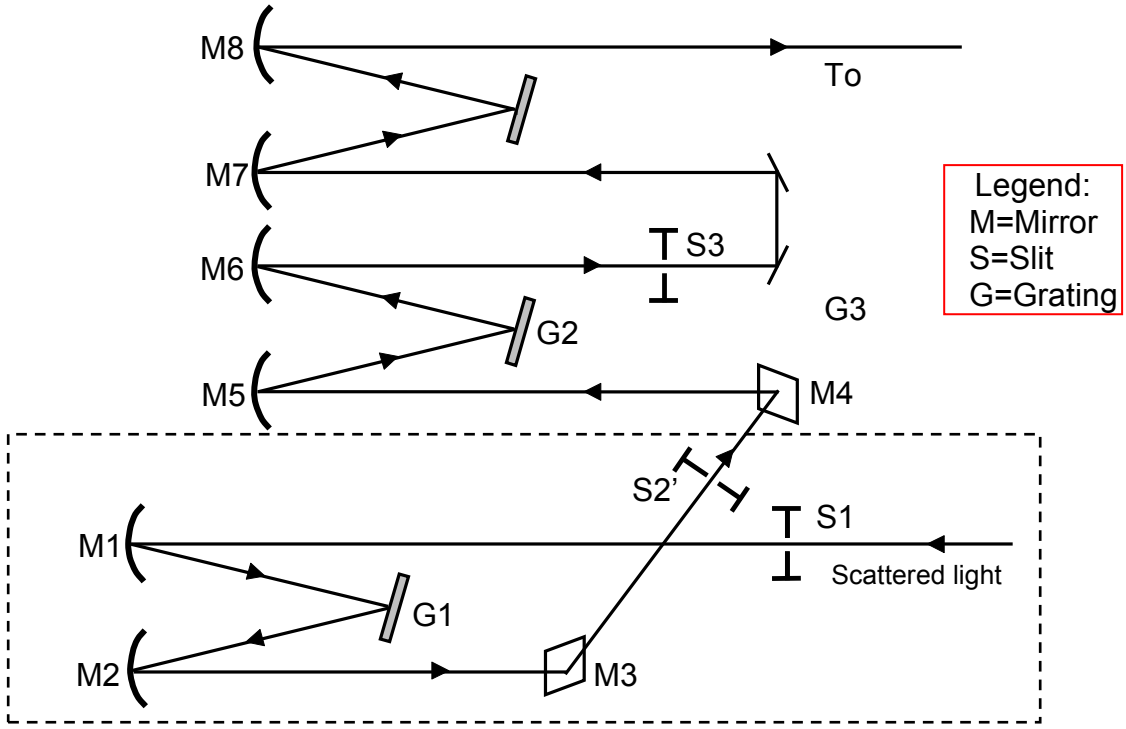

Figure 4.9: Schematic of spectrometer in the normal configuration.[84]

The subtractive fore-monochromator and spectrograph used most frequently in our lab are illustrated in Fig. 4.9. In this configuration, the optical path passes through three slits, S1, S2' and S3. Those slits are electric motor operated and controlled by an encoder. The opening of a horizontal entrance slit (S1) can be regulated from 0 to 2 mm. The slit S2' that determines the half pass band can be varied from 0 to 25 mm. The exit slit, S3, opening is adjustable from 0 to 14 mm.

In the subtractive monochromator mode, normally S1 and S3 are set to the same value. In addition to the resolution, the opening of the S1 and S3 also influence level of

stray light. The level of stray light is reasonable when the slits are less than 150 μm for our experiments with the 514.5 nm excitation line.[84] However a distortion of the background signal may appear when recording a spectrum with high background with narrow slits due to dispersion. A precision alignment, as good as it can be, is not sufficient to attain a condition of no dispersion of the fore-monochromator. A simple solution to overcome this problem is to open the exit slit wider. Opening the exit slit wider will not affect the resolution since in a double subtractive foremonochromatic mode, the second monochromator is the image of the first about the plane of S2'. That means the resolution is basically controlled by S1 when S1 is narrower than S3. For S1=50 μm, the overall spectrometer resolution is 0.2 Å in the subtractive mode.

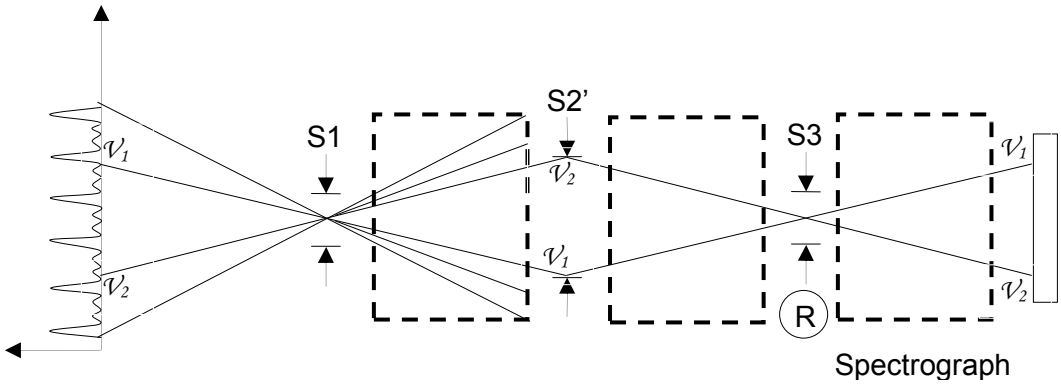

Figure 4.10: Schematic of subtractive fore-monochromator and spectrograph.[84]

The peak position of a spectral line depends on the position of the spectrograph due to calibration accuracy. As previously discussed, we have used Si lines to calibrate CdS nanowires spectra and gas lines to calibrate CdTe/ZnTe quantum dots spectra.

4.3.7 CCD Camera

The spectra dispersed by the spectrograph are collected by a Spectrum One Series liquid nitrogen (LN_2) cooled charge-coupled-device (CCD) camera which was provided by Instruments S.A, Inc. The CCD detector is a two dimensional array of silicon photodiodes (pixels) which has 2000 pixels oriented horizontally and 800 pixels vertically as illustrated in Fig. 4.11.

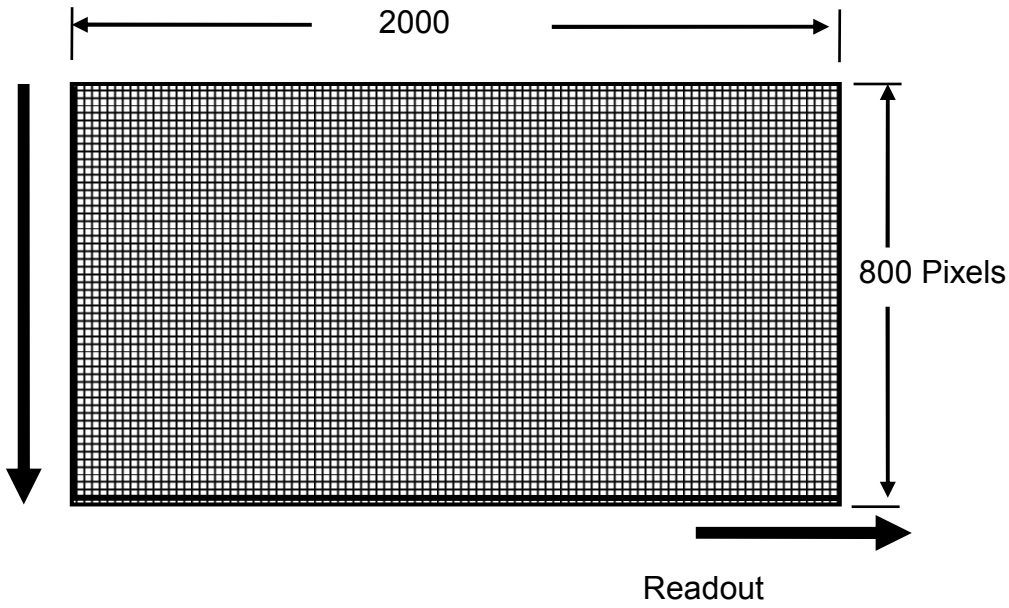

Figure 4.11: CCD camera array. The thick arrows indicate choice of readout by columns or by rows.

The CCD camera is illuminated only when a shutter is opened during data collection. The CCD camera is arranged so that the horizontal axis measures the photon energy and signals coming from different vertical locations along the entrance slit will strike different vertical segments of the array. Thus, 2000 and 800 pixels are

associated with energy and spatial position of the signal respectively. During exposure, the photons generate changes as a result of the photoelectric effect and then each pixel integrates the total charge it experiences. The charges of adjacent pixels are kept separated by a grid of electrodes that confine the charges electrostaticaly. After acquisition, the shutter is closed and then the electrode grid voltages are manipulated by control signals from the detector interface unit. This interface unit successively transports the pixel charges row by row or column by column to the edge of the chip into a readout register.

Optical and spatial optimizations of the spectrometer are employed to achieve an optimum signal to noise ratio. Optical optimization was done by carefully aligning the input optical components. This improves optical coupling from the excitation source to a sample and then from the sample to the spectrograph entrance slit. An increased signal can be gained by extending the integration time, or by increasing the power of the excitation source. However, increasing the source power is not always possible due to heating effects and laser induced oxidation. Another spatial optimization technique is accomplished by collecting the CCD signal which is generated only in the illuminated region of the array (see Fig. 4.12). In this case, collecting from the whole area of the CCD does not increase the collection of the signal, instead it increases the collection of cosmic rays that decreases the overall signal to noise ratio. In all the experiments described here, the Raman signal did not illuminate the total array area of the CCD. To optimize the spectra, first a CCD image was taken and then the active area of the CCD was selectively reduced in such a way to record only the data from the portion of the array where the signal is located.

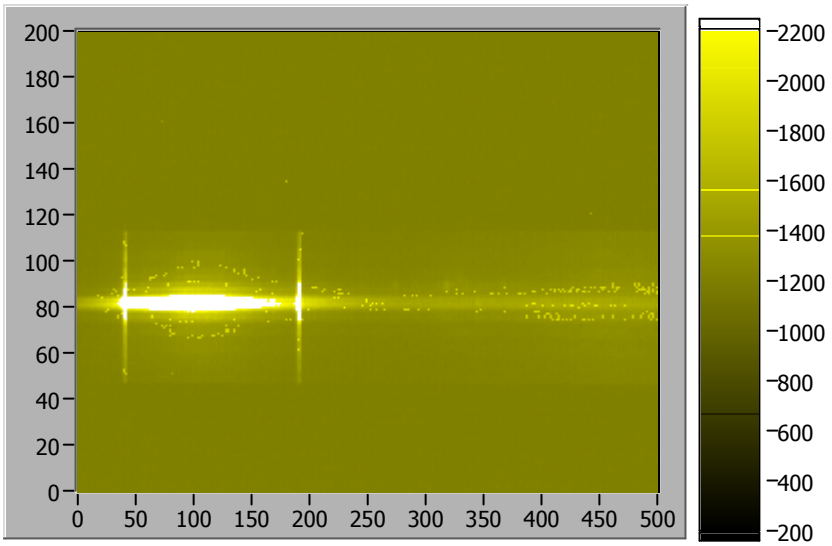

Figure 4.12: CCD image. The thick arrows indicate readout by columns and rows.

It is also important to keep mind in the number of times analog to digital conversion (ADC) occurs to achieve an optimum signal to noise ratio. Some noise is introduced in a signal during each of the ADC. Binning of pixels is advantageous since it combines all signals from the binned pixels into a single ADC. The signal level of binned pixels increases in direct proportional to the number of pixels binned while the shot noise increases only as the square root of the number of pixels. The shot noise is the noise due to the random statistical variations of light that includes both experimental and dark signal components. Hence, a binning of four is used throughout our entire experiment to achieve a better signal to noise ratio by reducing the number of the ADC. On the other hand, increasing the signal integration time also reduces the noise proportionally as long as the time is short enough to avoid saturation.

We have provided a detailed description of the CdTe SAQDs and CdS nanowire samples studied for this thesis as well as the fabrication techniques employed. We have schematically illustrated the experimental setups used to conduct the RRS experiments on boththe CdTe SAQDs and CdS nanowires. In addition, the major experimental components have been discussed in some detail. The typical RRS from both the CdTe SAQDs and CdS nanowires has been shown, and the spectrometer calibration and background correction methods used during data analysis have been discussed.

5 Resonant Raman scattering of CdTe quantum dots

Resonant Raman scattering (RRS) is a sensitive, non-destructive tool which can be used to probe the electronic states of a QD ensemble. In this technique, the intensity of a Raman active phonon mode is monitored as the laser wavelength is scanned through the QDs' electronic states. Because the resonance may be with a *virtual* electronic state, it becomes possible to measure such a state even though the state may not luminesce. Moreover, since the resonance needs only to be local to the quantum dot, we can measure the QD electronic structure even for single layers of self-assembled quantum dots (SAQDs).

The purpose of this chapter is to discuss optical phonons in CdTe/ZnTe SAQDs, to demonstrate resonance behavior in the 1-LO phonon, and to describe the temperature dependent PL measurement. We also measure the energy difference between the excited states (ES) and ground states (GS), to confirm the effect of post-growth annealing on the energy difference, and finally demonstrate the sensitivity of resonant Raman scattering from the edge of the sample in categorizing and measuring layers. The core of the work presented in this chapter has now been published in Abdi et sl., Appl. Phys. Lett. **87**, 183104 (2005).[85]

5.1 Optical phonons in CdTe SAQDs

The resonant Raman scattering data is collected using a back scattering geometry at room temperature. According to the polarization selection rules, only scattering by longitudinal optical phonons is allowed for this configuration. Raman spectra were taken for both the as-grown and the annealed SAQD samples over the entire excitation wavelength range of 570-710 nm in steps of 5 nm. Recall that the CdTe SAQDs are grown on a 1 μm thick layer of ZnTe and are also capped with a 50 nm ZnTe layer. A typical resonant Raman spectrum of the as-grown CdTe QD sample at an excitation wavelength of 590 nm is shown in Fig. 5.1. Gamma rays are removed manually to decrease their interference with the real spectrum. In the RRS cases, we have observed three Raman peaks at energies of ~125 cm^{-1}, 202 cm^{-1} and 404 cm^{-1}.

The peak observed at 125 cm^{-1} has been suggested to originate with the CdTe QDs, but does not correspond exactly to the known CdTe phonon modes.[61] Freire et. al.[86] have observed the bulk CdTe optical phonon peaks at 120.6 cm^{-1}, 139.7 cm^{-1} and 164.3 cm^{-1}. They have suggested that the two low frequency peaks show the presence of distributed Te in the CdTe bulk sample. In addition, they pointed out that the peak at 164.3 cm^{-1} corresponds to a reported bulk CdTe LO phonon mode. However, they have not observed the CdTe phonon peak at 142 cm^{-1}.[87] In our case, the TO phonon peak does not occur in resonant Raman scattering spectra from the CdTe quantum dots, consistent with selection rules that do not allow backscattering from this phonon. We also have not observed the CdTe LO scattering in the resonant Raman scattering

spectra from the CdTe SAQDs sample. That is expected since the CdTe LO peak would be overwhelmed by the strong resonant ZnTe LO peak mainly due to the material involved in the scattering process. The peaks at Raman frequencies of 202 cm^{-1} and 404 cm^{-1} are assigned to the first and second order ZnTe LO-phonon scattering, respectively.

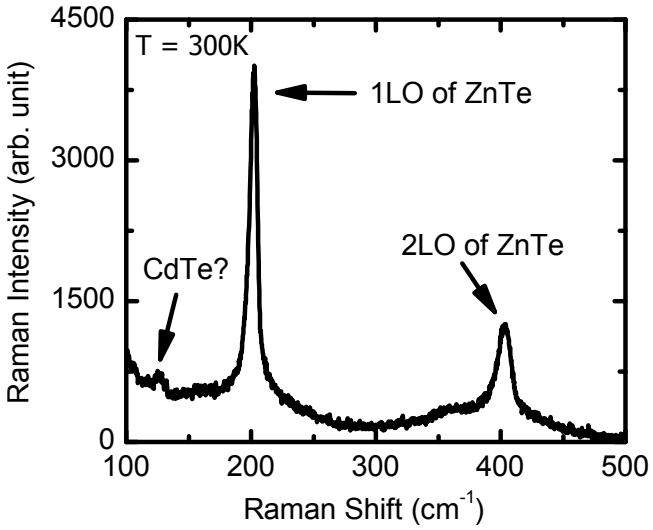

Figure 5.1: Resonant Raman spectrum of the as-grown QD sample excited at a laser wavelength of 590 nm. The two phonon peaks observed at Raman frequencies of 202 cm^{-1} and 404 cm^{-1} are assigned to first and second order scattering of ZnTe LO phonons. The first peak observed at ~ 125 cm^{-1} may be associated with a CdTe phonon mode.

The ZnTe LO phonon scattering exhibited resonance behavior when excited with the laser of energies less than the band gap of bulk ZnTe (2.26 eV). This indicates that the imbedded CdTe quantum dots have an effect on the LO phonon scattering from the ZnTe matrix. This interaction can be explained by the fact that the CdTe exciton

Bohr radius (10 nm) is much larger than the average size of the quantum dots (3 nm).[27] As a result, the CdTe excitons wavefunction extend into the ZnTe matrix. Hence in this study, we use the room temperature RRS sensitivity of the ZnTe longitudinal optical (LO) phonon intensities to probe the ground state-excited state energy (GS-ES) difference in a single layer of CdTe/ZnTe quantum dots. We show that such a non-invasive measurement can be used to probe the change in the GS-ES energy induced by post-growth annealing.

5.2 RRS of ZnTe

In order to isolate the 1-LO phonon signal from the rest of the recorded spectra, the PL background and the dark signal were subtracted from the raw spectra. Figure 5.2 displays a series of first order ZnTe LO phonon Raman spectra for the as-grown QD sample at excitation energies ranging from 2.00 to 2.16 eV. The spectra were also normalized to laser power and acquisition time to quantify the resonance behavior. Note that the Raman spectral intensities strongly depend on excitation energy, with the largest enhancement - of more than two orders of magnitude - occurring at a laser energy of 2.08 eV. Similarly, for the annealed QD sample, the highest Raman intensity is observed at an excitation energy of 2.10 eV (Fig. 5.3). In both cases the room temperature Raman resonance occurs over a ~60 meV range, approximately the same range observed for non-resonant PL for the QD ensemble at low temperatures.[20]

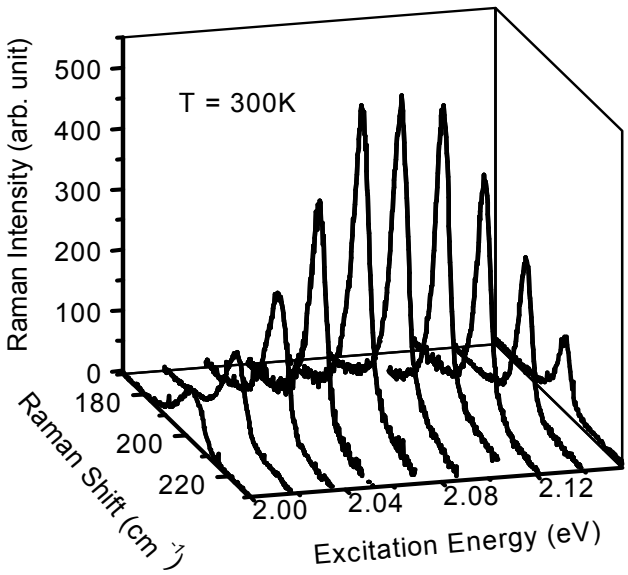

Figure 5.2: Back-scattered Raman spectra of the first order LO phonon peak (centered at 202 cm^{-1}) as a function of excitation energy near resonance for the as-grown CdTe quantum dot sample.

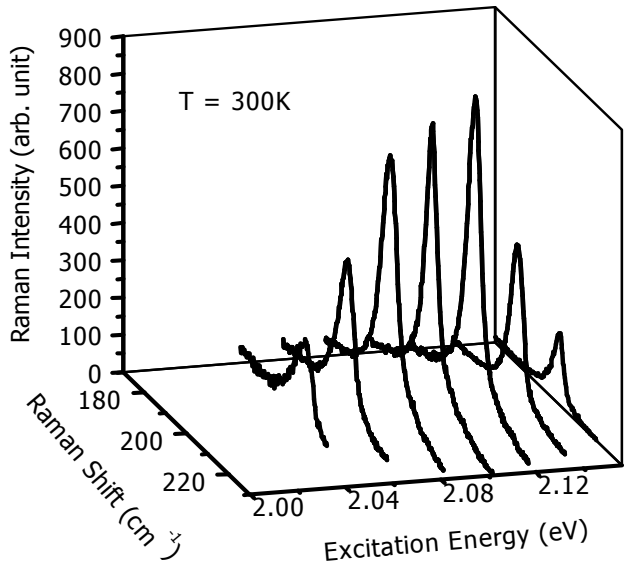

Figure 5.3: Back-scattered Raman spectra of the first order LO phonon peak (centered at 202 cm^{-1}) as a function of excitation energy near resonance for the annealed CdTe quantum dot sample.

Comparing Fig. 5.2 and 5.3, we see that the 1-LO phonon linewidth is narrower after annealing. In addition, we note that the position of resonance peak shifts towards higher energy.

To further investigate the1-LO RRS, we map the total integrated intensity of each 1-LO peak as a function of excitation energy. This provides insight into the phonon-QD interaction.

5.3 Temperature dependent PL

A strong resonance profile of the Raman intensity indicates strong coupling of the LO phonon modes with the QD electronic states. Because excitons randomly populate the quantum dots, the RRS spectra reflect the distribution of ground states for the QD ensemble. Hence, by comparing the ground state PL to the RRS signal, one would expect to find the RRS response to reflect the ground state distribution. However, because at room temperature the luminescence of the CdTe dots is completely quenched, it is not possible to make a direct comparison with the QD ground state energies and the Raman resonance. Moreover, at lower temperatures where the QDs luminesce strongly, it is not possible to measure the Raman scattered signal, as it would be overwhelmed by the PL emission. Because of this, we have performed a careful temperature-dependent measurement of the PL emission for the QD ensemble using 514 nm laser excitation. In Fig. 5.4 a series of PL emission spectra are presented as a function temperature. All of the spectra are normalized and cascaded to clearly display the effect of temperature. Note that the peak of the PL emission spectra shifts to lower energy as the temperature increased.

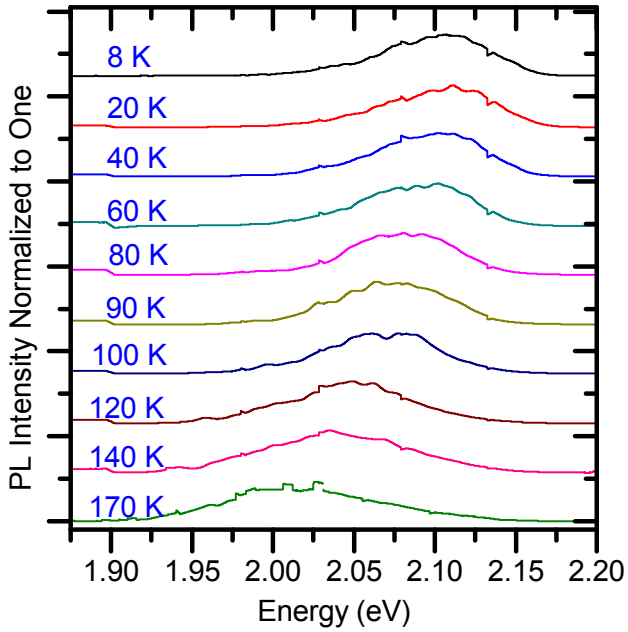

Figure 5.4: Normalized and cascaded PL spectra from the as-grown sample as function of temperature is shown. Note how the peak of PL emission changes with temperature.

In Fig. 5.5 we show the energy positions of the peak PL intensities in the temperature range from 6K to 180K (above 180K the PL is no longer visible). The solid curve is a fit of the data points to the Varshni equation.[24,38] The Varshni equation is given by

$$E_g(T) = E_g(0) - \frac{\alpha T^2}{\beta + T} \quad \cdots\cdots\cdots\cdots (2.13)$$

with $E_g(0)$, α and β as fitting parameters. We obtained a good fit with chi^2 = 9.1785 X 10^{-6}. The curve is extrapolated to room temperature. From the graph, we find the peak PL value at 300 K, and we find that the median energy position of the CdTe QD ground states at room temperature to be 1.96 eV for the as-grown QD sample and 2.02 eV for the annealed QD sample.

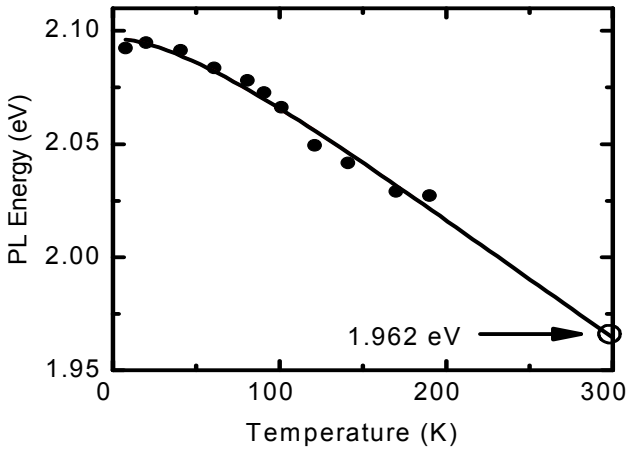

Figure 5.5: Temperature dependence of non-resonant PL peak energy position between 6K and 180K with 514.5 nm laser excitation. The solid line fit indicates the extrapolation to room temperature of the ground state energy of the as-grown CdTe quantum dots.

5.4 Energy difference between excited and ground states

In Fig. 5.6, we compare the integrated RRS intensities (solid points) for the as-grown QD sample with a low-temperature micro-PL spectrum which has been shifted to reflect the effect of temperature (according to Fig. 5.5). The shifted PL spectrum thus represents the room temperature ground state energy distribution of the ensemble for the as-grown QD sample, and the curve through the RRS data points to the right is a Gaussian fit. The similar width of the integrated RRS profile (90 meV) and ground state PL (80 meV) suggests that the Raman scattering is probing the ensemble of quantum dots. However, the integrated RRS signal (solid points) occurs at significantly higher energy (110 meV) than the estimated ground state energy (1.92 eV) of the respective QD sample.[24] These resonances cannot be associated with the ZnTe barrier because

the ZnTe band edge is nearly 300 meV higher in energy than the QD ground states. Taken together, these observations strongly suggest that the integrated RRS intensity reflects coupling to excited state distributions rather than to the ground state distributions. As noted earlier, the exciton Bohr radius is 10 nm while the QDs are ~ 3 nm in diameter. Thus, the fact that it is the ZnTe LO phonon modes which resonates with the QD excited states probably reflects the larger spatial penetration of the QD excited state wavefunctions from these particularly small (~ 3 nm) CdTe dots into the surrounding ZnTe barrier.

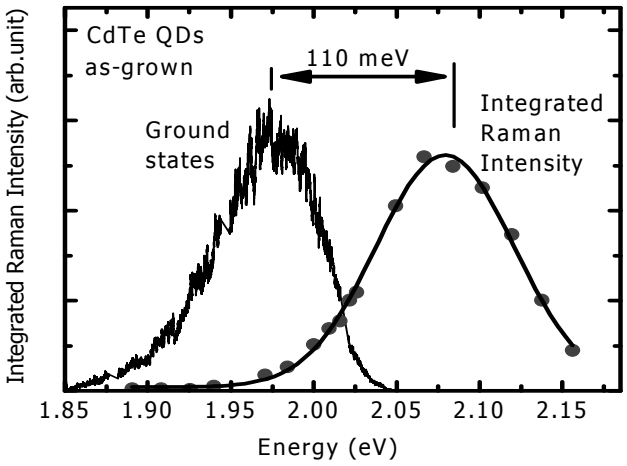

Figure 5.6: Room temperature ground and excited state distributions of the as-grown CdTe QDs. Data points are the integrated RRS intensity of the 1-LO peak for as-grown QD samples as a function of laser energy. Spectra to left are low-temperature micro PL data which have been shifted to account for the temperature shift of the bandgap. The energy differences between the excited states (the integrated Raman intensity data points on the right hand side and their Gaussian fit) and the corresponding ground states (the two shifted PL curves on the left) are 110 meV.

5.5 Effects of Post-Growth Thermal Annealing on QDs

In order to explore the effects of post-growth annealing on the CdTe SAQDs, we made a similar measurement on the annealed sample and graphed the PL with the total integrated intensities of the RRS as a function of laser excitation energy. Figure 5.7 provides a comparison between the results for the annealed and as-grown samples. Note that the PL emission spectrum from annealed sample has moved to higher energy and its distribution is narrower (70 meV compared to 90 meV) than the PL emission spectrum from as-grown sample. From the measurements illustrated in Fig. 5.7, we can estimate the energy separation between ground and excited states in the as-grown and annealed CdTe QDs to be 110 meV and 80 meV, respectively. In order to explain the differing measurements between the two samples, we consider how annealing affects the SAQD sample. Post-growth annealing has been shown to cause interdiffusion of Zn and Cd ions within the QD and its surrounding layers which significantly enlarge the SAQDs, while at the same time makes the confining potential shallower.[88]

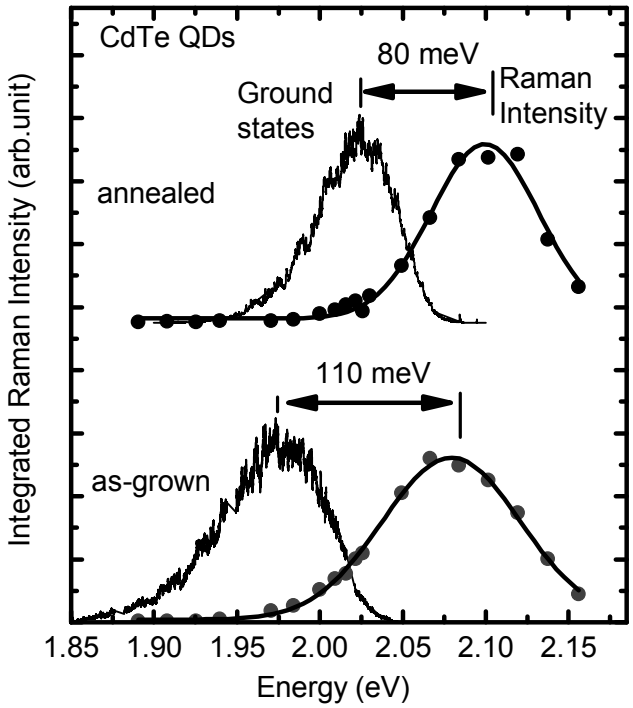

Figure 5.7: Room temperature ground and excited state distributions of CdTe QDs. Data points are the integrated RRS intensity of the 1-LO peak for the annealed (top) and as-grown (bottom) QD samples as a function of laser energy. Spectra to left are low-temperature micro PL data which have been shifted to account for the temperature shift of the bandgap.

In Fig. 5.8, we show a schematic of the effects of diffusion on a QD. The diffusion of Zn into the QD increases the energy of the band gap of the QD, as well as increases the QD size. Consequently, the QDs confining potential, which is both spatially wider and less deep, shifts the ground electronic states to higher energies and reduces the excitons GS-ES split. Our experimental observations shown in Fig. 5.7 reflect the effects of annealing as schematically presented in Fig. 5.8.

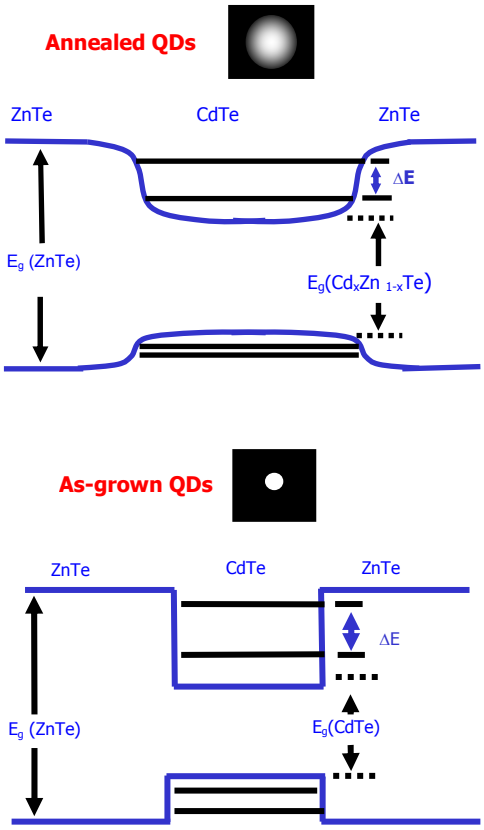

Figure 5.8: Schematic of effects of interdiffusion of Zn and Cd. It demonstrates how QD size, confining potential and the energy distribution changed due to annealing.

5.6 Raman Scattering from edge of the QD Sample

In order to probe the layers of a QDs sample, we study RRS from the *edge* of the sample. In this experimental geometry, we will observe Raman scattering from the transverse optical (TO) phonon which is not allowed in the backscattering geometry used previously. A 100X objective is used to focus the laser to about a 0.8 μm spot on

the sample and to collect the backscattered signal. The layers of the CdTe SAQDs samples are illustrated in the schematic drawing of Fig. 5.9. The thicknesses of the GaAs substrate and CdTe buffer layer are 1 mm and 4 μm respectively. The ZnTe buffer layer on which the QDs layer is deposited is 1 μm thick. Finally the 4 monolayer (ML) thick QDs layer is capped with a 50 nm thick ZnTe layer.

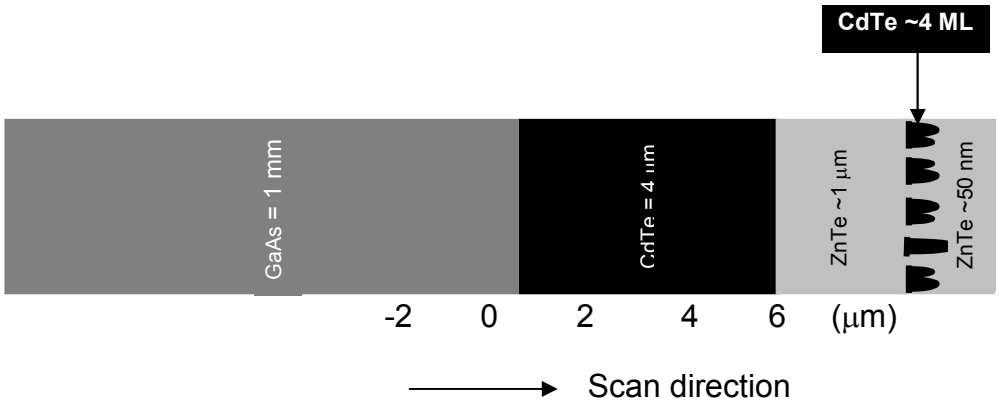

Figure 5.9: Schematic of the CdTe SAQDs sample as seen from the edge.

In Fig. 5.10, three representative room temperature RRS spectra taken from different positions on the edge of the CdTe QDs sample are shown. The Raman scattering peak observed at 267 cm^{-1} on the top spectrum in Fig. 5.10 is associated with a 1-TO GaAs phonon from the GaAs substrate. The Raman signal at 140 cm^{-1} is attributed to a 1-TO CdTe phonon. As noted earlier, the peak at 124 cm^{-1} that is associated with CdTe does not correspond to any known CdTe phonon energy. The signal observed at 202 cm^{-1} on the bottom spectrum in Fig. 5.10 is associated with a 1-LO ZnTe phonon. The 1-LO ZnTe phonon is possible since the collection angle of 100x

is large enough to collect Raman scattering from the surface of the sample, a (100) plane.

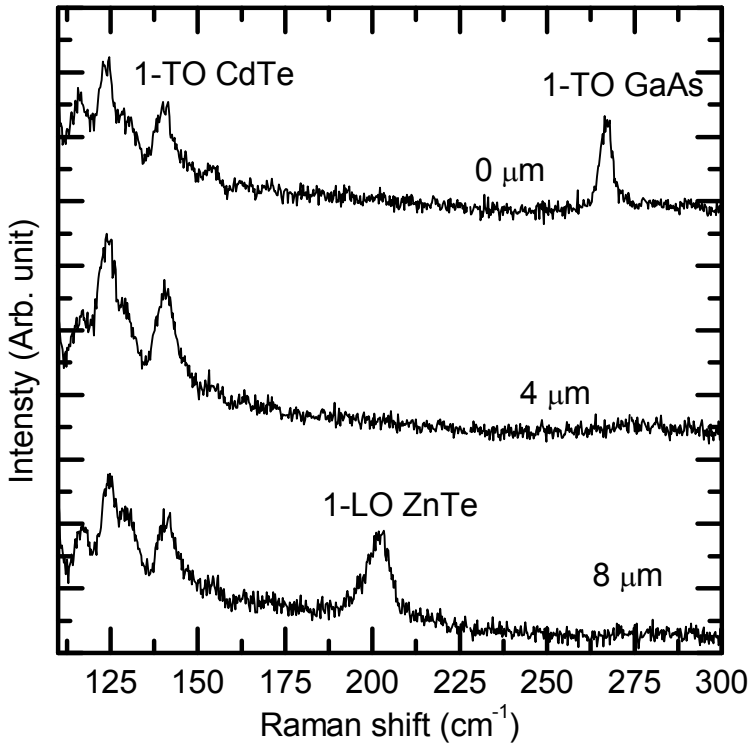

Figure 5.10: Representative Room temperature RRS taken from three different positions on the edge of CdTe QDs sample using the 496.5 nm excitation wavelength of Ar ion laser.

In Fig. 5.11, integrated intensities of 1-TO GaAs, 1-TO CdTe phonons and the signal at 124 cm^{-1} are plotted as a function of positions along the edge. The solid circle data points are integrated intensities of the 1-TO GaAs phonon. The open and solid square data points are the integrated intensities of CdTe phonons observed at 124 and 140 cm^{-1}, respectively. The triangular data points are integrated intensities of the 1-LO ZnTe phonon peak at 202 cm^{-1}. Note that as we approach the sample surface from the

substrate direction (from left to the right in Fig. 5.11), the intensity of the 1-LO GaAs phonon drops sharply as the intensity of the 1-TO CdTe phonon increases in a similar fashion. We believe that 1-TO phonon scattering from ZnTe could not be detected due to the small amount of ZnTe material and the low TO phonon scattering efficiency. The measured thickness of the CdTe buffer layer is about 4 μm, consistent with the thickness measured during deposition.

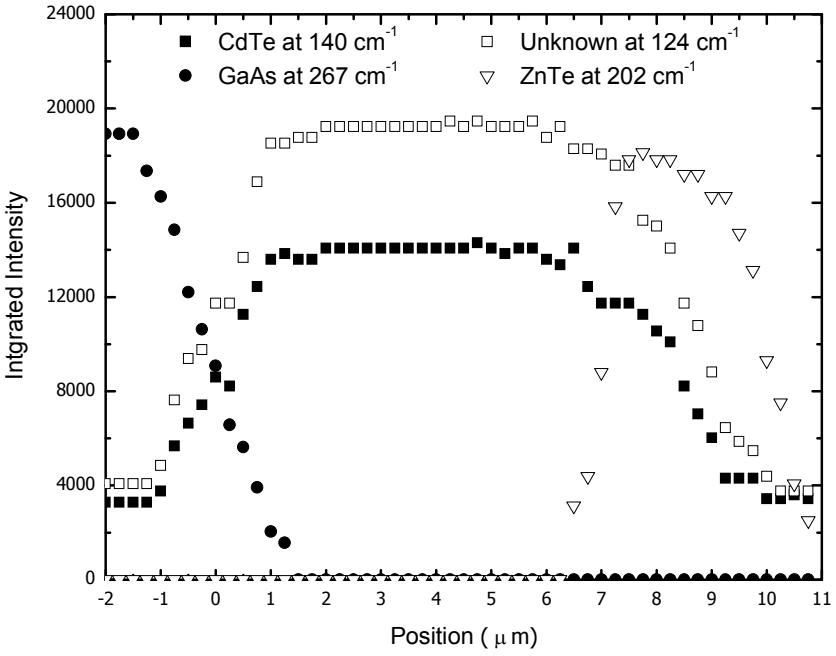

Figure 5.11: Room temperature integrated RRS of CdTe QDs sample. Solid circle data points are the integrated RRS of the 1-TO phonon from GaAs substrate. The Square data points are integrated intensities of the peaks observed at 124 and 140 cm^{-1} which are associated with CdTe. The triangular data points are integrated intensities of the ZnTe 1-LO phonon. The thickness of the CdTe buffer layer is estimated to be 4 μm.

To conclude, we have successfully demonstrated that RRS probes the excited states distribution of a single layer of CdTe self-assembled QDs at room temperature. We show that this technique effectively characterizes the changed energy profile of QDs which occurs after annealing. We find that the GS-ES splitting is clearly reduced as a result of annealing and is consistent with the formation of larger QDs through interdiffusion. Movement of the QD ensemble energies to higher energies is also consistent with the shallower confinement potential of the dots caused by interdiffusion. These results demonstrate the potential utility of resonance Raman scattering for characterization of QDs energy distributions. In addition, the spatially-resolved resonant Raman scattering from the edge of CdTe SAQDs sample was used to probe the layers of the sample effectively.

6 Resonant Raman scattering of CdS nanowires

We exploit the sensitivity of resonant Raman scattering (RRS) to probe the electronic and vibronic states of an ensemble of CdS nanowires and single CdS nanowires. In addition, we make use of Raman scattering at resonance to probe the structural uniformity in a single nanowire. RRS as a probe of the excited states of semiconductor nanostructures has been discussed in the previous chapter for CdTe quantum dots. In addition, the RRS was shown to be a sensitive way to study the effects of post-growth annealing on the energy distribution of the quantum dots. This provides the motivation to use this technique to study the electronic and vibronic structure in CdS nanowires.

First, we present typical room temperature PL and RRS spectra from an ensemble of CdS nanowires. Then, we show resonance behavior in the 1-LO phonon of an ensemble of CdS nanowires. Next, we provide the RRS integrated intensities as a function of excitation energy and compare it with a room temperature PL spectrum. We then report the typical resonant Raman scattering spectra and show integrated intensities as a function of excitation energies for a *single* CdS nanowire. We compare the integrated intensities with a PL spectrum for a single CdS nanowire. Finally, we illustrate the potential of spatially-resolved RRS as a tool to probe the structural uniformity in a single nanowire. The core of the work presented in this chapter has been recently published by Abdi et al. in Appl. Phys. Lett. **88**, 043118 (2006).[89]

6.1 Room Temperature PL from an Ensemble of CdS NWs

RRS and PL spectra were acquired from an ensemble of CdS nanowires (~10 nm diameter) at a number of excitation wavelengths from a cw Ar^+ laser source. Figure 6.1 displays a typical room temperature PL recorded from an ensemble of CdS nanowires sample using the 458 nm excitation wavelength. This spectrum displays a symmetric, broad (FWHM 80 meV) emission line centered at ~2.45 eV. Bulk epilayers and platelets show a room temperature emission band ~20 meV lower, at 2.43, with a somewhat narrower width (~60 meV).[90] This suggests that the electron and hole states may exhibit some modest quantum confinement in the ~10 nm nanowire,[28] consistent with the calculated exciton diameter for CdS of ~6 nm.[29] Because the NW emission linewidth is significantly larger than is typical for room temperature PL from bulk crystals, we conclude that PL from the nanowires is strongly inhomogeneously broadened, either through disorder in the wires themselves or by the varying diameters of the CdS nanowires within the ensemble.[91] Spectra acquired by collecting over ~1.25 μm diameter regions of the sample exhibited high intensity, suggesting that several nanowires are probably represented in a given spectrum.

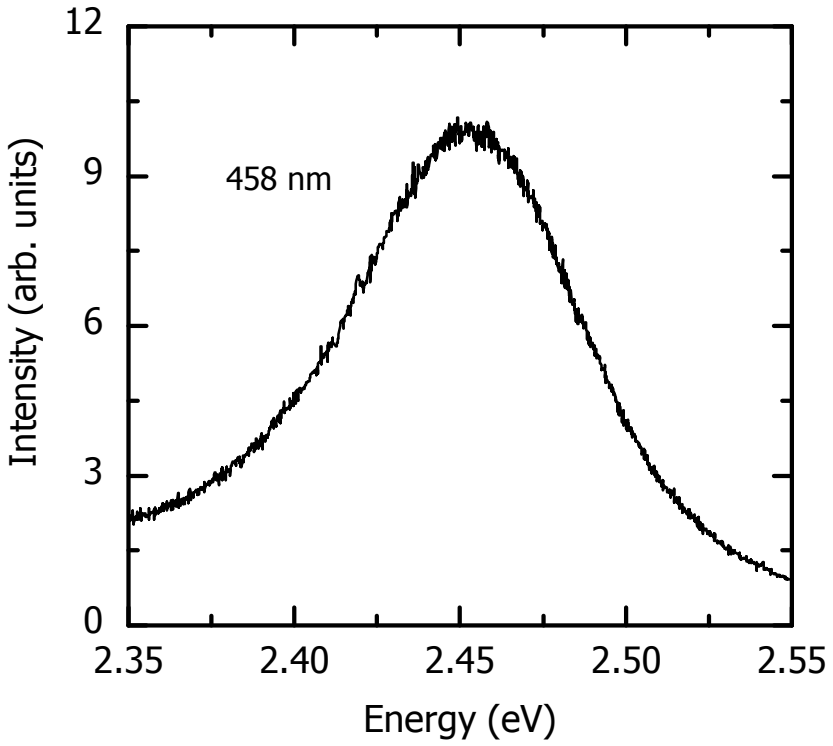

Figure 6.1: An off-resonance PL of an ensemble of CdS nanowires excited with the 458 nm laser line.

6.2 Optical Phonons in a CdS Nanowires

Figure 6.2 displays resonant Raman scattering spectra excited with the 488 and 496.5 nm lines of the Ar^+ laser source. In both spectra, strong 1-LO and 2-LO Raman resonances at ~ 301 and 603 cm^{-1} respectively from the ensemble of CdS nanowires were readily observed within the broader photoluminescence (PL) emission. This enables comparison of the electronic and phonon structure with that of the bulk material. As shown below, the optical phonon line from the substrate Si at ~ 520 cm^{-1} is also observed between the CdS nanowires' 1-L0 and 2-LO phonon lines.

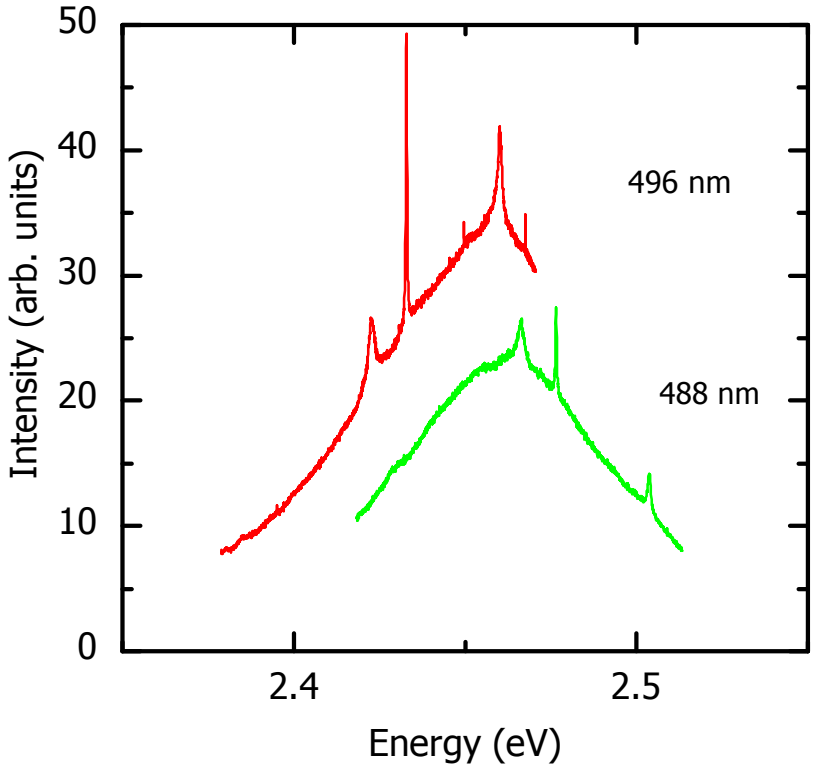

Figure 6.2: Typical room temperature resonant Raman spectra for two excitation wavelengths, 488 nm and 496.5 nm. Sharp LO phonon lines are evident on top of the PL spectrum.

The 488 and 496.5 nm laser excitations are near the peak of the PL, and one can easily see strong Raman peaks superimposed on top of the PL. The strong resonance for Raman scattering is demonstrated by the fact that the Raman scattered photons are an appreciable fraction (~ 10%) of the emitted PL at the same wavelength.

For excitation at 488 nm, the 2-LO phonon scattered peak is resonant with the peak of the PL spectrum, and is as strong as the 1-LO phonon peak. However, for the excitation at 496.5 nm, the 1-LO phonon peak which is resonant with the PL peak dominates the 2-LO phonon peak.

In order to study more closely these Raman peaks, the PL and dark signal background are subtracted. Figure 6.3 shows the results of this subtraction for the 488 nm data plotted in relative Raman shifts. In this spectrum, we observe three orders of peaks which can clearly be associated with the longitudinal optical phonon for CdS at 301, 603, and 906 cm^{-1}, respectively. These values are close to those observed in bulk CdS (300 cm^{-1} and 602 cm^{-1}) and CdS quantum dots (298 cm^{-1} and 600 cm^{-1}).[62] The sharp Raman line observed at 520 cm^{-1} is associated with the Si substrate and provides a means for calibration.

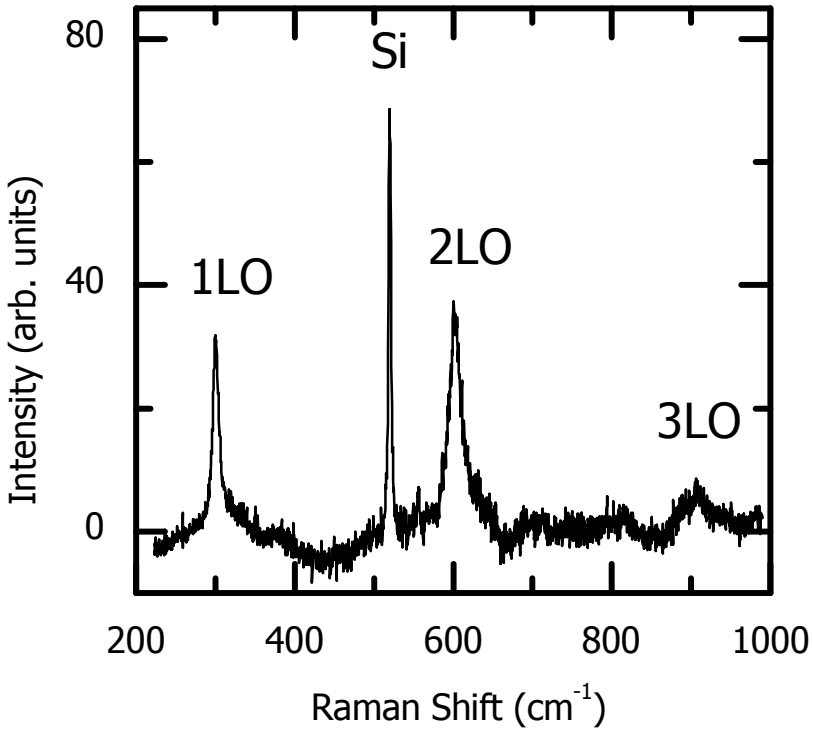

Figure 6.3: The Raman spectra excited at 488 nm laser line with background and PL subtracted.

To observe resonance behavior more clearly and to calculate the 1-LO and 2-LO

phonon integrated intensities, first the PL and dark signal background were subtracted for all measured spectra. Secondly, the resulting Raman intensities were normalized to the laser power and averaging time. Then, the 1-LO and 2-LO phonon response as a function of excitation energy were obtained. The 1-LO lineshapes are shown in Fig. 6.4. Finally, the integrated intensities as a function of excitation energy were obtained by integrating over the lineshapes.

6.3 RRS of CdS nanowires

The Raman resonance for the CdS nanowires is shown in Fig. 6.4 for the 1-LO Raman spectra (with the PL background subtracted) as a function of the six available Ar^+ laser lines. From this plot it becomes clear that the intensity of the1-LO Raman line is much stronger for laser excitation at 2.497 eV (496.5 nm) and less intense on either side. Similar plots for the 2-LO peak shows a resonance one phonon higher in energy at 2.531 eV. In each case, the frequency of the Raman scattered light is at the peak of the PL spectrum. From these considerations, we therefore conclude that the Raman process is most likely resonant with the outgoing photon rather than with the incoming photon.

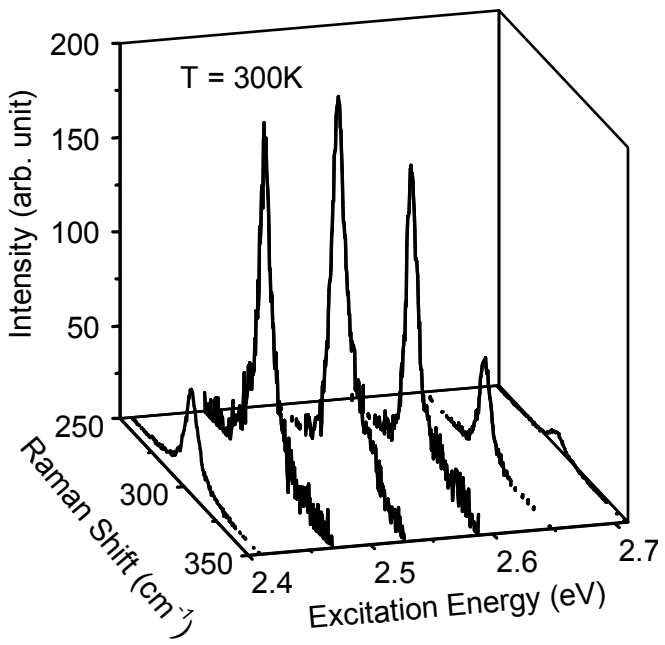

Figure 6.4: Raman spectra of 1-LO phonon peaks as a function of the excitation energy for CdS nanowires. The resonance of 1-LO reaches its maximum at an excitation energy of 2.497 eV.

6.4 Electronic states in CdS nanowires

To more easily quantify this resonance, in Fig. 6.5 we display the *integrated* RRS intensities of 1-LO and 2-LO peaks as a function of excitation energy along with the room temperature PL spectrum excited at 458 nm. The two dashed lines on the right are Gaussian fits to the 1-LO and 2-LO normalized integrated intensity of RRS as a function of excitation energy. In this figure, all curves are scaled to a common peak value. One can see directly that the 1-LO RRS intensity peaks at a laser energy of ~2.497 eV, and the 2-LO Raman lines peaks at ~2.531 eV. Both 1-LO and 2-LO

resonances are of similar width (80 meV), which is comparable to the width of the PL spectrum. The measured energy separation between 1-LO and 2-LO RRS peaks is ~34 meV, which is close to the expected longitudinal phonon energy of 37 meV (300 cm^{-1}).[92] However, the 42 meV energy difference between the peaks of the 1-LO integrated intensity and the PL spectrum is presently unclear.

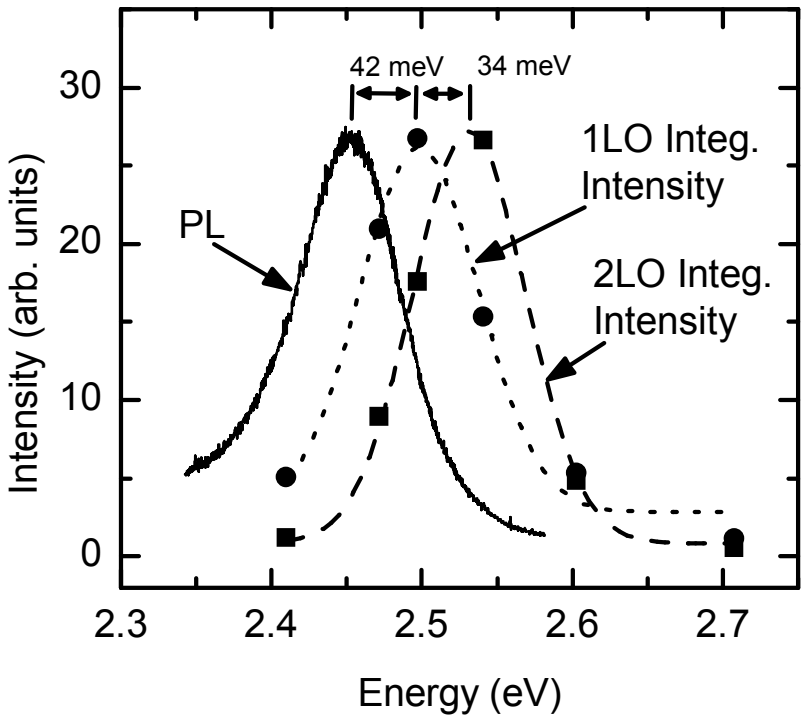

Figure 6.5: Room temperature PL excited at 458 nm (solid line), and room temperature integrated RRS intensities of 1-LO (circles) and 2-LO phonon scattering (squares) peaks as a function of excitation energy. The dashed lines are Gaussian fits to the integrated RRS LO phonon intensities. The energy difference between 1-LO phonon integrated intensity peak and PL peak is 42 meV, and the 1-LO to 2-LO resonant peak separation is 34 meV.

6.5 A single CdS nanowire

Typical RRS spectra from a *single* CdS nanowire excited by the 488 nm and 496.5 nm laser lines are displayed in Fig. 6.6. The peak at 520 cm^{-1} on both spectra is attributed to the Si substrate. In addition, we observe two peaks which can clearly be associated with the first and second longitudinal optical phonon for CdS at 301 and 603 cm^{-1} respectively. These 1-LO and 2-LO Raman peaks are strong enough that they are clearly visible on top of the broad photoluminescence emission of the NW. In order to quantify the resonance behavior and to calculate the integrated intensity of the 1-LO and 2-LO Raman peak, we have subtracted the PL background as done previously for the ensemble of CdS nanowires (see Figs. 6.3 and 6.4).

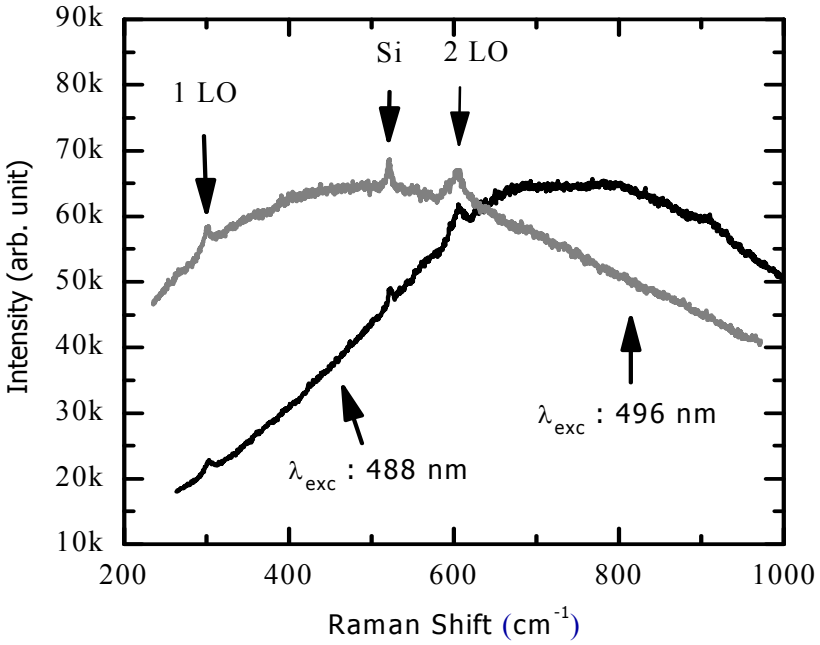

Figure 6.6: Typical resonant Raman spectra of a single CdS nanowire using 488 and 496.5 nm excitation.

In Fig. 6.7 we display the *integrated* RRS intensities of 1-LO and 2-LO peaks as a function of excitation energy along with the room temperature PL spectrum excited at 458 nm for a single CdS nanowire. The two dashed lines on the right are Gaussian fits to the 1-LO and 2-LO normalized integrated intensity of RRS as a function of excitation energy. In this figure, all curves are scaled to a common peak value as was done for the ensemble of CdS nanowires previously. One can see directly that the 1-LO RRS intensity peaks at a laser energy of ~2.471 eV, and the 2-LO Raman lines peaks at ~2.506 eV. Both the 1-LO and 2-LO resonances are of similar width (70 meV), which is comparable to the width of the PL spectrum, but somewhat smaller than that observed in an ensemble of CdS nanowires (80 meV). The two Raman peaks are separated by 35 meV, which is again in good agreement with the bulk LO phonon energy (37 meV) and slightly higher than observed in the case of ensemble of CdS NWs (34 meV). The measured energy difference between the 1-LO intensity and PL peak is 20 meV.

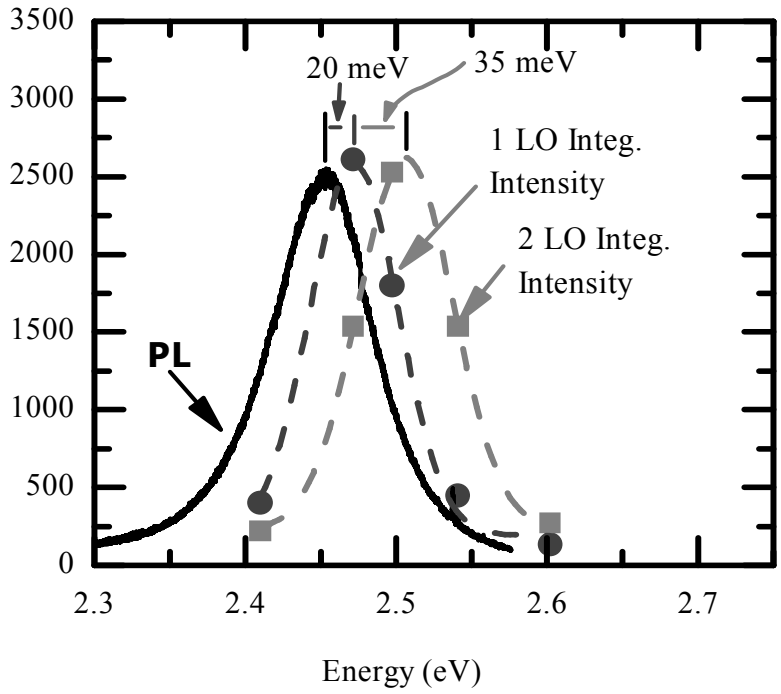

Figure 6.7: Room temperature PL, 1-LO and 2-LO phonons Integrated intensities of a single CdS nanowire as a function of excitation energy. The energy difference between 1-LO phonon integrated intensity peak and PL peak is 20 meV, and the 1-LO to 2-LO resonant peak separation is 35 meV.

6.6 Structural Uniformity in CdS nanowires

Spatially-resolved Raman scattering can be used to probe the structural uniformity of the nanowires since the positions of the Raman lines are extremely sensitive to strain and local composition.[93] Typical room temperature Raman spectrum from a single CdS nanowire taken in 1.0 μm steps along the growth axis is displayed in Fig. 6.8. In each spectrum, we observe Raman peaks which can be associated with the

1-LO and 2-LO phonons for CdS nanowire at 292 and 606 cm^{-1} respectively.

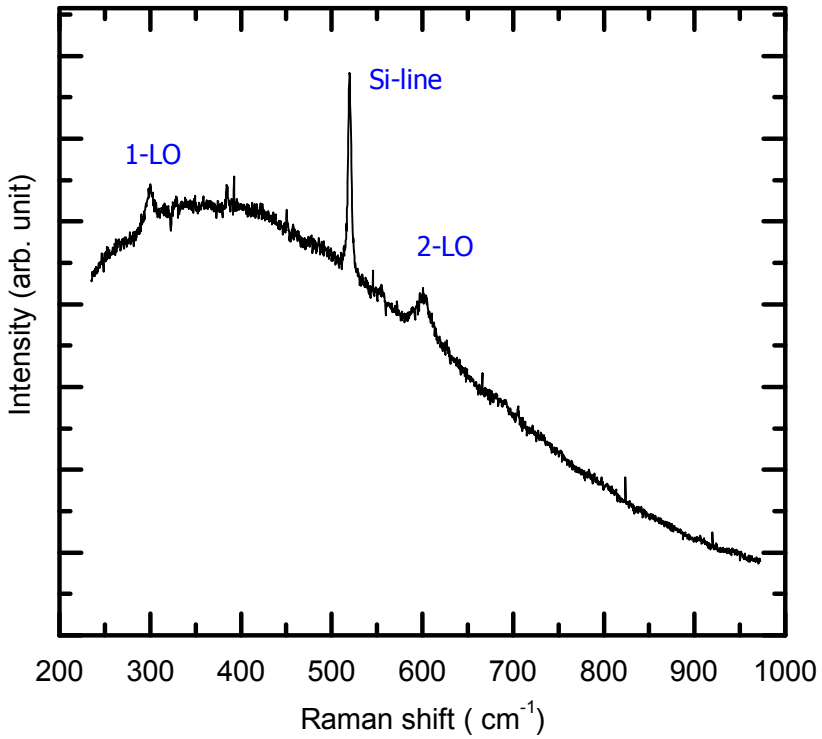

Figure 6.8: Typical room temperature Raman spectrum from a single CdS nanowire using 496.5 nm laser wavelength. The 1-LO and 2-LO phonons of CdS nanowire are observed at 292 cm^{-1} and 606 cm^{-1} respectively.

The peak intensity of the 1-LO and 2-LO phonons of CdS nanowire as a function of position along the wire is shown in Fig. 6.9. An optical image of the nanowire (taken with a 100X objective) shows morphological variations along ~7 μm length for this CdS nanowire, in particular a lobe near the nanowire center.

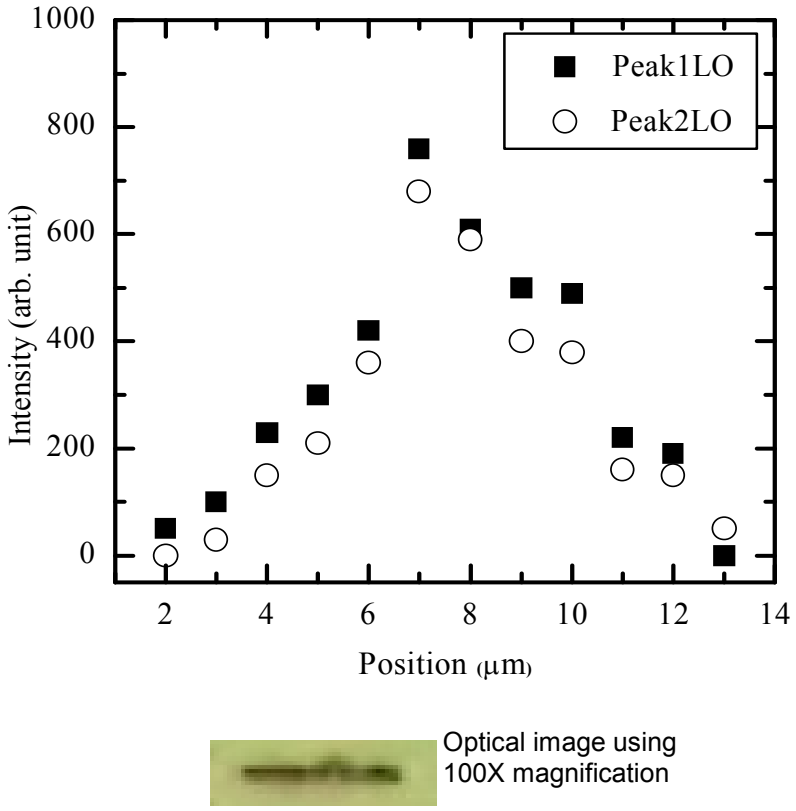

Figure 6.9: Integrated resonant Raman intensity for 1-LO and 2-LO as a function of position and an optical image of the wire.

The intensity of the 1-LO and 2-LO Raman lines also shows variations along the length of the wire. These variations of intensity of the 1-LO and 2-LO phonons are associated with the morphological variations. For reasons that are not presently clear, the intensity associated with the lobe on the nanowire is stronger than the intensity from other parts of the wire. The positions and widths of the 1-LO and 2-LO peaks are unchanged. These results show that spatially-resolved Raman scattering provides

insight into the structural uniformity of individual nanowires.

We have successfully demonstrated the use of resonant Raman scattering to probe the electronic and vibronic structure of an ensemble CdS nanowires and single CdS wires at room temperature. In the case of an ensemble of CdS nanowires, the sample inhomogeneity is reflected both in width of the PL spectrum and in the width of the resonant Raman integrated intensities as a function of excitation energy. The peaks of the resonant Raman scattering of 1-LO and 2-LO phonons are separated in energy by 34 meV which agrees well with bulk values. The 1-LO and 2-LO phonon resonances are unusually strong, as they are evident above the PL peak intensity. The ability to perform spatially-resolved Raman measurements of individual nanowires provides a unique opportunity for investigating the structural uniformity of the wires along the growth axis. We believe that these types of measurement could be further optimized through the use of a continuously tunable laser. A continuously tunable laser would provide the opportunity to determine the energy difference between the 1-LO and 2-LO phonons more precisely and also to probe the excited states.

7 Summary

In summary, we have shown that resonant Raman scattering at room temperature can be used to probe electronic and vibronic structures of two classes of II-IV semiconductor nanostructures, CdTe/ZnTe SAQDs and CdS nanowires. In addition, we have demonstrated that the spatially-resolved RRS from a single CdS nanowire and from the edge of a CdTe/ZnTe SAQDs sample can effectively probe the structural uniformity in the single nanowire and layers of the quantum dots sample, respectively.

The first and second order ZnTe LO-phonon scattering from CdTe/ZnTe SAQDs samples have been observed at Raman frequencies of 202 cm^{-1} and 404 cm^{-1}, respectively. Using the sensitivity of the ZnTe 1-LO phonon resonance, we have probed the excited states (ES) distribution in the CdTe/ZnTe quantum dots. The ZnTe 1-LO phonon is in resonance with the exited state of the quantum dots, since the QDs excited state penetrates into the surrounding ZnTe matrix. This can be explained by the fact that the size of the CdTe exciton Bohr radius (10 nm) is larger than the QDs (3 nm) and thus extends into the surrounding ZnTe. The peaks of the ZnTe resonance are observed at 2.08 and 2.10 eV for the as-grown and annealed CdTe/ZnTe SAQDs samples, respectively, and are much lower than the bandgap of the bulk ZnTe 2.26 eV and yet are higher than CdTe bulk bandgap of 1.43 eV. This suggests that integrated ZnTe RRS intensity reflects coupling to the excited states of the quantum dots than the ground states of ZnTe.

In order to find the energy splitting between the excited state and the ground state in the CdTe/ZnTe quantum dots, we have used a modified Varshni empirical equation to determine the ground states (GS) of the quantum dots at room temperature from temperature dependent PL measurements. From the energy splitting between the ES and GS of the as-grown and annealed samples, we have verified that the ES-GS is reduced due to post growth thermal annealing. In addition, we have shown that annealing caused a shift of the excited states towards higher values. These results are in agreement with previous observations that the annealing induces interdiffusion between the QDs and the barrier material leading to the enlargement of QDs with a shallower confining potential.

We have probed the layers in the quantum dot sample by spatially-resolved resonance Raman scans across the edge of the sample. The Raman signal scattered from the edge of the sample displays a CdTe TO phonon at 140 cm^{-1} that was not allowed from the (100) in the backscattering geometry. The thickness of the layers measured using this technique is in good agreement with value measured during growth. The resonant ZnTe 1-LO signal which is only observed as we approach the CdTe quantum dots layer confirms that the ZnTe 1-LO resonance probes the excited states in the quantum dots.

In the case of CdS nanowires, we have observed the first and second order CdS LO-phonon scattering at 301 and 603 cm^{-1} respectively. These phonon lines are readily observed above the broad PL of a single CdS nanowire at resonance. The sample inhomogeneity in the ensemble of CdS nanowires is reflected in the width of both the PL

and the integrated LO phonon intensities. The 1-LO and 2-LO CdS phonon resonance has been used to probe the electronic and vibronic states in both an ensemble of CdS nanowires and a single CdS nanowire. This is revealed in the similarity of the width of the PL and integrated RRS intensity. The energy separation between the peaks of 1-LO and 2-LO phonons resonant Raman scattering of 34 meV and 35 meV for the ensemble and single CdS nanowires agrees well with bulk values of 37 meV. In order to study the structural uniformity in a single CdS nanowire, we have collected RRS as a function of position on the wire. We have observed that the RRS intensities from a single nanowire strongly depends the morphology of the wire, whereas the energy position of the phonon lines remain unchanged. In particular, we have observed a strongly enhanced intensity associated with a lobe on the nanowire.

In conclusion, we have shown that RRS at room temperature is a sensitive tool to probe electronic and vibration sates as well as structural uniformity in semiconductor nanostructures.

References

[1] G. Karczewski, S. Mackowski, M. Kutrowski, T. Wojtowicz, and J. Kossut, Appl. Phys. Lett. **74**, 3011 (1999).

[2] Y. Arakawa and H. Sakaki: Appl. Phys. Lett., 40, 939 (1982).

[3] M. Asada, Y. Migamoto, Y. Suematsu, *IEEE J. QE*-**22**, 1915 (1986).

[4] M. Grundmann, J. Christen, N. N. Ledentsov, J. Böhrer, D. Bimberg, S. S. Ruvimov,‡, P. Werner, U. Richter, U. Gösele, J. Heydenreich, V. M. Ustinov, A. Yu. Egorov, A. E. Zhukov, P. S. Kop'ev, and Zh. I. Alferov, Phys. Rev. Lett. 74, 4043–4046 (1995).

[5] http://www.fujitsu.com/global/news/pr/archives/month/2004/20040910-01.html

[6] http://www.physlink.com/News/PrintNews.cfm?ID=73

[7] M.S. Skolnick and D.J. Mowbray, Annu. Rev. Mater. Res. 34, 181 (2004).

[8] P. Borri and W. Langbein, Topics in Appl. Phys. 90, 237 (2003).

[9] K. Gundogdu, K.C. Hall, E.J. Koerperick, C.E. Pryor, M.E. Flatte, T.F. Boggess, O.B. Shchekin and D.G. Deppe, Appl. Phys. Lett. 86, 113111 (2005).

[10] S. Mackowski, T.A. Nguyen, T. Gurung, K. Hewaparakrama, H. E. Jackson, L.M. Smith, J. Wrobel, K. Fronc, J. Kossut and G. Karczewski, Phys. Rev. B 70, 245612 (2004).

[11] M. Paillard, X. Marie, P. Renucci, T. Amand A. Jbeli and I.M. Gerard, Phys. Rev. Lett. 86, 1634 (2001).

[12] M. Law, J. Goldberger, and P. Yang, Annu. Rev. Mater. Res., 34, 83 (2004).

[13] X. Duan and C.M. Lieber, Adv. Mat. 12, 298 (2000).

[14] L. J. Lauhon, M. S. Gudiksen and C. M. Lieber, Phil. Trans. Roy. Soc. A 362.

[15] R. Agarwal, C. J. Barrelet and C. M. Lieber, Nano Lett. 5, 917 (2005).

[16] X. Duan, Y. Huang, Y. Cui, J. Wang and C. M. Lieber, Nature 409, 66 (2001).

[17] M. T. Borgstrom, V. Zwiller, E. Muller and A. Imamoglu, Nano Letters, 5, 1439 (2005).

[18] X. Duan, Y. Huang, R. Agarwal and C. M. Lieber, Nature, 421, 241 (2003).

[19] M. Bissiri, G. Baldassarri Höger von Högersthal, M. Capizzi, P. Frigeri and S. Franchi, Phys. Rev. B 64, 245337 (2001).

[20] T. A. Nguyen, S. Mackowski, H. E. Jackson, L. M. Smith, J. Wrobel, K. Fronc, J. Kossut, M. Dobrowolska, J. K. Furdyna, and W. Heiss, Phys. Rev. B **70**, 125306 (2004).

[21] K. H. Schmidt, G. Medeiros–Ribeiro, M. Oestreich, P. M. Petroff, and G. H. Döhler, Phys. Rev. B 54, 11346 (1996).

[22] S.W. Osborne, P. Blood, P.M. Smowton, Y.C. Xin and A. Stintz, Condens. Matter 16, 3749 (2004).

[23] C. Thomsen, S. Reich and J. Maultzsch, Philos. Trans. R. Soc. London, Ser. A**362**, 2337 (2004).

[24] D. Bimberg, M. Grundmann, N.N. Ledentsov, Quantum Dot Heterostructures, 1999 John Wiley & Sons Ltd, Chichester, England.

[25] F.T. Vasko and A.V. Kuznetsov, Electronic States and Optical Transitions in Semiconductor Heterostructures, Springer-Verlag New York , Inc., 1999.

[26] E.L. Ivchenko, Optical Spectroscopy of Semiconductor Nanostructures, 2005 Alpha Science International Ltd. Harrow, U.K.

[27] S. Mackowski, G. Karczewski, F. Kyrychenko, T. Wojtowicz, and J. Kossut, Thin Solid Film **367**, 210 (2000)

[28] U. Venkateswaran, M. Chandrasekhar and H.R. Chandrasekhar, Phys. Rev. B **30**, 3316 (1984).

[29] D. Kulik, H. Htoon, C. K. Shih and Y. Li, J. Appl. Phys. **95**, 1056 (2004).

[30] Landolt-Bornstein, New series, Group III, Vol. **17** a to i, **22** a b, **41** A to D, ed. By O. Madelung and. Rossler, *Springer, Berlin* (1982-2001).

[31] D.J. Stukel, R.N. Euwema, and T.C. Collins, *Phys. Rev. B*, **179**, 740 (1969)

[32] D.T.F. Marple and H. Ehrenreich, *Phys. Rev. B* **8**, 87 (1962)

[33] Ed Ghahramani, D.J. Moss and J.E. Sipe, Phys. Rev. B 43, 9700 (1991)

[34] V. Kumar, S. Kr. Sharma, T.P. Sharma and V. Singh, Optical Materials 12, 115 (1999)

[35] S. Ninomiya and S. Adachi, J. Appl. Phys. 78, 1183 (1995)

[36] B. Ullrich, R. Schroeder W. Graupner and H. Sakai, Optics Express 9, 116 (2001).

[37] D. Vogel, P. Kruger and J. Pollmann, *Phys. Rev. B* **54**, 5495 (1996)

[38] Y.P. Varshni, Physica 34, 149 (1967)

[39] M. Cardona, T.A. Meyer and M.L.W. Thewalt, Phys. Rev. Lett. 92, 196403 (2004)

[40] A. Monoogian and J.C. Woolley, Can. J. Phys. 62, 285 (1984)

[41] C.C. Kim, M. Daraselia and S. Sivananthan, Phys. Rev. B 56, 4786 (1997)

[42] D. Olguin, M. Cardona and A. Cantarer, Solid State Commun. **122**, 575 (2002)

[43] P.E. Lippens and M. Lannoo, Phys. Rev. B. **41**, 6079 (1990)

[44] L.-W Wang and A. Zunger, J. Phys. Chem. **98**, 2158 (1994)

[45] P. C. Sercel and K.J. Vahala, Phys. Rev. B **42**, 3690 (1990)

[46] D.C. Roger, et al. Phys. Rev. B **34**, 4002(1986)

[47] A. Debernardi, N. M. Pyka, A. Gobel, T. Ruf, R. Lauck, S. Kramp and M. Cardona, Sol. Stat. Comm. 103, 297 (1997)

[48] D.B. Tran Thoai, Y.Z. Hu and S.W. Koch, Phys. Rev. B 42, 11261 (1990)

[49] J. Li and L-W. Wang, Phys. Rev. B 72, 125325 (2005).

[50] M.A. Stroscio and M. Dutta, Phonons in Nanostructures, Cambridge University Press, 2001

[51] P. Y. Yu and M. Cardona, Fundamentals of Semiconductors, Spinger-Verlag Berlin Heidelberg, 1996

[52] A.V. Fedorov, A. V. Baranov, and K. Inoue, Phys. Rev. B 54, 8627 (1996)

[53] Y. Tado, O. Moriwaki, M. Nishioka and Y Arakawa, Physica E 8, 328 (2000)

[54] H. Rho, H. E. Jackson, S. Lee, M. Dobrowolska and J. K. Furdyna, Phys. Rev. B **61**, 15641 (2000)

[55] http://gltrs.grc.nasa.gov/reports/2002/TM-2002-211588.pdf

[56] G.I. Pangilinan, and Y.M. Gupta, Appl. Phys. Lett. **70**, 967 (1997)

[57] D. Drews, A. Schneider and D. R. T. Zahn, J. Vac. Tecjnol. B **15**, 1128 (1997)

[58] S. Kanakaraju, A.K. Sood and S. Mohan, J. of Appl. Phys. **84**, 5756 (1998)

[59] G. Bauer and W. Richter, Optical Characterization of Epitaxial Semiconductor Layers, Springer 1996

[60] J. Singh, Physics of Semiconductor and Their Hetrostructures, by McGraw- Hill, Inc. 1993

[61] L. K. Vodop'yanov, V.S. Vinogradov, N.N. Mel'nik, and G. Karczewski, JETP Letters, Vol. 77, No. 3, 143 (2003).

[62] A.Balandin K.L.Wang, N. Kouklin and S. Bandyopadhyay, “Raman spectroscopy of electrochemically self-assembled CdS quantum dots,” Appl. Phys. Lett, vol. 76, pp. 137-139 (2000).

[63] C. V. Raman and K. S. Krishnan, Nature, *121(3048)*, 501, March 31, 1928.

[64] C. V. Raman and K. S. Krishnan ,"A new radiation", Indian J. Phys., 2 (1928) 387

[65] http://www.kosi.com/raman/resources/tutorial/index.html

[66] J. R. Ferraro, K. Nakamoto and C.W. Brown, Introduction of Raman Spectroscopy, Academic Press, 2003.

[67] C.A. Arguello, D.L. Rousseau and S.P.S Porto, Phys. Rev. 181, 1351 (1969)

[68] C. Raptis, D. Nesheva, Y. C. Boulmatis, Z Levi and Z. Aneva, J. Phys.: Condens. Matter 16, 8221 (2004) Phys. Stat. Sol. 241, 572 (2004)

[69] R. Loudon, Proc. Royal Soc. London Ser. A 275, 219 (1963)

[70] M. Lamy de la Chapelle, H.X. Han and C.C. Tang, Eur. Phys. J. B 46, 507-513 (2005)

[71] A. Cantarero, C. Trallero-Giner, and M. Cardona, Phys. Rev. B 39, 8388 (1988)

[72] W.R. Tribe, D. Baxter, M.S. Skolnick, D.J. Mowbray, T.A. Fisher, and J.S. Roberts, Phys. Rev. B 56, 12429 (1997).

[73] A.K. Ganguly and J.L. Birman, Phys. Rev. 162, 806 (1967)

[74] M. P. Chamberlain, C. Trallero-Giner, and M. Cardona, Phys. Rev. B 51, 1680 (1994)

[75] H. J. Kim and Y.H. Xie, Appl. Phys. Lett. 79, 263 (2001)

[76] S. Lee, I. Daruka, C.S. Kim, A.-L. Barabasi, J.L. Merz, and J.K. Furdyna, Phys. Rev. Lett. 81, 3479 (1998)

[77] http://www.seas.ucla.edu/smrl/research/qd.htm

[78] J.L. Merz, S. Lee,and J.K. Furdyna, Journal of Crystal Growth, 184/185 (1998) pg 228-236

[79] Y. Terai, S. Kuroda K. Takita, T Okuno and Y.i Masumoto, Appl. Phys. Lett. 73, 3757 (1998).

[80] J. Hu, T.W. Odom and C.M. Lieber, Acc. Chem. Res. 32, 435-445 (1999)

[81] Y. Xia, P. Yang, Y. Sun, Y. Wu, B. Mayers, B. Gates, Y. Yin, F. Kim and H. Yan, Adv. Mater 15, 353 (2003).

[82] J.-P. Ge, J. Wang, H.-X. Zhang and Y.-D. Li, Chem. Eur. J. 10, 3525-3530 (2004).

[83] Y. Wu and P. Yang, J. Am. Chem. Soc. 123, 3165 (2001)

[84] a triple Raman Spectrometer User manual, by Jobin Yvon, 1996

[85] A. Abdi, T. B. Hoang, S. Mackowski, L.M. Smith, H.E. Jackson, J.M.Yarrison-Rice, J. Kossat and G. Karczewski, Appl. Phys. Lett. 87, 183104 (2005).

[86] P.T.C. Freir, M.A. Araujo Silva, V.C.S. Reynoso, A.R. Vaz, and V. Lemos, Phys. Rev. B **55**, 6743 (1996).

[87] A.M. de Paula, L.C. Barbosa, C.H.B. Cruz, O.L. Alves, J.A. Sanjurjo and C.L. Cesar, Appl. Phys. Lett. **69,** 6951 (1996).

[88] S. Mackowski, L. M. Smith, H. E. Jackson, W. Heiss, J. Kossut and G. Karczewski, Appl. Phys. Lett. **83,** 254 (2003).

[89] A. Abdi, L.V. Titova, L.M. Smith, H.E. Jackson, J.M.Yarrison-Rice, J.L. Lensch and L.J. Lauhon, Appl. Phys. Lett. 88, 043118 (2006).

[90] C. J. Barrelet, Y. Wu, D. C. Bell and C. M. Lieber, J. Am. Chem, Soc. **125**, 11498 (2003).

[91] Y. Knemitsu, T. J. Inagaki, M. Ando, K. Matsuda, T. Saiki and C. W. White, Appl. Phys. Lett. **81**, 141 (2002).

[92] M. H. Huang, S. Mao, H. Feick, H. Q. Yan, Y. Y. Wu, H. Kind, E. Weber, R. Russo, P. D. Yang, Science **292**, 1897 (2001).

[93] See, for instance, H. Rho, Howard E. Jackson and B. L. Weiss, "Mapping of local stress distributions in SiGeOSi otical chennel waveguide," J. Appl. Phys. , vol. 90, pp. 276-282 (2000).

Appendices

A. Dye Laser Optical Alignment

Here, we will present full optical alignment procedures assuming the jet stream is properly aligned. The procedures are as follows.

Switch off the pump laser and then the dye circulator.

Remove and clean Output coupler M3 (Fig. A.1, item 6), birefringent filter (Fig. A.1, item 5), pump mirror P1 (Fig. A.1, item 3), end mirror M1 (Fig. A.1, item 4) and fold mirror M2 (Fig. A.1, item 2) according to the removal and cleaning procedures written in the manual. Lay them at safe place on layers of new optical tissues on clean table with the optics facing up. Cover the optics form dust with a new optical tissue.

Turn on the pump laser and make sure the power is less than 150 mW. This is to protect the fold mirror from damage in case the direct pump laser strikes it with dye jet stream off.

Align the pump laser by adjusting the three dye laser height adjusting screws, item 12 shown in Fig. A.1, so that the pump laser pass through the center of the pump beam input aperture, item 11, and enters the pump beam leveling aperture, item 10, at the center. Securely bolt the dye laser to the optical table and double check the pump laser alignment. **Note:** The position of the items on the dye laser is indicated by numbered arrows in Fig. A.1.

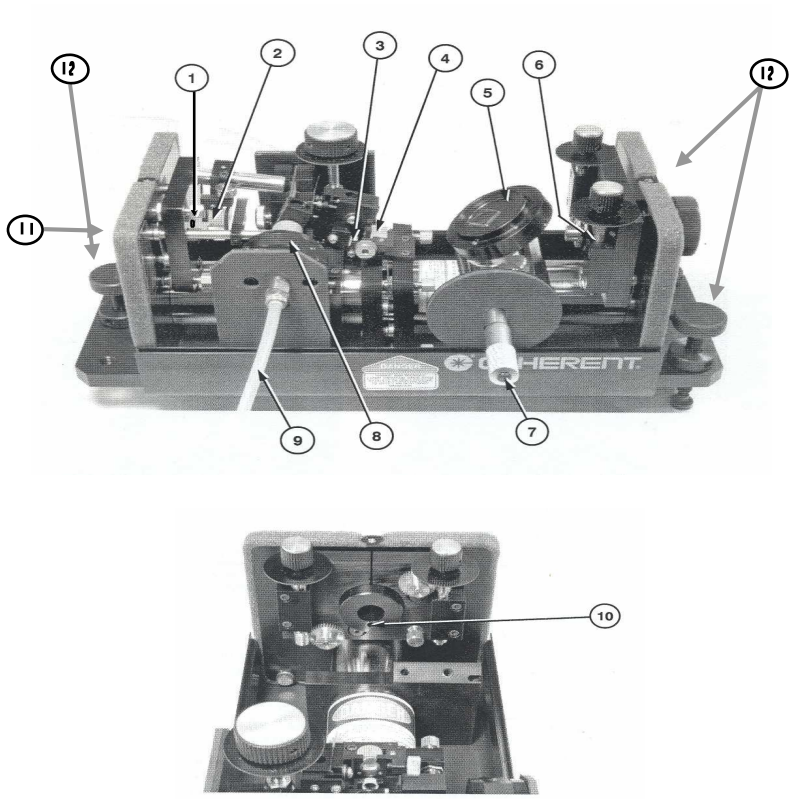

Pump mirror alignment hole 11	BRF micrometer
Fold mirror M2	Dye jet translation assembly
Pump mirror P1	Dye input hose
End mirror M1	Pump beam leveling aperture
Birefringent filter (BRF)	Pump beam input Aperture
Output coupler M3	pump beam leveling adjustment

Figure A.1: Major Laser Head Components.

Block the pump laser and install pump mirror P1 with the caret (>) on the edge of the optics pointing toward the dye jet stream. Make certain that the pump mirror coating stripe is vertical as shown on Fig. A.2.

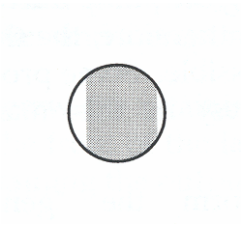

Figure A.2: Pump mirror coating stripe.

Fine-tune the pump mirror vertical and horizontal fine adjust controls (items 4 and 8 on Fig. A.3) at the middle of their travel.

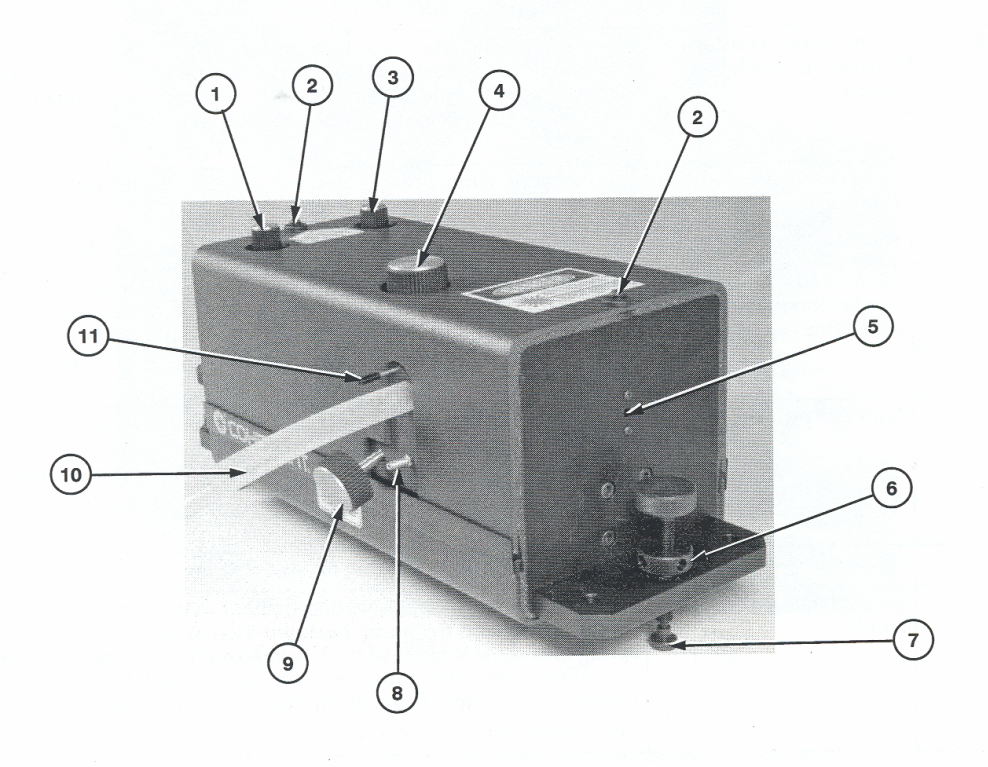

Figure A.3: Laser head controls- cover on.

Unblock the pump laser; use the manual coarse pump mirror adjustments (items 10 and 11 on Fig. A.4) to adjust the pump mirror so that the beam strikes in the upper one-third of the mirror. **Note:** Do not make use of the fine adjustments knobs at this point. Ensure the pump mirror coating stripe is vertical.

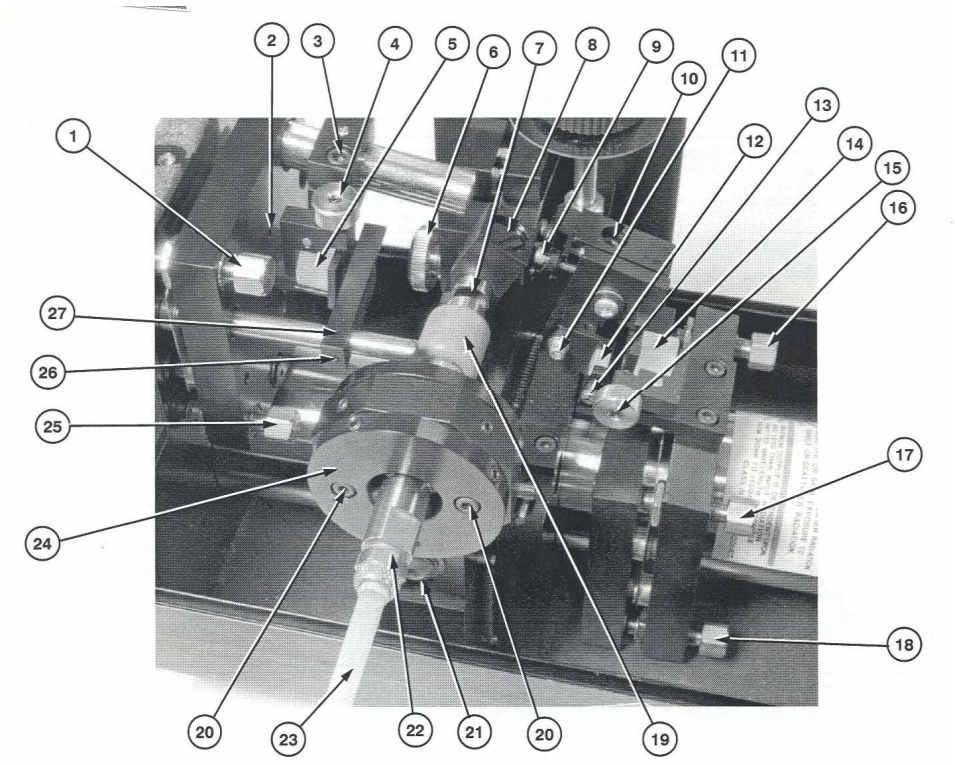

Figure A.4: Laser head controls

Have pump beam dump retaining screw loose and raise the pump beam dump.

Check if reflected pump beam goes into the pump mirror alignment aperture (Fig. A.4, item 2) in addition make sure that the pump beam strikes the top one-third of the pump mirror. If not readjust the pump mirror such that the reflected beam goes through the pump alignment aperture and the beam hit the top one-third of the pump mirror. **Note**: Do not disturb the focus of the pump mirror since the screw is not in good condition unless it is absolutely necessary.

Check that the pump laser power is less than 150 mW. Install the fold mirror M2 with the caret (>) on the edge of the optics pointing toward the dye jet stream.

Put the dye circulation switch to the PUMP position and confirm that the pressure on the pressure indicator is 40 psi. If not adjust the pressure.

Cover up the catch tube pump beam cutout (item 7 on Fig. A.4) with neutral density filter (item 8 on Fig. A.4) to protect your eye.

Change the dye circulation switch to the JET position to start dye flow. View the pump beam through neutral density filter on the dye jet; it should at the center of the jet. If not, adjust the jet position in accordance to the manual.

Block the beam hitting the fold mirror with the pump beam dump and increase the pump beam power to 5 W to measure the dye absorption.

Extra care should be taken during measuring the dye absorption since it involves directing the pump beam out of the dye laser cavity. Wear safety Glasses! Put a mirror in front of M2 to direct the beam out of the laser cavity and measure power of the reflected beam with the jet on and with the jet off. **Note**: do not allow the pump beam to strike fold mirror M2.

$$Absorption = \left[\frac{Power\ without\ the\ jet - power\ with\ the\ jet}{Power\ without\ the\ jet} \right] \times 100\%$$

Adjust the dye solution until the absorption is 80%. Too high absorption will red shift the tuning curve and also causes thermal lensing of the jet and instability. Lower absorption will yield lower power output with very little blue shift.

Block the pump beam out side the dye laser, move pump beam dump out of your way (raise) and turn on the jet. **Note**: the catch tube pump beam cutout should be covered with the neutral density filter.

By loosing the M2 mount assembly (item 3 on Fig. A.4), move the M2 to the center of its travel and secure it there.

Using a white card, find the fluorescence spot within the dye laser. Once you find the spot, you can adjust the M2 horizontal/vertical angle adjust, and pivot adjust (items 25 and 1 on Fig. A.4) so that the fluorescence spot can be seen outside the laser head on a white card at least 130 cm away.

Move the fold mirror back and forth until the spot is sharp and tighten it securely.

Put a lens tissue on the output coupler mount hole (Fig. A.1, item 6) and adjust M2 using vertical and horizontal tilt angle adjusts so that the spot is at the center of the hole.

Lower the pump beam dump to block unabsorbed pump beam.

Tune the pump mirror focus (use item 9 Fig. A.4) until the fluorescence spot is circular and back up ¼ - ½ turn.

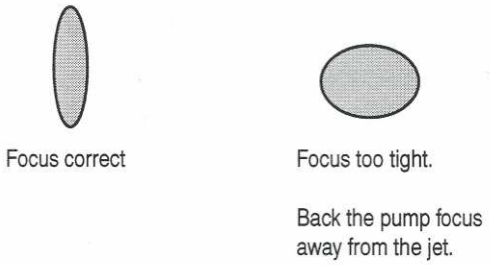

Figure A.5: Correct focus of the fluorescence spot from fold mirror.

Install end mirror M1 and bring the fluorescence spot from M1 next to the spot from M2 using the M1 horizontal and vertical angle adjusts (Fig. A.4, items 16 and 18) and M1 pivot adjust (item 17). Keep on tuning the M1 adjusts until the size of the M1 spot is the same as the M2 spot.

Slowly move the white card closer to the laser while observing the spots. The spots should remain nearly the same. If the spots are the same proceed to step 25. If not repeat the M1 adjustment.

Overlap the two spots using the M1 adjustments.

Install the output coupler with the caret (>) on the edge of the optics pointing toward the dye jet stream.

By pushing the M3 vertical tilt angle adjust (Fig. A.1, item 13) in front and back motion, locate the reflection of the fluorescence spot from the M3.

Adjust the M3 horizontal and vertical tilt angle adjusts and the pivot adjust until the spot is back reflected (until lasing occurs).

If lasing doe not occur after repeating steps 27 and 28 for a few minutes, repeat steps 17-28.

Once it start lasing, peak it using fine adjustment knobs of the P1 (items 4 and 9 Fig. A.3) and fine adjustment knobs of the M3 (items 1 and 3 on Fig. A.3).

B. Front Panel of the LabView Program

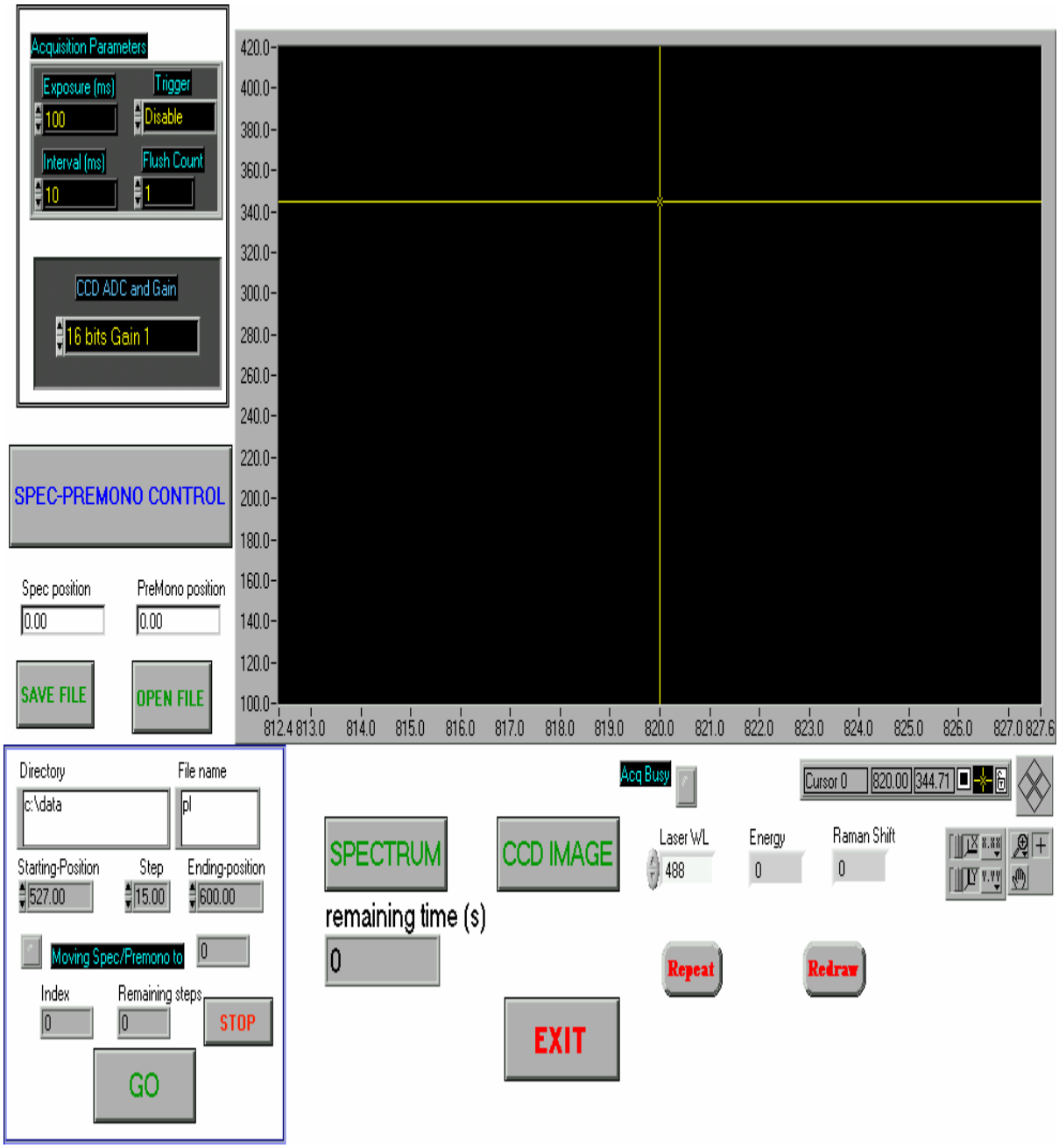

Figure B.1: Front panel of the LabView program that allows taking continuous spectrum.

To take continuous spectrum, we have to fill the information in the box ar the bottom left hand side and hit GO. The program saves individual spectrum in using the file name typed under the directory you specified. You can also save the whole spectrum at the end when the program tells you that it is done. While running, the program shows the total number of steps, the currently running step and the remaining time. You can hit STOP in case you need to interrupt taking data. But do not forget to hit the STOP button after you get the massage done.